

AWARD NUMBER: W81XWH-16-1-0434

TITLE: Optimizing Ventilation Distribution and Gas Exchange in Combat-Related Lung Injury Using Multifrequency Oscillation

PRINCIPAL INVESTIGATOR: David W. Kaczka, MD, PhD

CONTRACTING ORGANIZATION: University of Iowa
Iowa City, IA 52242-1316

REPORT DATE: October 2017

TYPE OF REPORT: Annual

PREPARED FOR: U.S. Army Medical Research and Materiel Command
Fort Detrick, Maryland 21702-5012

DISTRIBUTION STATEMENT: Approved for Public Release;
Distribution Unlimited

The views, opinions and/or findings contained in this report are those of the author(s) and should not be construed as an official Department of the Army position, policy or decision unless so designated by other documentation.

REPORT DOCUMENTATION PAGE

*Form Approved
OMB No. 0704-0188*

Public reporting burden for this collection of information is estimated to average 1 hour per response, including the time for reviewing instructions, searching existing data sources, gathering and maintaining the data needed, and completing and reviewing this collection of information. Send comments regarding this burden estimate or any other aspect of this collection of information, including suggestions for reducing this burden to Department of Defense, Washington Headquarters Services, Directorate for Information Operations and Reports (0704-0188), 1215 Jefferson Davis Highway, Suite 1204, Arlington, VA 22202-4302. Respondents should be aware that notwithstanding any other provision of law, no person shall be subject to any penalty for failing to comply with a collection of information if it does not display a currently valid OMB control number. **PLEASE DO NOT RETURN YOUR FORM TO THE ABOVE ADDRESS.**

1. REPORT DATE October 2017			2. REPORT TYPE Annual		3. DATES COVERED 15 Sep 2016 - 14 Sep 2017			
4. TITLE AND SUBTITLE Optimizing Ventilation Distribution and Gas Exchange in Combat-Related Lung Injury Using Multifrequency Oscillation					5a. CONTRACT NUMBER W81XWH-16-1-0434			
					5b. GRANT NUMBER W81XWH-16-1-0434			
					5c. PROGRAM ELEMENT NUMBER			
6. AUTHOR(S) David W. Kaczka, M.D., Ph.D. E-Mail:david-kaczka@uiowa.edu					5d. PROJECT NUMBER			
					5e. TASK NUMBER			
					5f. WORK UNIT NUMBER			
7. PERFORMING ORGANIZATION NAME(S) AND ADDRESS(ES) University of Iowa, The 105 Jessup Hall Iowa City IA 52242-1316					8. PERFORMING ORGANIZATION REPORT NUMBER			
9. SPONSORING / MONITORING AGENCY NAME(S) AND ADDRESS(ES) U.S. Army Medical Research and Materiel Command Fort Detrick, Maryland 21702-5012					10. SPONSOR/MONITOR'S ACRONYM(S)			
					11. SPONSOR/MONITOR'S REPORT NUMBER(S)			
12. DISTRIBUTION / AVAILABILITY STATEMENT Approved for Public Release; Distribution Unlimited								
13. SUPPLEMENTARY NOTES								
14. ABSTRACT The goal of this research project was to develop a novel method for mechanical ventilation, termed ‘Multi-Frequency Oscillatory Ventilation’ (MFOV), which optimizes gas exchange in the acute respiratory distress syndrome (ARDS) and other forms of combat-related lung injury, while simultaneously preserving mechanical protection of the lung. We hypothesized that lung function and gas exchange would be significantly improved if small volume oscillations are applied at multiple frequencies simultaneously, rather than at a single frequency, due to more even distribution of ventilation to different lung regions in accordance with local mechanical properties. In Specific Aim 1, we designed candidate MFOV waveforms for the acutely injured lung, using structurally explicit computational models of the mammalian respiratory system. Our simulations demonstrated that MFOV waveforms are capable of minimizing parenchymal strain and strain rate in healthy and injured lungs. In Specific Aim 2, we used dynamic Xenon-enhanced CT imaging and registration to establish that MFOV improves ventilation distribution and gas exchange in a porcine model of ARDS, compared to conventional modes of ventilation. The results obtained from these studies demonstrate that MFOV has a high likelihood of yielding a new, viable mode of ventilation for use in both military and civilian populations with ARDS.								
15. SUBJECT TERMS Acute lung injury, Acute respiratory distress syndrome, Blast lung injury, Combat-related lung injury, Multi-frequency oscillatory ventilation, Oleic acid lung injury, computed tomography								
16. SECURITY CLASSIFICATION OF:			17. LIMITATION OF ABSTRACT Unclassified	18. NUMBER OF PAGES 100	19a. NAME OF RESPONSIBLE PERSON USAMRMC			
a. REPORT Unclassified					b. ABSTRACT Unclassified		c. THIS PAGE Unclassified	

TABLE OF CONTENTS

1.0	INRODUCTION	4
2.0	KEYWORDS	4
3.0	ACCOMPLISHMENTS	4
3.1	Goals of Project	4
3.2	Goal Accomplishments	5
3.2.1	Specific Aim 1	5
3.2.2	Specific Aim 2	8
3.3	Opportunities for Training and Professional Development	11
3.4	How were the results disseminated to the communities of interest?	11
3.5	What do you plan to do during the next reporting period to accomplish the goals?	11
4.0	IMPACT	11
4.1	What was the impact on the development of the principal discipline of the project?	11
4.2	What was the impact on other disciplines?	12
4.3	What was the impact on technology transfer?	12
4.4	What was the impact on society beyond science and technology?	12
5.0	CHANGES / PROBLEMS	13
5.1	Changes in approach and reasons for change	13
5.2	Actual or anticipated problems or delays and actions or plans to resolve them	13
5.3	Changes that had a significant impact on expenditures	13
5.4	Significant changes in the use or care of human subjects, vertebrate animals, biohazards, and/or select agents	13
6.0	PRODUCTS	13
6.1	Journal Publications	13
6.2	Books or other non-periodical, one-time publications	14
6.3	Other Publications, Conference Papers, and Presentations	14
6.4	Website or other Internet site	15
6.5	Technologies or techniques	15
6.6	Inventions, patent applications and/or licenses	15
7.0	PARTICIPANTS & OTHER COLLABORATING ORGANIZATIONS	15
7.1	What individuals have worked on the project?	15
7.2	Has there been a change in the active other support of the PI or key personnel since the last reporting period?	16
7.3	What other organizations were involved as partners?	17
8.0	SPECIAL REPORTING REQUIREMENTS	17
9.0	REFERENCES	18
10.0	APPENDICES	19

1.0 INTRODUCTION

Respiratory failure from **acute lung injury**, now termed the *acute respiratory distress syndrome* (ARDS), accounts for 4 million ICU days annually in the U.S., and is associated with high mortality (up to 40%) in both military and civilian populations. Survivors may also have substantial morbidity, with long-term physical and mental health impairments. ARDS thus places significant burdens on military and public health resources. Since ventilation distribution in ARDS is governed by a heterogeneous distribution of regional mechanics, the most appropriate distending pressure, ventilation frequency, or tidal volume for one lung region may not necessarily be the same for another, even in the same patient. This may result in large portions of an injured lung being simultaneously under-ventilated or over-ventilated, with poor ventilation-to-perfusion matching and increased dead space. **The goal of this research project is to develop a novel method for mechanical ventilation, ‘Multi-Frequency Oscillatory Ventilation’ (MFOV) that optimizes gas exchange in ARDS, while preserving lung protective ventilation.** We hypothesize that lung function and gas exchange will be significantly improved if small volume oscillations are applied at multiple frequencies simultaneously, rather than at a single frequency, due to more even distribution of ventilation to different lung regions in accordance with local mechanical properties. The purpose of this research project is to design candidate MFOV waveforms for the acutely injured lung, using structurally explicit computational models of the mammalian respiratory system. We then use dynamic computed tomographic (CT) imaging to determine whether MFOV improves ventilation distribution and gas exchange in a porcine model of ARDS. Regional ventilation is quantified using Xenon-enhanced CT in these pigs, while regional mechanical properties are assessed using image registration and measures of lung impedance. We expect our results to be ultimately translatable and testable in human clinical trials, with potential to reduce morbidity and mortality associated with ARDS and other heterogeneous lung diseases.

2.0 KEYWORDS

Acute lung injury	Porcine
Acute respiratory distress syndrome	Mechanical ventilation
Blast lung injury	Computed tomography
Combat-related lung injury	Xenon
High frequency oscillatory ventilation	Image registration
Multi-frequency oscillatory ventilation	Ventilator-induced lung injury
Oleic acid lung injury	

3.0 ACCOMPLISHMENTS

3.1 Goals of Project

The **overall goal** of this research project is to develop a novel method for mechanical ventilation, “Multi-Frequency Oscillatory Ventilation” (MFOV) that optimizes gas exchange in ARDS and other forms of combat-related lung injury, while preserving lung protective ventilation. Our hypothesis is that lung function and gas exchange will be significantly improved if small volume oscillations are applied at multiple frequencies simultaneously, rather than at a single frequency, due to more even distribution of ventilation to different lung regions in accordance with local mechanical properties. The **goals of our Specific Aims** are: 1) to design candidate MFOV

waveforms for the acutely injured lung, using structurally explicit computational models of the mammalian respiratory system; and 2) to use dynamic CT imaging to establish that regional heterogeneity is the mechanism by which MFOV improves ventilation distribution and gas exchange in a porcine model of ARDS.

3.2 Goal Accomplishments

During the first year of this award we have made substantial progress along our research plan, both in the development of computational models for the design MFOV waveforms in acutely lung injury, as well as the confirmatory animal experiments to assess regional ventilation distribution and strain during MFOV. Our progress is detailed for both Specific Aims 1 and 2 below.

3.2.1 Specific Aim 1

With regard to the computational modeling of Specific Aim 1, we completed the development of a three-dimensional computational model of a canine lung to simulate distributed gas flow and CO₂ elimination during oscillatory ventilation. Consistent with our hypothesis, our simulations from this model demonstrated that ventilation distribution in a heterogeneous lung is spatially clustered and dependent on oscillatory frequency (Figure 1). Such regional differences in gas exchange, as a function of frequency, further confirms our notion that use of MFOV is ideally suited for the heterogeneously injured lung. These results were recently published in the *Journal of Applied Physiology* (11).

To determine whether such model could be used to design candidate MFOV waveforms for the acutely injured lung, we developed a Monte Carlo optimization algorithm for tuning the spectral content of broadband oscillatory flow waveforms according to regional mechanical properties, in order to minimize parenchymal strain heterogeneity (Figure 2). Optimal combinations of frequencies, amplitudes, and phases in our MFOV waveforms were determined according to frequency-dependent distributions of ventilation throughout the heterogeneous periphery of our model. We found that the superposition of multiple simultaneous frequencies provided more uniform ventilation distribution in our model compared to single frequency oscillatory ventilation, with less potential for ventilator-induced lung injury (VILI). These results were presented at the 2016 Annual Meeting of the Biomedical Engineering Society in Minneapolis, Minnesota (6).

For consistency with our animal experiments of Specific Aim 2 (below), we have now extended these computational modeling and optimization techniques to the unique anatomy of the porcine lung, to investigate the potential for minimizing distributed acinar strains and strain rates during

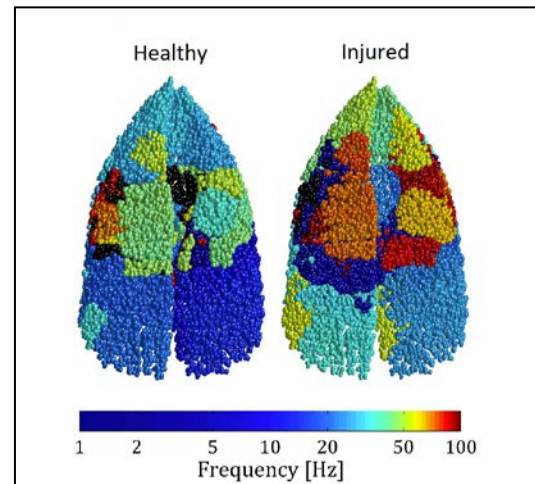
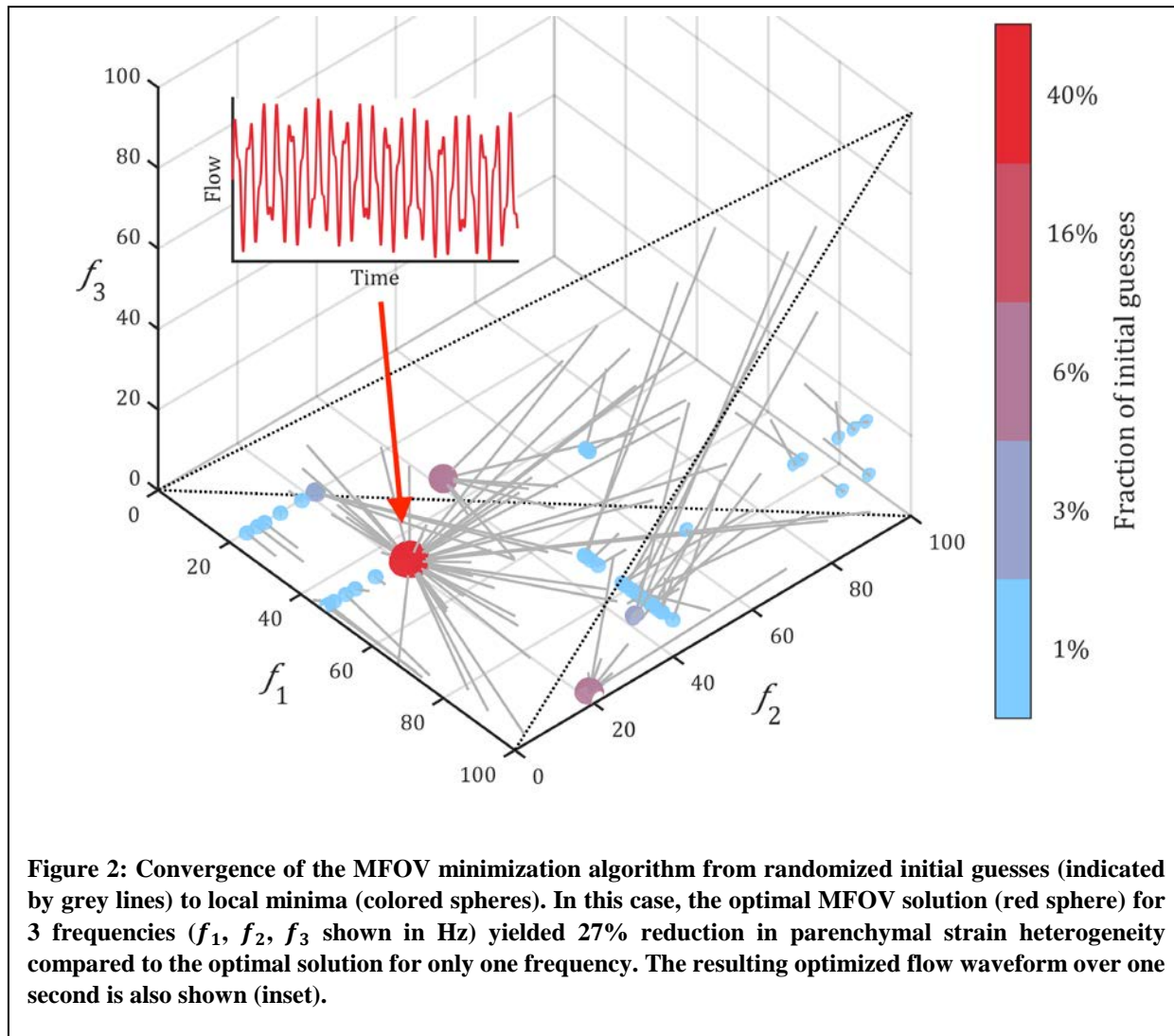


Figure 1: Optimal oscillation frequencies for CO₂ elimination in a healthy and injured canine lung model. The regional distribution of optimal frequencies in the models are clustered and heterogeneous. These are simulated assuming supine position of the animal, with the gravitational vector pointing out of the page, toward the reader. Modified from Herrmann et al. (11).



oscillatory ventilation (Figure 3). Again, our simulations demonstrated that MFOV waveforms are superior to traditional single-frequency HFOV for minimizing strain and strain rate in both healthy and injured pig lungs. More importantly, we found that an MFOV waveform consisting of uniform flow amplitudes across frequency (i.e., hyperbolically decreasing volume amplitudes with increasing frequency) achieved an appropriate balance between minimizing parenchymal strain vs. strain rate in the porcine lung. These results will be presented in poster format at the 2017 American Society of Anesthesiologists Meeting in Boston, Massachusetts (14).

Finally, we applied our computational techniques to simulate the effects of a very specific form of lung injury with military relevance: primary blast-lung injury. A computational model of a human airway network was generated using central airways obtained from segmented X-ray computed tomographic scans, and algorithmically generated peripheral airways (M.H. Tawhai *et al.*, *J Appl Physiol* 97(6):2310-2321, 2004). The model consisted of 60,494 cylindrical airway segments, with 30,243 terminal bronchi subtended by viscoelastic acini. Distributed mechanical properties of tissues and airways were simulated to represent typical healthy and blast-injured lungs, the latter

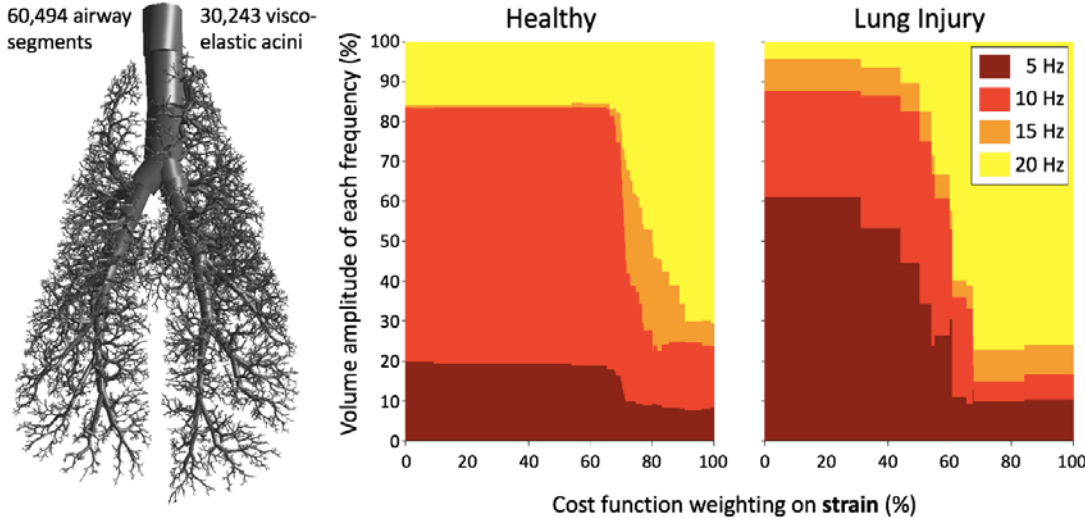


Figure 3: Computational model of porcine lung (left panel). Optimal MFOV volume amplitudes at each frequency are shown for varying cost function emphasis on strain vs. strain rate, in simulated healthy conditions (center panel) and heterogeneous lung injury (right panel).

characterized by bilateral derecruitment and increased tissue stiffness, focusing on the perihilar regions of the model (Figure 4). We found that delivered gas flow was heterogeneously distributed in the blast-injured lung during both conventional mechanical ventilation and high-frequency oscillatory ventilation. During conventional mechanical ventilation, flow was distributed primarily according to local tissue stiffness. At higher frequencies, the distribution of flow became increasingly heterogeneous and frequency-dependent, with some regions being under-ventilated while other regions experienced substantially greater distension. These results were presented in poster form at the 2017 Military Health System Research Symposium in Kissimmee, Florida (8).

Ultimately, our unique modeling and optimization approaches will allow for the selection of patient-specific MFOV waveforms, especially when combined with experimental evidence (Specific Aim 2) to justify physiologically-relevant emphasis on strain vs. strain rate to minimize risk for VILI.

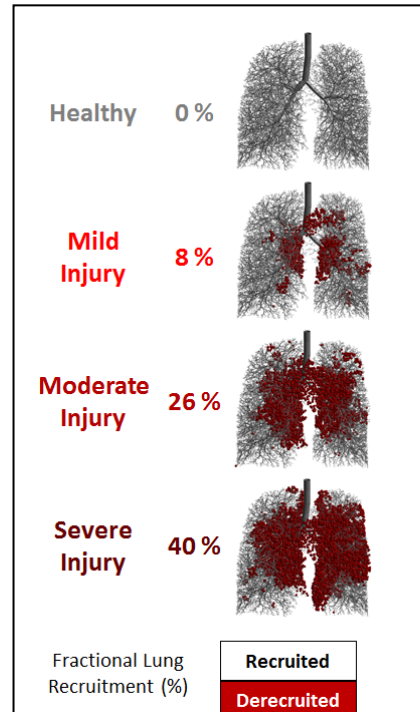


Figure 4: Healthy human airway tree, along with three levels of blast injury, modeled as increasing levels of parenchymal tissue stiffness and acinar derecruitment.

3.2.2 Specific Aim 2

With regard to Specific Aim 2, we have completed seven animal experiments to date, comparing conventional mechanical ventilation (CMV), traditional single-frequency HFOV, and MFOV in anesthetized and paralyzed pigs before and after acute lung injury across several physiologic, imaging, and gas exchange metrics. All experiments have been approved by the University of Iowa Institutional Animal Care and Use Committee (Protocol number 5031314). Measurements of oscillatory input impedance (13) are obtained under baseline conditions and immediately following lung injury. All pigs receive: 1) CMV at a rate of 20 min^{-1} and tidal volume between $10\text{-}12 \text{ mL kg}^{-1}$; 2) HFOV delivered at 5 Hz; and 3) MFOV delivered using uniform flow amplitudes at 5, 10, 15, and 20 Hz. Each ventilatory / oscillatory modality is applied in random order, under baseline conditions and following

lung injury. At the end of each modality period, arterial blood gases are drawn, and CT scans are obtained using a Siemens Somatom Force scanner. Figure 5 shows example transverse, coronal, and sagittal CT images in a representative pig before and after oleic acid-induced lung injury. Similar to clinical ARDS, this injury model is characterized by patchy alveolar edema, along with generalized increased CT density that is greatest in the dependent lung regions.

During the course of these experiments, our group developed a *revolutionary* dynamic CT image reconstruction algorithm to assess intratidal derecruitment and overdistention during CMV and MFOV in these animals with acute lung injury. This frequency-selective CT (FSCT) reconstruction can *identify and track regions of the lung at high risk for additional injury* due to atelectrauma or volutrauma, with unparalleled spatiotemporal resolution. Figure 6 shows variation in regional aeration over the course of a positive pressure CMV breath. Our technique has just recently been published in *IEEE Transactions in Medical Imaging* (4). In collaboration with Drs. Gary E. Christensen and Joseph M. Reinhardt at the University of Iowa, we have applied a novel 4-D image registration technique to our unique FSCT image sequences, to reconstruct temporally-resolved structural deformations during periodic ventilation, along with regional maps of parenchymal expansion and contraction (15). Periodic expansion and contraction are assessed by the discrete Fourier transform of the normalized time-varying Jacobian determinants. Figure 7 shows the distribution of strain amplitudes in a representative pig during HFOV delivered at 5 Hz,

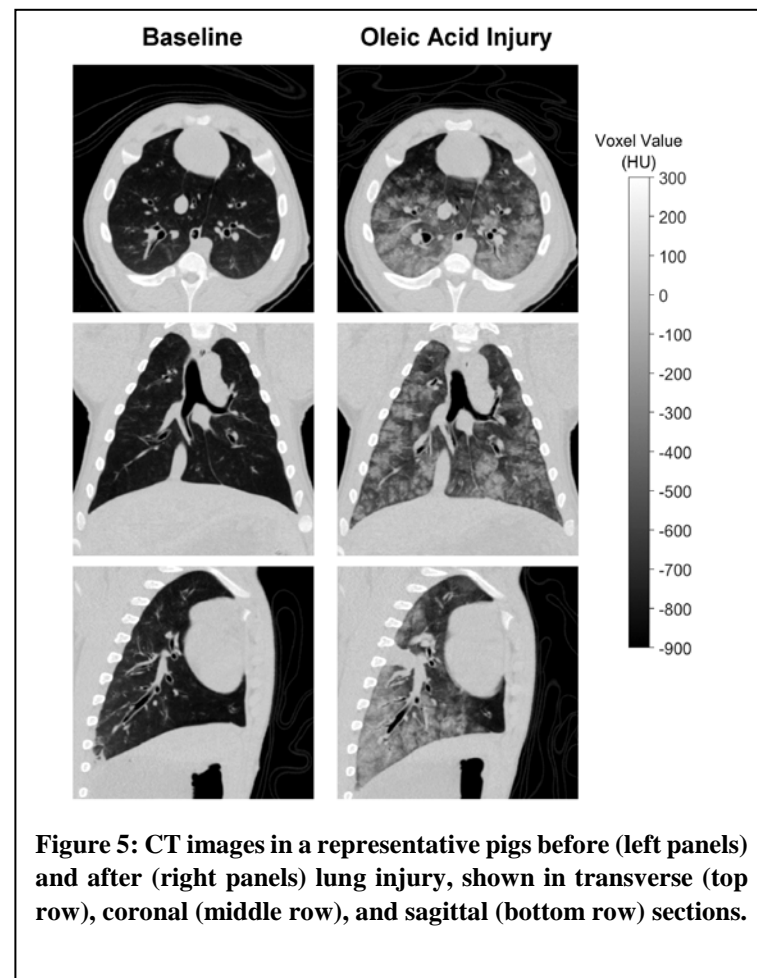
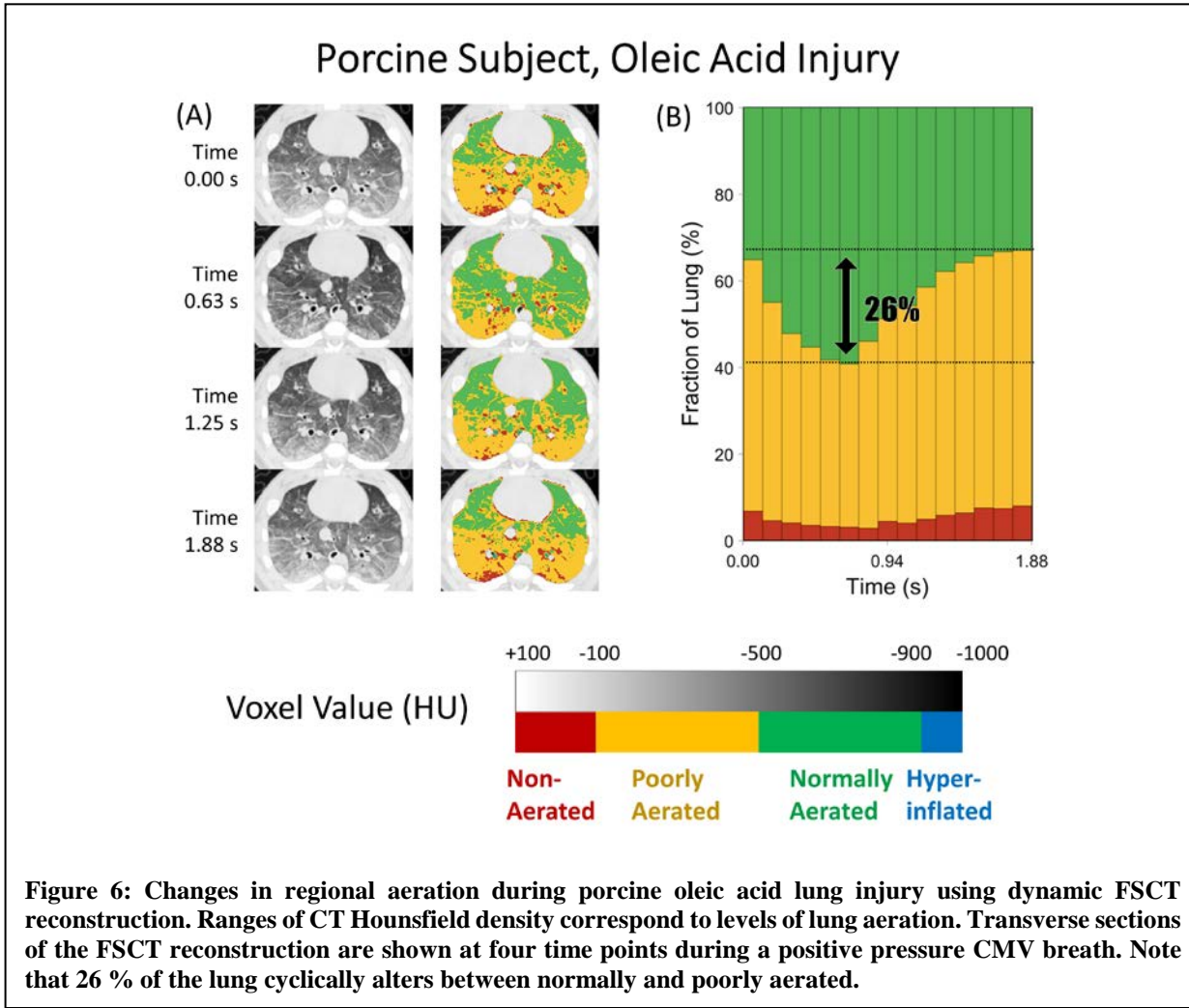
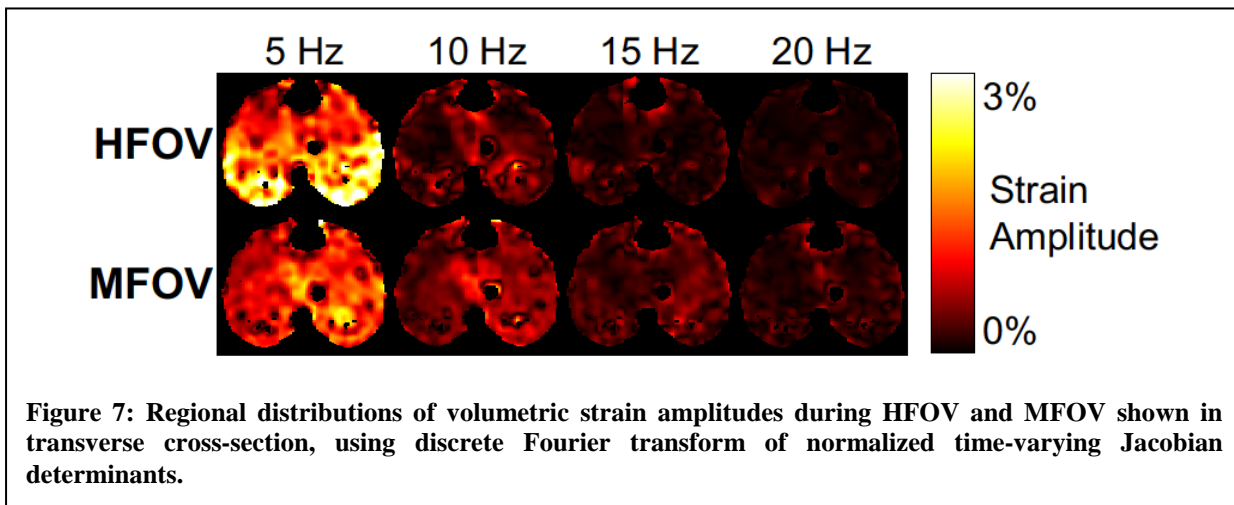


Figure 5: CT images in a representative pigs before (left panels) and after (right panels) lung injury, shown in transverse (top row), coronal (middle row), and sagittal (bottom row) sections.



as well as during MFOV. These distributions tend to vary primarily in the ventral-dorsal direction, in accordance with the gravitational field in supine position. Regional strain amplitudes during MFOV varies with frequency, with different lung regions selectively filtering the harmonic frequency content of the broadband oscillatory flow. Of note, the total volumetric strain (peak-to-



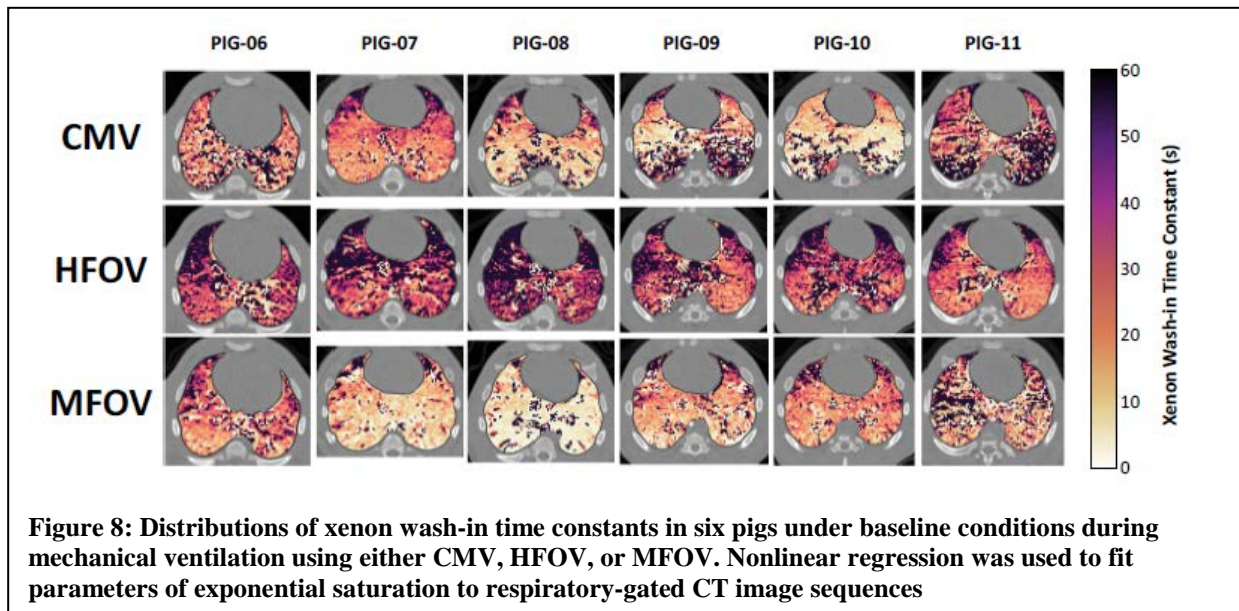


Figure 8: Distributions of xenon wash-in time constants in six pigs under baseline conditions during mechanical ventilation using either CMV, HFOV, or MFOV. Nonlinear regression was used to fit parameters of exponential saturation to respiratory-gated CT image sequences

peak mean \pm standard deviation) during HFOV ($7.9\% \pm 3.1\%$) and MFOV ($6.9\% \pm 2.5\%$) were substantially lower than during CMV ($31.3\% \pm 11.6\%$). Our preliminary results indicate that parenchymal stretch during oscillatory ventilation is regionally heterogeneous and frequency-dependent. Moreover, the broadband spectral content associated with MFOV may enhance gas transport in the presence of periodic parenchymal deformation with higher harmonics. Such behavior may be further adjusted to compensate for patient-specific regional heterogeneity. These results will be presented at the 2017 meeting of the Biomedical Engineering Society in Phoenix, Arizona (7).

In conjunction with the FSCT imaging described above, we also acquired timed sequences of CT images during xenon wash-in and wash-out in each pig to assess regional ventilation distribution. Image acquisition was gated to the periodic mechanical ventilation cycle during CMV, HFOV, or MFOV. All images in each sequence were pairwise registered to their respective initial images, to compensate for non-respiratory sources of motion such as cardiogenic oscillations. Regions of interest were defined as cubes spanning four voxels on each side. Within each region of interest, nonlinear regression was used to fit exponential saturation or decay curves to a time series of spatially-averaged voxel intensities during xenon wash-in or wash-out, respectively. Figure 8 shows representative slices from xenon wash-in image analysis performed in six pigs under baseline conditions. These results demonstrate the feasibility of our XeCT imaging protocol in healthy subjects, and furthermore suggest noticeable qualitative differences in the distribution of xenon equilibration time constants between the ventilation modalities. In particular, *gas transport during MFOV appears to be least affected by gravitational forces compared to CMV or HFOV*. Additionally, HFOV tends to produce larger time constants than CMV or MFOV, suggesting overall slower rates of xenon equilibration during HFOV.

3.3 Opportunities for Training and Professional Development

Jacob Herrmann, M.S., is currently a Ph.D. candidate in the Department of Biomedical Engineering at the University of Iowa, and has been working under the direct supervision of Dr. Kaczka on all aspects of this project. Mr. Herrmann has assisted with all animal experiments to date, and has been managing the analyses for the CT imaging and impedance data in pigs. As a part of his Ph.D. research, he has developed the dynamic FSCT image reconstruction algorithm to quantify lung parenchymal motion during mechanical ventilation and oscillation (4), as well as 4-D image registration to assess mechanical strain heterogeneity in the injured porcine lungs. Along with our consultant Dr. Merryn Tawhai of the University of Auckland, Mr. Herrmann has developed a three-dimensional computational model of a porcine lung with high anatomic fidelity, based on a central airway tree segmented from a CT image of a supine pig. Simulations of ventilation distribution using this model has been crucial to our understanding how MFOV enhances gas exchange in the injured lung, and how spectral content of MFOV waveforms can be further optimized according to the relative contributions of acinar strain vs. strain rate. During the first year of this grant, Mr. Herrmann has been the first author of two publications (4, 11), and has another manuscript in press (10).

3.4 How were the results disseminated to the communities of interest?

We have published one article (11) and have another article (10) accepted for publication in the *Journal of Applied Physiology*. The audience for this journal consists mostly of organ-level physiologists and biomedical engineers. Our paper focusing on the FSCT technique (4) was published in *IEEE Transactions in Medical Imaging*, with an audience of clinical radiologists, imaging scientists, and medical physicists. Our work from this contract has also been presented at meetings of the Biomedical Engineering Society (1, 7, 9), the American Thoracic Society (3), the Association of University Anesthesiologists (5), the International Flow-Volume Underworld Meeting (2, 12) and the Military Health System Research Symposium (8).

3.5 What do you plan to do during the next reporting period to accomplish the goals?

We plan to finish the experimental protocols in the three remaining pigs. We are now in the ongoing process of analyzing and comparing all gas exchange data, physiological variables and indices, as well as dynamic CT imaging data. A very time consuming process is the segmentation of CT images of the injured pig lungs, since the Hounsfield density of parenchymal consolidation and edema fluid are difficult to distinguish from other chest wall structures. This makes semi-automatic segmentation algorithms ineffective, and we must rely on manual segmentation. However, we expect to have this completed by the closeout of the final progress report.

4.0 IMPACT

4.1 What was the impact on the development of the principal discipline of the project?

MFOV a promising and innovative approach to lung protective ventilation, and its use in patients will require considerable work to understand its application in pathophysiologies relevant to ARDS and other forms combat-related lung injury. The mechanical heterogeneity of the injured lung has important implications for optimal ventilation protocols and treatment strategies. The novel modeling, experimental, and imaging techniques detailed in this progress report address fundamental questions regarding the mechanism by which MFOV improves gas exchange

compared to CMV or traditional HFOV. *The immediate, short-term impact of this project is the development of MFOV waveforms that have far more potential to reduce the risk of ventilator-associated lung injury compared to CMV*, as well as a mechanistic understanding of gas transport during oscillatory ventilation. Our work also provides a requisite, scientific basis for the eventual use of MFOV in patients, since our results are easily translatable and testable in human clinical trials. MFOV will have *long-term impact on guiding therapeutic and technological developments for future research in ARDS*, with potential to significantly impact the morbidity and mortality associated with this deadly syndrome.

4.2 What was the impact on other disciplines?

As detailed in Section 3.0 of this progress report, our new frequency-selective CT (FSCT) dynamic image reconstruction algorithm enables imaging of both low- and high-frequency dynamic periodic motions at specified frequencies, with minimal extraneous motion artifact. This FSCT approach offers improved imaging fidelity of dynamic subject motion compared to more conventional prospective or retrospective gating approaches. The characterization of dynamic deformations of thoracic structures will have *enormous impact in the fields of clinical radiology and cardiac imaging*. When combined with image registration techniques, FSCT may provide detailed four-dimensional information of distributed tissue deformation of anatomic structures previously inaccessible using standard reconstruction approaches.

4.3 What was the impact on technology transfer?

Nothing as yet to report

4.4 What was the impact on society beyond science and technology?

ARDS has a major impact in the United States, with an estimated 190,000 cases and 74,000 deaths annually. Significant reductions in mortality have been realized by the use of lung protective mechanical ventilation protocols in which PEEP is used to recruit the lung and prevent repetitive end-expiratory opening and closing of airspaces, and smaller tidal volumes prevent end-inspiratory over-distension. *MFOV represents a promising and innovative approach to lung protective ventilation*, although its use in patients will require considerably more work to understand its application in pathophysiologies relevant to ARDS and combat-related lung injury. *This project will ultimately provide a solid, scientific basis for the rational use of this MFOV in critically ill patients*. The thrust of this DoD CDMRP contract is to demonstrate that MFOV results in improved gas exchange while minimizing additional injury in an animal model of combat-related lung injury. However, *MFOV may have more far-reaching implications for both pulmonary medicine and anesthesia*. For example, MFOV may not be limited to a treatment solely for ARDS, but may be utilized in the ventilator management of other heterogeneous lung diseases, such as asthma, COPD, or pneumonia. The possibility that MFOV can more efficiently penetrate ‘difficult-to-reach’ regions of the lung also has implications for the *optimal delivery of aerosols and drugs, such as beta agonists, steroids, or even inhaled volatile anesthetics*.

5.0 CHANGES / PROBLEMS

5.1 Changes in approach and reasons for change

Our original experimental protocol indicated that four ventilatory / oscillatory modalities would be used in each animal: 1) CMV; 2) single-frequency HFOV; 3) a generic MFOV consisting of uniform flow amplitudes (or hyperbolically-decreasing volume amplitudes); and 4) a custom-designed MFOV waveform based on the modeling and simulation results of Specific Aim 1. However, our computer modeling results indicated that an MFOV waveform consisting of hyperbolically-decreasing volume amplitudes provided a near-optimal solution for most levels of lung injury (Figure 3). Thus, we were able to simplify our experimental protocol using only three modalities, since our original generic MFOV waveform was found to be optimal. This was a relatively minor change to our initial experimental design.

5.2 Actual or anticipated problems or delays and actions or plans to resolve them

Nothing to report

5.3 Changes that had a significant impact on expenditures

Nothing – we are within our budget, despite doing more experiments than planned in the first year. As detailed in Section 5.1, the experimental protocol was simplified from comparing four ventilatory modalities to just three, since our ‘generic’ MFOV waveform yielded optimal solutions based on our computer modeling. Thus the duration for each experiment was shortened, and thus reduced expenditures. We budgeted for 3 experiments in Year 1 and 7 experiments in Year 2, however, we were able to get completed protocols in 7 experiments in Year 1 with sufficient budget for 4-5 more experiments in Year 2. Analysis of the completed experiments from Year 1 is continuing into Year 2.

Budget category	Total budget	Cumulative Expenditures for Year 1	Remaining for Year 2
Animal experiment costs (7 experiments)	\$76,982.50	\$55,642.45	\$21,340.05

5.4 Significant changes in the use or care of human subjects, vertebrate animals, biohazards, and/or select agents

Nothing to report.

6.0 PRODUCTS

6.1 Journal Publications

Herrmann J, Tawhai MH, and Kaczka DW. Regional gas transport in the heterogeneous lung during oscillatory ventilation. *Journal of Applied Physiology* 121: 1306-1318, 2016;
Acknowledgement of federal support: yes

Herrmann J, Hoffman EA, and Kaczka DW. Frequency-Selective Computed Tomography: Applications During Periodic Thoracic Motion. *IEEE Trans Med Imaging* 36: 1722-1732, 2017; Acknowledgement of federal support: yes

Herrmann J, Tawhai MH, and Kaczka DW. Parenchymal strain heterogeneity during oscillatory ventilation: Why two frequencies are better than one. *Journal of Applied Physiology* (in press); Acknowledgement of federal support: yes

6.2 Books or other non-periodical, one-time publications

Nothing to report

6.3 Other Publications, Conference Papers, and Presentations

Herrmann J, and Kaczka DW. Optimization of Spectral Content in Oscillatory Ventilator Waveforms. In: *2016 Annual Meeting of the Biomedical Engineering Society*. Minneapolis, MN: 2016. Acknowledgement of federal support: yes

Herrmann J. What can frequency-selective CT imaging show us about regional lung deformation? *Flow-Volume Underworld*, Boston, MA, 2017. Acknowledgement of federal support: yes

Kaczka DW. Parenchymal Strain During Oscillatory Ventilation: Why Two Frequencies are Better than One. *Flow-Volume Underworld*, Boston, MA, 2017. Acknowledgement of federal support: yes

Herrmann J, and Kaczka DW. Minimizing Parenchymal Strain Heterogeneity During Oscillatory Ventilation. In: *Association of University Anesthesiologists 64th Annual Meeting*. Washington, D.C.: 2017. Acknowledgement of federal support: yes

Herrmann J, Fuld MK, Hoffman EA, and Kaczka DW. Temporally Resolved Computed Tomographic (CT) Imaging to Assess Regional Parenchymal Strain during Oscillatory Ventilation. *2017 Meeting of the American Thoracic Society. American Journal of Respiratory and Critical Care Medicine* 2017; 195:A6522. Acknowledgement of federal support: yes

Herrmann J, Shao W, Reinhardt J, Hoffman E, Christensen G, and Kaczka DW. Frequency-Selective CT Image Registration for Assessment of Regional Periodic Lung Deformation. *2017 Meeting of the Biomedical Engineering Society*, Phoenix AZ, Acknowledgement of federal support: yes

Herrmann J, Tawhai M, and Kaczka DW. Multi-Objective Optimization of Multi-Frequency Oscillatory Ventilation. *2017 Meeting of the Biomedical Engineering Society*, Phoenix AZ, Acknowledgement of federal support: yes

Hadjarevic B, Herrmann J, Kaczka DW. Modeling the Frequency Response of a Proportional Solenoid Valve for Oscillatory Ventilation. *2017 Meeting of the Biomedical Engineering Society*, Phoenix AZ, Acknowledgement of federal support: yes

6.4 Website or other Internet site

<https://www.researchgate.net/project/Optimizing-Ventilation-Distribution-and-Gas-Exchange-in-Combat-Related-Lung-Injury-Using-Multi-Frequency-Oscillation>

6.5 Technologies or techniques

Nothing to report

6.6 Inventions, patent applications and/or licenses

Nothing to report

6.7 Other Products

Nothing to Report

7.0 PARTICIPANTS & OTHER COLLABORATING ORGANIZATIONS

7.1 What individuals have worked on the project?

Name:	David W. Kaczka, M.D., Ph.D.
Project Role:	Principal Investigator
Researcher Identifier (ORCID ID):	0000-0003-4378-5242
Nearest person month worked:	3.2
Contribution to Project:	Dr. Kaczka is responsible for the overall direction of the project as well as the experimental measurements of lung impedance and CT imaging. Dr. Kaczka is responsible for oversight of all publications and presentations related to the project. Dr. Kaczka supervised and participated in the animal experiments with Mr. Jacob Herrmann (Ph.D. student).
Funding Support:	NIH

Name:	Jacob Herrmann, M.S.
Project Role:	Graduate Student
Researcher Identifier (ORCID ID):	0000-0001-5046-5592
Nearest person month worked:	12
Contribution to Project:	Mr. Herrmann has performed the computational modeling for assessment of gas transport and exchange in porcine lungs in collaboration with Dr. Kaczka and Dr. Tawhai. He has also assisted in the animal experiments and analysis of the imaging and impedance data.
Funding Support:	University of Iowa, Department of Anesthesia

Name:	Merryn Tawhai, Ph.D.
Project Role:	Consultant
Researcher Identifier (ORCID ID):	0000-0002-3211-6337
Nearest person month worked:	160 hours over Year 1 (1.0 person month)
Contribution to Project:	Advisor for modeling projects in Year 1, completed
Funding Support:	NIH, Royal Society of New Zealand, Health Research Council of New Zealand, The Tertiary Education Commission of New Zealand

Name:	Eric Hoffman, Ph.D.
Project Role:	Co-Investigator
Researcher Identifier (ORCID ID):	0000-0001-8456-9437
Nearest person month worked:	0.6
Contribution to Project:	Dr. Hoffman closely collaborated in all aspects of the computational modeling, animal experiments, CT scanning and image processing
Funding Support:	NIH

7.2 Has there been a change in the active other support of the PI or key personnel since the last reporting period?

The PI, David Kaczka, MD, PhD, has added effort on two projects, however overall research effort is unchanged from 60% research effort, 40% clinical effort. There is no overlap between the current project and these projects.

2015-2019 NIH/NHLBI 1R01HL126838
 "Defining the Role of Early Pulmonary Vascular Disease in COPD"
 Role: Co-Investigator 10% FTE
 This project evaluates the role of imaging-based measures of pulmonary vascular structure and function to identify smokers at risk of rapid emphysema progression and/or at risk of having frequent acute exacerbations of their COPD.

2012-2017 NIH 5R01HL112986
 "Multi-Center Structural & Functional Quantitative CT Pulmonary Phenotyping"
 Role: Co-Investigator 10% FTE
 This bioengineering research partnership takes advantage of emerging acquisition technique of multi-spectral computed tomography (dual energy CT: DECT), careful evaluation of dose lowering methods, and novel approaches to statistical cluster analysis to expand the biomarkers used in multi-center studies to identify sub-populations of lung disease.

The Co-I, Eric Hoffman, PhD, has modified his effort on various NIH projects. There is no overlap between the current project and any of his other projects.

7.3 What other organizations were involved as partners?

Organization Name: University of Auckland

Location of Organization: Auckland, New Zealand

Partner's contribution to the project: Consultant, Merryn Tawhai, Ph.D.

Dr. Tawhai advised Dr. Kaczka and Mr. Herrmann on aspects of the modeling that was completed in Year 1. Her commitment was as expected and the full budget of \$11,840 had been paid. No further effort is required by Dr. Tawhai on this project.

8.0 SPECIAL REPORTING REQUIREMENTS

Nothing to report

9.0 REFERENCES

1. **Hajdarevic B, Herrmann J, and Kaczka DW.** Modeling the Frequency Response of a Proportional Solenoid Valve for Oscillatory Ventilation. *2017 Meeting of the Biomedical Engineering Society* 2017.
2. **Herrmann J.** What can frequency-selective CT imaging show us about regional lung deformation? *2017 Meeting of the Flow-Volume Underworld Boston, MA* 2017.
3. **Herrmann J, Fuld MK, Hoffman EA, and Kaczka DW.** Temporally Resolved Computed Tomographic (CT) Imaging to Assess Regional Parenchymal Strain during Oscillatory Ventilation. *American Journal of Respiratory and Critical Care Medicine* 195: A6522, 2017.
4. **Herrmann J, Hoffman EA, and Kaczka DW.** Frequency-Selective Computed Tomography: Applications During Periodic Thoracic Motion. *IEEE Transactions on Medical Imaging* 36: 1722-1732, 2017.
5. **Herrmann J, and Kaczka DW.** Minimizing Parenchymal Strain Heterogeneity During Oscillatory Ventilation. In: *Association of University Anesthesiologists 64th Annual Meeting*. Washington, D.C.: 2017.
6. **Herrmann J, and Kaczka DW.** Optimization of Spectral Content in Oscillatory Ventilator Waveforms. In: *2016 Annual Meeting of the Biomedical Engineering Society*. Minneapolis, MN: 2016.
7. **Herrmann J, Shao W, Reinhardt J, Hoffman EA, Christensen G, and Kaczka DW.** Frequency-Selective CT Image Registration for Assessment of Regional Periodic Lung Deformation. *2017 Meeting of the Biomedical Engineering Society, Phoenix AZ* 2017.
8. **Herrmann J, Tawhai MH, and Kaczka DW.** Computational Modeling of Primary Blast Lung Injury: Implications for Ventilator Management. In: *Military Health System Research Symposium*. Kissimmee, FL: 2017.
9. **Herrmann J, Tawhai MH, and Kaczka DW.** Multi-Objective Optimization of Multi-Frequency Oscillatory Ventilation. *2017 Meeting of the Biomedical Engineering Society, Phoenix AZ* 2017.
10. **Herrmann J, Tawhai MH, and Kaczka DW.** Parenchymal strain heterogeneity during oscillatory ventilation: Why two frequencies are better than one. *Journal of Applied Physiology* (in press).
11. **Herrmann J, Tawhai MH, and Kaczka DW.** Regional gas transport in the heterogeneous lung during oscillatory ventilation. *Journal of Applied Physiology* 121: 1306-1318, 2016.
12. **Kaczka DW.** Parenchymal Strain During Oscillatory Ventilation: Why Two Frequencies are Better than One. *2017 Meeting of the Flow-Volume Underworld, Boston MA* 2017.
13. **Kaczka DW, and Dellaca RL.** Oscillation mechanics of the respiratory system: applications to lung disease. *Critical Reviews in Biomedical Engineering* 39: 337-359, 2011.
14. **Kaczka DW, Herrmann J, and Tawhai MH.** Parenchymal Strain Versus Strain Rate During Multi-Frequency Oscillatory Ventilation. In: *American Society of Anesthesiologists*. Boston, MA: 2017.
15. **Zhao B, Christensen GE, Song JH, Pan Y, Gerard SE, Reinhardt JM, Du K, Patton T, Bayouth JM, and Hugo JD.** Tissue-volume preserving deformable image registration for 4DCT pulmonary images. *Proceedings of the 2016 IEEE Conference on Computer Vision and Pattern Recognition Workshops* 41-49, 2016.

10.0 APPENDICES

Text from References 1, 3-11 and 14 are enclosed in the same order as the listing above. Number 2 and 12 are talks from a conference that does not publish abstracts.

Modeling the Frequency Response of a Proportional Solenoid Valve for Oscillatory Ventilation

Bakir Hajdarevic¹, Jacob Herrmann¹, and David Kaczka¹

¹University of Iowa, Iowa City, IA

Introduction: Proportional solenoid (PSOL) valves are an important component of modern mechanical ventilators^[1]. However the use of PSOL valves in high frequency oscillators is limited due to incomplete characterization of their dynamic responses, as well as the necessity to incorporate them into sophisticated closed-loop systems for precise airway pressure control and patient safety^[2]. The goal of this study was to characterize the dynamic response of high-flow PSOL valve using a linear transfer function, which may allow for robust simulation and design of closed-loop controllers for various ventilatory and oscillatory modalities in patients.

Materials and Methods: Measurements were made in an ASCO Posiflow™ PSOL valve (Model SD8202G027V) connected in series to a Bellofram Type 70 Air Regulator (960-131-010). Maximum orifice diameter of the valve was 7 mm, allowing for a steady peak flow delivery of 4.7 L sec⁻¹. Pulse width modulated (PWM) current to the PSOL coil was provided by ASCO's Electronic Control Unit (ECU Model 8908A001) at a frequency of 300 Hz. A digital-to-analog (D/A) converter (USB-6008, National Instruments) was used to generate bandlimited white noise (0.01-40 Hz), as well as three different pseudorandom signals consisting of discrete sinusoids at mutually prime frequencies (0.195-37.4 Hz). The output of the D/A converter was low pass filtered at 40 Hz (8-pole Butterworth), and presented as the input control voltage to the ECU. Output flow from the PSOL valve was measured with a pneumotachograph (Hans Rudolph 4700A) coupled to a 0-2 cmH₂O differential pressure transducer (Celesco LCVR-0002). Both the input voltage and output flow waveforms were low pass filtered at 40 Hz, and sampled by an analog-to-digital converted at 100 Hz. The voltage-flow transfer function of the combined ECU-PSOL system was determined using an overlap-average periodogram technique, which was then fitted to a generalized parametric transfer function of the form:

$$T(s) = K \prod_{m=1}^M (s + \alpha_m) / \prod_{n=1}^N (s + \beta_n) \quad (1)$$

where α_m and β_n denote the zeroes and poles, respectively, of $T(s)$, and $M \leq N$. The parameters K , α_m , and β_n were estimated using a nonlinear gradient search technique (MATLAB v9.0, The Mathworks Inc.). The optimal number of zeros and poles for the ECU-PSOL system (M, N) were determined based on the Akaike information criterion (AIC).

Results and Discussion: The PSOL valve exhibited a steady-flow hysteresis of ~18%, while its dynamic magnitude and phase responses were flat out to 10 Hz (Figure 1). Broadband measurement of total harmonic flow distortion^[3] was approximately 11%. The frequency response of the ECU-PSOL system was adequately described by Equation 1 with $M = 3$ and $N = 5$.

Conclusions: The dynamic frequency response of a high-flow PWM PSOL valve can be adequately described using a linear polynomial transfer function. Such a characteristic will allow for robust simulation and design of a closed-loop controller in a device capable of generating various ventilatory and oscillatory modalities in patients with acute respiratory failure.

Acknowledgements: Work supported in part by U.S. Department of Defense grant PR151761

References:

- [1] Lua AC, Shi KC, and Chua LP. *Med Eng Phys* 23: 381-389, 2001.
- [2] Kaczka DW, and Lutchen KR. *Ann Biomed Eng* 32: 596-608, 2004.
- [3] Zhang, Q., B. Suki, and K. R. Lutchen. *Ann. Biomed. Eng.* 23:672–681, 1995.

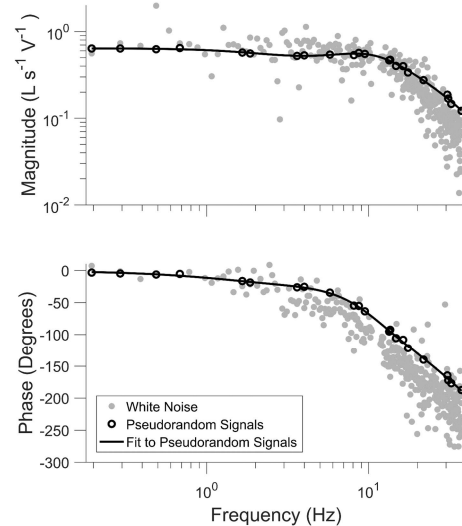


Figure 1 Frequency response of PSOL valve driven with white noise (gray symbols) and pseudorandom signal (black symbols) inputs, along with corresponding fit of Equation 1 to pseudorandom data (solid lines).

2017 Meeting of the American Thoracic Society

Abstract 6518

Temporally-Resolved Computed Tomographic (CT) Imaging to Assess Regional Parenchymal Strain during Oscillatory Ventilation

Type: Scientific Abstract

Topic: 20. Mechanical Ventilation (Invasive, Non-Invasive) / Adult / Translational Science / Respiratory Structure and Function (RSF)

Authors: J. Herrmann¹, M.K. Fuld², E.A. Hoffman³, D.W. Kaczka¹; ¹University of Iowa - Iowa City, IA/US, ²Siemens Medical Solutions USA, Inc. - Malvern, PA/US, ³University of Iowa Carver College of Medicine - Iowa City, IA/US

Abstract Body

Rationale:

We have recently proposed the use of multi-frequency oscillatory ventilation (MFOV) as a modification of high frequency oscillatory ventilation (HFOV) for improving ventilation distribution and minimizing ventilator-induced lung injury (Kaczka et al., *Anesthesiology* 123(6):1394-1403, 2015). Direct observation of dynamic regional strain during MFOV is not possible using conventional X-ray CT imaging, due to motion artifact blurring and extraneous cardiogenic disturbances. These artifacts are especially problematic during oscillation at frequencies greater than the rotation frequency of the X-ray source and detector array. In this study, we developed a reconstruction algorithm for spatial and temporal resolution of periodic lung motion during CT scanning, enabling quantification of regional parenchymal strain during HFOV or MFOV.

Methods:

Sedated and paralyzed pigs received mechanical ventilation (conventional, HFOV, or MFOV) using ventilatory frequencies between 0.4 to 20 Hz (i.e., 24 to 1200 min⁻¹). CT projections were acquired continuously for 30 to 100 seconds using a SOMATOM Force scanner (Siemens Healthineers, Forchheim, Germany) rotating at 4 Hz, using 80 kVp and 150 mAxs (total dose per acquisition between 345 to 1152 mGy). CT projections were reorganized according to oscillatory frequency before cone-beam reconstruction, yielding a series of volumetric images (isotropic 0.3 mm voxel size, 192 slices, 240 mm field-of-view) at 10 distinct time-points during periodic motion, with minimal extraneous motion artifact. Piecewise four-dimensional image registration was used to determine spatial parenchymal deformation between consecutive time-points.

Results:

Our reconstruction algorithm produced image sequences of clearly defined lung structure at distinct time points throughout the oscillatory ventilation cycle (Figure 1). Substantial reductions in reconstruction error were achieved for the longest scanning durations. Cardiogenic oscillations resulted in minor motion artifact due to the oscillatory frequency not being an integer multiple of heart rate. Image registration revealed heterogeneous distributions of parenchymal strain magnitudes and phases during oscillatory ventilation.

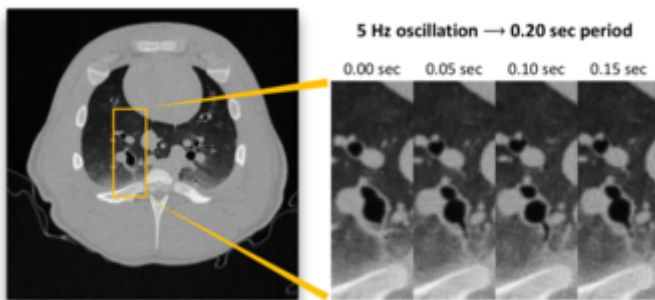
Conclusions:

We have developed a novel method for reconstructing temporally resolved images of oscillatory lung deformation during continuous X-ray CT acquisition, with minimal distortion from extraneous motion. Our method, coupled with image registration techniques, enables direct, non-invasive quantification of regional parenchymal strain *in vivo* during high frequency and multi-frequency oscillatory ventilation.

Acknowledgements:

The authors thank Siemens Healthineers (Forchheim, Germany) for technical assistance. The authors also acknowledge support from U.S. Department of Defense grant PR151761, and from National Institutes of Health grants 1S10OD018526 and 5R01HL112986.

Reconstructed images of a pig during post-mortem oscillatory ventilation at 5 Hz.



[Print](#)

Frequency-Selective Computed Tomography: Applications During Periodic Thoracic Motion

Jacob Herrmann, *Student Member, IEEE*, Eric A. Hoffman, *Member, IEEE*,
and David W. Kaczka*, *Member, IEEE*

Abstract— We seek to use computed tomography (CT) to characterize regional lung parenchymal deformation during high-frequency and multi-frequency oscillatory ventilation. Periodic motion of thoracic structures results in artifacts of CT images obtained by standard reconstruction algorithms, especially for frequencies exceeding that of the X-ray source rotation. In this paper, we propose an acquisition and reconstruction technique for high-resolution imaging of the thorax during periodic motion. Our technique relies on phase-binning projections according to the frequency of subject motion relative to the scanner rotation, prior to volumetric reconstruction. The mathematical theory and limitations of the proposed technique are presented, and then validated in a simulated phantom as well as a living porcine subject during oscillatory ventilation. The 4-D image sequences obtained using this frequency-selective reconstruction technique yielded high-spatiotemporal resolution of the thorax during periodic motion. We conclude that the frequency-based selection of CT projections is ideal for characterizing dynamic deformations of thoracic structures that are ordinarily obscured by motion artifact using conventional reconstruction techniques.

Index Terms— Heart, image acquisition, image reconstruction – analytical methods, lung, motion compensation and analysis, tracking (time series analysis), X-ray imaging and computed tomography.

GLOSSARY OF NOMENCLATURE

FSCT	Frequency-selective computed tomography.
f_{rot}	Frequency of scanner rotation.
f_{sub}	Frequency of subject motion.
k	Index.
n_{bin}	Index of subject phase bin.
n_{pro}	Index of projection angle.
N_{bin}	Number of subject phase bins.
N_{pro}	Number of projections acquired per scanner rotation.

Manuscript received February 6, 2017; revised April 9, 2017; accepted April 10, 2017. Date of publication April 18, 2017; date of current version July 30, 2017. This work was supported in part by the U.S. Department of Defense under Grant PR151761 and in part by the National Institutes of Health under Grant S100D018526 and Grant R01HL112986. Asterisk indicates corresponding author. (Corresponding author: David W. Kaczka.)

J. Herrmann and E. A. Hoffman are with The University of Iowa, Iowa City, IA 52242 USA.

*D. W. Kaczka is with The University of Iowa, Iowa City, IA 52242 USA (e-mail: david-kaczka@uiowa.edu).

Color versions of one or more of the figures in this paper are available online at <http://ieeexplore.ieee.org>.

Digital Object Identifier 10.1109/TMI.2017.2694887

N_{rot}	Total scanning duration, measured in number of scanner rotations.
p	Index of sequentially acquired projections.
R_{pro}	Number of projections acquired before repetitious sampling.
R_{rot}	Number of scanner rotations completed before repetitious sampling.
R_{sub}	Number of subject motion cycle completed before repetitious sampling.
t	Time.
t_k	Times corresponding to the same subject phase.
t_p	Time of acquisition for p^{th} projection.
π	Number of radians in a semi-circle.
ϕ_{rec}	Reconstructed phase of subject motion.
ϕ_{rot}	Phase of scanner rotation.
ϕ_{sub}	Phase of subject motion.

I. INTRODUCTION

SEVERAL imaging modalities are available to provide four-dimensional descriptions of transient tissue deformations (i.e., three spatial dimensions, one temporal dimension) [1]. X-ray computed tomography (CT) is often used in this regard due to its excellent spatial resolution, despite the risks associated with the use of ionizing radiation [2]. However scanner rotation speed limits temporal resolution using standard image reconstruction algorithms [3]. This may limit the quality of images during dynamic subject motion, especially for deformations at high frequencies. As a result, temporally-resolved imaging during rapid, periodic motion, e.g., high-frequency and multi-frequency oscillatory ventilation [4], [5], is difficult to acquire. Especially with faster rotation times, larger axial coverage, and the ability to significantly reduce radiation exposure utilizing newly emerging CT technologies [6], [7], there is a renewed interest in assessing dynamic physiologic phenomena via CT.

With CT imaging, the X-ray source and detector array rotate about the subject, while X-rays are projected at varying angles. The resulting projections on the opposing detector array are characterized by linear attenuation coefficients, representing the tendency of various biological tissues to absorb or scatter X-rays [8]. The raw data acquired by the scanner comprises projections at multiple angles. A two-dimensional image of the spatially-distributed linear attenuation coefficients can then be obtained by reconstruction of the projection data.

Various reconstruction algorithms are available for clinical purposes, such as filtered back-projection or iterative

reconstruction [9], with each achieving a particular balance between image quality and computational cost. Standard reconstruction algorithms assume that the subject is stationary during scanner rotation, such that each acquired projection captures the same spatial orientation through a different angle. However if the subject is moving during image acquisition, the projection data will contain multiple spatial orientations and projection angles [10]. In such situations, standard reconstruction algorithms will blur the resulting image due to motion artifact [11]. This becomes especially problematic during repetitive periodic motion of anatomic structures at rates equal to or faster than the scanner rotation frequency [4], [12]. Motion artifact mitigation and/or temporally resolved image reconstruction in three dimensions is possible using appropriate gating or triggering techniques [12]. However such techniques selectively target image acquisition at the same subject state repeatedly over the course of multiple motion cycles, rather than acquiring multiple transient states within one cycle.

Image acquisition during periodic subject motion has been well-described in the fields of cardiac and thoracic imaging, for which cardiogenic motion (in the frequency range of 1 to 2 Hz) and spontaneous breathing (0.1 to 0.7 Hz) present sources of motion artifact. Gating techniques for such applications may utilize external signals for either retrospective gating or prospective triggering of the image acquisition cycle. In thoracic CT, a variety of external signals including respiratory flow, pressure, or abdominal motion may be used to target image timing according to lung volume or respiratory phase (i.e., end-expiration and end-inspiration) [13]–[15]. In cardiac CT, an electrocardiogram (EKG) may be used to target image timing according to cardiac phase and heart rate, identifying a period for which the mediastinal contents remain relatively stationary (i.e., diastole) [12], [16]–[18]. However conditions involving highly-dynamic subject states, such as high-frequency oscillatory ventilation (HFOV), do not provide comparable motionless time windows. HFOV is an alternative form of mechanical ventilation that may be used during severe refractory hypoxemia in the Acute Respiratory Distress Syndrome (ARDS). In contrast to conventional forms of mechanical ventilation, HFOV delivers tidal volumes that may be smaller than anatomic dead space, at rates of 2 to 20 Hz [19]. Thus imaging during HFOV has been limited to planar views [20] or phase-averaged volumetric images [4], [21]–[23], resulting in poor spatio-temporal resolution.

To achieve high-resolution CT images during such highly dynamic states, an alternative approach must be implemented that does not rely on the reconstruction of sequentially acquired projections triggered by physiological events [24], [25]. In this study, we propose the use of frequency-selective 4D-CT (FSCT) for capturing periodic subject motion with both high spatial and temporal resolutions. Our approach relies on the continuous acquisition of many projections during multiple scanner rotations over a specified length of axial coverage, followed by a retrospective analysis of the resulting phase distribution of subject motion obtained from projection data.

II. METHODS

A. Theory

Consider an X-ray source rotating through a circular trajectory at frequency f_{rot} , with an opposing detector array acquiring projections at varying angles, during periodic subject motion at frequency f_{sub} . The phase of subject motion ϕ_{sub} can be expressed as a function of time:

$$\phi_{\text{sub}}(t) = (2\pi f_{\text{sub}} t) \bmod 2\pi, \quad t \geq 0 \quad (1)$$

where each distinct value of ϕ_{sub} between 0 and 2π corresponds to a particular spatial orientation, cyclically repeated during the periodic motion. Similarly, the phase of the scanner rotation is:

$$\phi_{\text{rot}}(t) = (2\pi f_{\text{rot}} t) \bmod 2\pi, \quad t \geq 0 \quad (2)$$

where ϕ_{rot} is equivalent to the projection angle relative to the initial projection angle at time $t = 0$. To reconstruct a “still” image of the subject at one particular phase ϕ_{rec} , projections must be acquired at times t_k such that $\phi_{\text{sub}}(t_k) = \phi_{\text{rec}}$:

$$t_k = \frac{\phi_{\text{rec}} + 2\pi k}{2\pi f_{\text{sub}}}, \quad \text{where } k = 0, 1, 2, \dots \quad (3)$$

The relative X-ray projection angle at each t_k is given by:

$$\phi_{\text{rot}}(t_k) = \left[\left(\frac{f_{\text{rot}}}{f_{\text{sub}}} \right) (\phi_{\text{rec}} + 2\pi k) \right] \bmod 2\pi, \quad (4)$$

where $k = 0, 1, 2, \dots$

Multiple distinct “still” images of the subject throughout the periodic motion may be reconstructed by first partitioning subject phase into N_{bin} equally spaced bins on the interval 0 to 2π :

$$n_{\text{bin}} = \begin{cases} 0 & , \quad 2\pi \frac{0}{N_{\text{bin}}} \leq \phi_{\text{sub}} < 2\pi \frac{1}{N_{\text{bin}}} \\ 1 & , \quad 2\pi \frac{1}{N_{\text{bin}}} \leq \phi_{\text{sub}} < 2\pi \frac{2}{N_{\text{bin}}} \\ \vdots & \vdots \quad \vdots \\ N_{\text{bin}} - 1 & , \quad 2\pi \frac{N_{\text{bin}} - 1}{N_{\text{bin}}} \leq \phi_{\text{sub}} < 2\pi \frac{N_{\text{bin}}}{N_{\text{bin}}} \end{cases} \quad (5)$$

and then grouping the sequentially acquired projections according to the corresponding subject phase bin:

$$n_{\text{bin}}(t) = \left\lfloor \left(\frac{\phi_{\text{sub}}(t) N_{\text{bin}}}{2\pi} \right) \bmod N_{\text{bin}} \right\rfloor, \quad t \geq 0 \quad (6)$$

where $\lfloor \cdot \rfloor$ denotes rounding the enclosed argument to the largest integer less than or equal to itself. Equation (6) can be rewritten as:

$$n_{\text{bin}}(t) = \lfloor (f_{\text{sub}} t N_{\text{bin}}) \bmod N_{\text{bin}} \rfloor, \quad t \geq 0 \quad (7)$$

Binning the acquired projections according to subject phase yields N_{bin} sinograms, each containing a sufficient number of angles required for image reconstruction. The phase-binned sinograms may then be reconstructed independently to produce N_{bin} images in a sequence representing dynamic subject state during periodic motion. Each image represents subject state over a limited range of motion characterized by the size of each phase bin. Increasing N_{bin} reduces the size of each

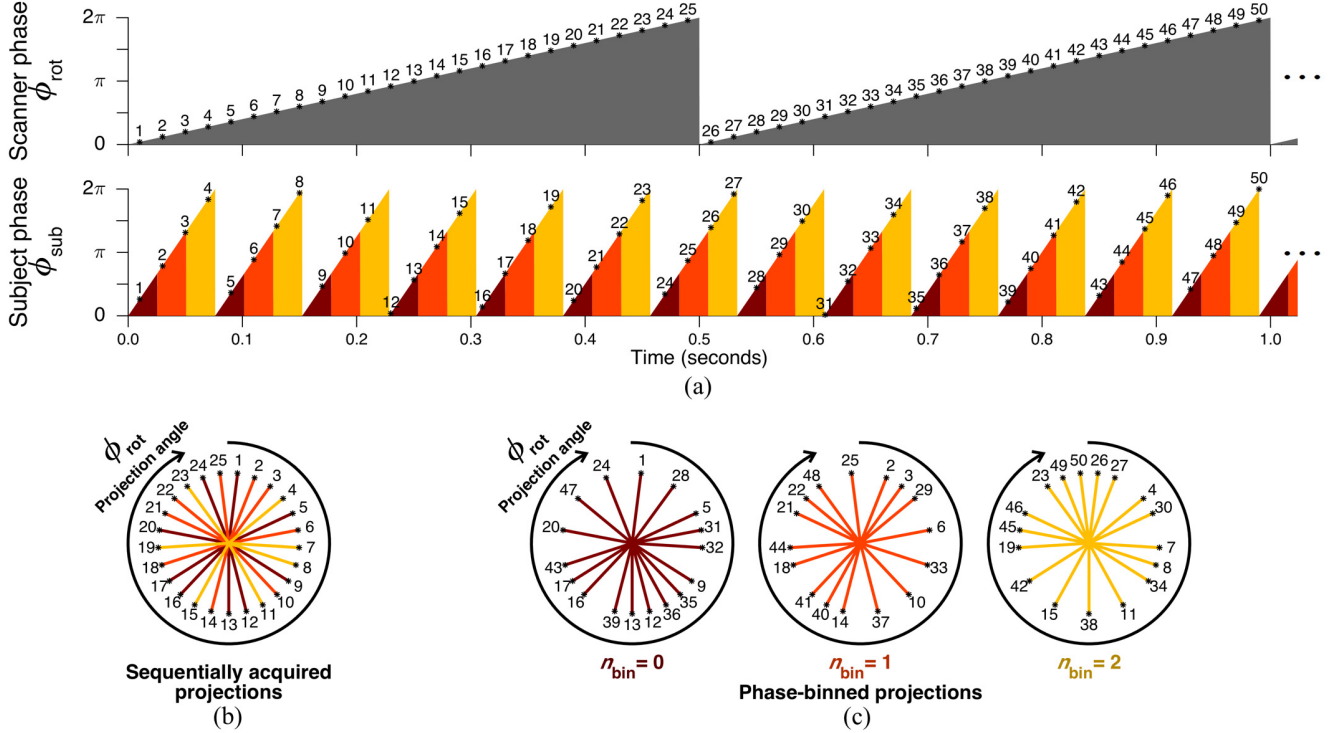


Fig. 1. Illustration of FSCT concept for arbitrarily selected parameters. (a) Scanner phase ϕ_{rot} as a function of time for a 2.0 Hz rotation frequency, with 25 projections acquired per rotation as indicated by numbered asterisks. Projections are numbered according to chronological order of acquisition. Subject phase ϕ_{sub} as a function of time for a 13.13 Hz periodic motion cycle. Subject phase is labeled according to 3 equally sized bins, indicated by color (red, orange, yellow). (b) Standard CT reconstruction is performed on sequentially acquired projections, averaging together variable subject phase acquired throughout one scanner rotation. (c) FSCT reconstruction is performed on phase-binned subsets of projections, each containing a limited range of subject phase.

phase bin, thereby reducing motion artifact in the reconstructed images.

Fig. 1a shows an example of transient variations in subject motion phase during scanner rotation, according to (1) and (2). Standard CT reconstruction is performed on sequentially acquired projections, resulting in variable subject motion phase obtained during one scanner rotation, illustrated in Fig. 1b. FSCT reconstruction is instead performed on subsets of projection data binned according to subject motion phase. Fig. 1c illustrates more uniform subject motion phase obtained in each binned subset of projection data using the FSCT approach described in (5).

B. Feasible Sampling Criterion

In practical applications, the number of unique projection angles is given by the number of projections acquired per scanner rotation N_{pro} . Projections are acquired at a fixed rate and with equal angular spacing throughout each scanner rotation. Therefore projection angle ϕ_{rot} may be considered a discrete variable rather than a continuous function of time, such that ϕ_{rot} for the p^{th} sequentially acquired projection is given by:

$$\phi_{\text{rot}}(p) = \frac{2\pi p}{N_{\text{pro}}} \bmod 2\pi, \quad p = 0, 1, 2, \dots \quad (8)$$

Each unique value of $\phi_{\text{rot}}(p)$ may be indexed by n_{pro} such that:

$$n_{\text{pro}}(p) = p \bmod N_{\text{pro}}, \quad p = 0, 1, 2, \dots \quad (9)$$

Acquisition of the p^{th} projection occurs at time point t_p :

$$t_p = \frac{p}{N_{\text{pro}} f_{\text{rot}}}, \quad p = 0, 1, 2, \dots \quad (10)$$

with subject motion phase:

$$\phi_{\text{sub}}(p) = p \frac{2\pi f_{\text{sub}}}{N_{\text{pro}} f_{\text{rot}}} \bmod 2\pi, \quad p = 0, 1, 2, \dots \quad (11)$$

and subject phase bin index n_{bin} :

$$n_{\text{bin}}(p) = \left\lfloor p \frac{N_{\text{bin}} f_{\text{sub}}}{N_{\text{pro}} f_{\text{rot}}} \bmod N_{\text{bin}} \right\rfloor. \quad (12)$$

Each projection is therefore assigned a pair of indexes $\langle n_{\text{pro}}, n_{\text{bin}} \rangle$ characterizing the associated projection angle and subject motion phase bin. All unique combinations of n_{pro} and n_{bin} must be sampled to appropriately reconstruct the complete image sequence with minimal spatial aliasing, although it is possible to poorly select f_{sub} , f_{rot} , and N_{bin} such that the acquired projections repeat non-unique pairs $\langle n_{\text{pro}}(p), n_{\text{bin}}(p) \rangle$ before complete sampling. The relative periodicity between scanner rotation and subject motion is determined by the number of projection acquisitions which may occur before a repetition in the pair $\langle \phi_{\text{rot}}(p), \phi_{\text{sub}}(p) \rangle$, hereafter referred to as R_{pro} . Projection angle index n_{pro} is periodic in p with period N_{pro} , therefore R_{pro} must be an integer multiple of N_{pro} :

$$R_{\text{pro}} = R_{\text{rot}} N_{\text{pro}} \quad (13)$$

where R_{rot} is the smallest integer number of rotations which may complete before a repetition in $\langle \phi_{\text{rot}}(p), \phi_{\text{sub}}(p) \rangle$ occurs.

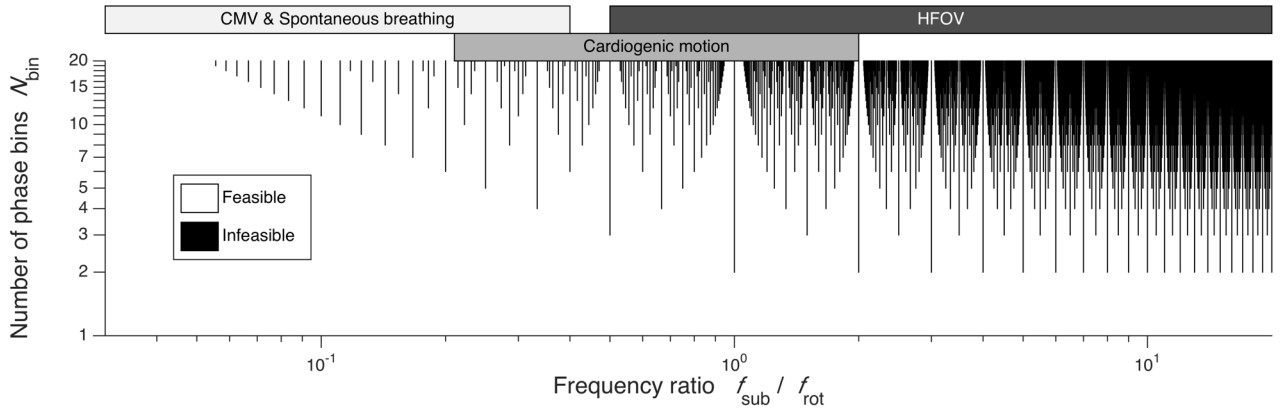


Fig. 2. The space of feasible sampling, showing the combinations of N_{bin} and frequency ratio ($f_{\text{sub}}/f_{\text{rot}}$) for which the projection angles and subject phase bins are either completely (white) or incompletely (black) sampled before repetitive sampling. Parameter selection along the black lines may not provide sufficient sampling for image reconstruction. Typical ranges of f_{sub} and f_{rot} corresponding to conventional mechanical ventilation (CMV), spontaneous breathing, cardiogenic motion, and high-frequency oscillatory ventilation (HFOV) are shown.

Substituting this expression for R_{pro} for p in (11) yields:

$$\phi_{\text{sub}}(R_{\text{pro}}) = \frac{R_{\text{rot}} 2\pi f_{\text{sub}}}{f_{\text{rot}}} \bmod 2\pi \quad (14)$$

Thus the pair $\langle \phi_{\text{rot}}(p), \phi_{\text{sub}}(p) \rangle$ repeats non-unique combinations when an integer number of scanner rotations have completed such that:

$$R_{\text{sub}} = R_{\text{rot}} \frac{f_{\text{sub}}}{f_{\text{rot}}} \quad (15)$$

where R_{sub} is the smallest integer number of motion cycles that may complete before a repetition in $\langle \phi_{\text{rot}}(p), \phi_{\text{sub}}(p) \rangle$ occurs. If f_{sub} and f_{rot} are incommensurable, then no finite values of R_{rot} and R_{sub} exist. Instead, both R_{rot} and R_{sub} will be infinite, since an exact repetition in $\langle \phi_{\text{rot}}(p), \phi_{\text{sub}}(p) \rangle$ will never occur. However if f_{sub} and f_{rot} are commensurable, then R_{rot} may be found by continued fraction expansion [26].

Finally the number of unique pairs $\langle \phi_{\text{rot}}(p), \phi_{\text{sub}}(p) \rangle$ for a given f_{rot} and f_{sub} is limited by an upper bound, determined as the number of projections acquired per scanner rotation N_{pro} multiplied by the number of scanner rotations which may occur before repetition R_{rot} . To ensure that undersampling does not occur, the product $N_{\text{pro}} \cdot R_{\text{rot}}$ must be greater than the total number of samples to be acquired, which is given by the product $N_{\text{pro}} \cdot N_{\text{bin}}$:

$$\frac{N_{\text{pro}} R_{\text{rot}}}{N_{\text{pro}} N_{\text{bin}}} = \frac{R_{\text{rot}}}{N_{\text{bin}}} \geq 1 \quad (16)$$

Note that this feasible sampling criterion does not depend on N_{pro} , but rather only on N_{bin} , f_{rot} , and f_{sub} . Fig. 2 illustrates the space of feasible sampling, given a selection of N_{bin} and frequency ratio ($f_{\text{sub}}/f_{\text{rot}}$). This fractal-like criterion is characterized by the Thomae function, a modified Dirichlet function that is non-zero only at rational values of its argument.

C. Optimal Sampling Condition

The minimum scanning duration for a feasible selection of N_{bin} and frequency ratio ($f_{\text{sub}}/f_{\text{rot}}$) depends on the length of time required to completely sample all unique pairs of phase bin and projection angle. Under ideal circumstances,

each newly acquired projection corresponds to a previously unsampled pair $\langle n_{\text{pro}}(p), n_{\text{bin}}(p) \rangle$, i.e., with minimal redundancy. In this case, the scanning duration measured in number of scanner rotations (N_{rot}) is lower-bounded by the number of motion phase bins:

$$\frac{N_{\text{rot}}}{N_{\text{bin}}} \geq 1 \quad (17)$$

However (17) assumes that the acquired projections uniformly sample both subject phase bins and projection angle bins without redundancy. More generally, the degree of redundant sampling depends on the frequency ratio ($f_{\text{sub}}/f_{\text{rot}}$), as indicated by Fig. 2. Due to the discrete nature of phase-binning, redundant sampling of indices $\langle n_{\text{pro}}(p), n_{\text{bin}}(p) \rangle$ may occur before an exact repetition of phases $\langle n_{\text{pro}}(p), n_{\text{bin}}(p) \rangle$ is encountered. For any choice of N_{bin} , the ideal sampling condition given by (17) is ensured with equality when:

$$\frac{f_{\text{sub}}}{f_{\text{rot}}} = \frac{c}{N_{\text{bin}}} \quad (18)$$

where c is any positive integer such that c and N_{bin} are coprime. If (18) is satisfied, then N_{bin} scanner rotations may be used to reconstruct N_{bin} motion phase bins. Some examples of optimal frequency ratios for desired N_{bin} values are provided in Table I, according to (18). Deviating from the frequency ratios given by (18) may result in substantially increased scanning duration required to properly reconstruct the image sequence.

D. Simulated Phantom

An oscillating imaging phantom was simulated using a Shepp-Logan design [27], with two ellipses modified by sinusoidal oscillations in size, intensity, and/or centroid position at a rate of 9.924 Hz, as shown in Fig. 3. Image size was 256 by 256 pixels. An X-ray CT scanner was simulated with 1000 detectors, 1600 projections per rotation, and 3.509 Hz rotation frequency (285 ms period). These frequencies were chosen to maximize the number of feasible choices for N_{bin} . Projection acquisition was performed using the Radon transform in MATLAB (The Mathworks Inc., Natick, MA),

TABLE I
OPTIMAL SAMPLING CONDITIONS TO MINIMIZE SCANNING DURATION

N_{bin}	Optimal $f_{\text{sub}}/f_{\text{rot}}$ ratio
1	Any
2	$1/2, 3/2, 5/2, 7/2, 9/2, \dots$
3	$1/3, 2/3, 4/3, 5/3, 7/3, \dots$
4	$1/4, 3/4, 5/4, 7/4, 9/4, \dots$
5	$1/5, 2/5, 3/5, 4/5, 6/5, \dots$
:	:
N_{bin}	c/N_{bin} , with c and N_{bin} coprime

Under such conditions, required scanning duration $N_{\text{rot}} = N_{\text{bin}}$.

assuming parallel beam projection and a flat detector array. A total of 224,000 projections over 140 scanner rotations were acquired during continuous phantom oscillation.

Image reconstruction was performed by filtered back-projection using the inverse Radon transform, with linear interpolation and Ram-Lak ramp filtering. Standard reconstruction was performed using either 1 complete rotation (1600 sequentially acquired projections), or 140 rotations (224,000 sequentially acquired projections). FSCT reconstruction was performed by phase-binning the projection data according to the 9.924 Hz phantom cycle, using a range of N_{rot} between 1 and 140 rotations, and a range of N_{bin} between 1 and 100 motion phase bins.¹ FSCT reconstruction error was computed as the mean and standard deviation of voxel-wise absolute intensity difference between the reconstructed image and the phantom image across all reconstructed phase bins. The reference phantom image for each phase bin was selected at the motion phase corresponding to the midpoint of the phase bin.

E. Thoracic Imaging in vivo

One pig weighing 45 kg was scanned with approval from the University of Iowa Institutional Animal Care and Use Committee (Protocol number 5031314). The animal was sedated using an intravenous infusion of propofol at $9 \text{ mg kg}^{-1} \text{ hr}^{-1}$, and paralyzed with intermittent doses of rocuronium at 1 mg kg^{-1} . EKG waveforms were obtained using a Philips patient monitor equipped with the M3001A measurement module (Philips Healthcare, Andover, MA). The animal was ventilated by a FabianHFO ventilator/oscillator (Acutronic Medical Systems AG, Hirzel, Switzerland) using pressure-controlled ventilation at a rate of 24 min^{-1} with $5 \text{ cmH}_2\text{O}$ positive end-expiratory pressure, $20 \text{ cmH}_2\text{O}$ peak inspiratory pressure, and I:E ratio 1:2. The animal was positioned in the gantry of a SOMATOM Force CT scanner (Siemens Healthineers, Forchheim, Germany) such that the axial field of view was centered approximately 3 cm caudal to the carina. Scanning was performed during 1) ventilation with pressure-controlled conventional mechanical ventilation (CMV); 2) high-frequency oscillatory ventilation (HFOV) set at 5 Hz; 3) HFOV set at 20 Hz; and 4) multi-frequency oscillatory ventilation (MFOV) using a broadband excitation waveform containing energy set at 5 Hz, 10 Hz, 15 Hz, and 20 Hz [5]. Each of the oscillatory waveforms was delivered at $10 \text{ cmH}_2\text{O}$

¹A sample MATLAB script for this computational phantom simulation is available from the authors upon request.

mean airway pressure, $100 \text{ cmH}_2\text{O}$ peak-to-peak pressure, and 10 L min^{-1} bias flow. The animal was continuously scanned at 80 kVp tube voltage and 150 mA tube current for a total duration of approximately 30 seconds, at a 4.0 Hz scanner rotation frequency (250 ms period). The Force scanner acquired 1120 projections per rotation using 920 detectors per row and 96 detector rows. Transverse beam width was 0.48 mm at the isocenter, with 0.6 mm spacing between detector rows. As part of another study under this protocol, a total of 177 mL Isovue-370 contrast agent (Bracco Diagnostic Inc., Monroe Township, NJ) was given over approximately one hour. Scanning for this study was performed 20 minutes following the final 54 mL dose.

The ventilatory and cardiac frequencies were estimated from the ventilator settings and EKG heart rate monitor, however these estimates lacked sufficient precision for the FSCT reconstruction technique. Since the *in vivo* projection data contained substantial frequency content at both ventilatory and cardiac frequencies, temporal variations in each set of projection data were examined to determine frequency content prior to selection of FSCT reconstruction frequencies. The acquired projections were re-sampled at intervals of 2π radians in projection angle, producing subsets of the projection data containing transient variations in subject position sampled at the frequency of the scanner rotation (f_{rot}). In the two-dimensional discrete Fourier transform (2D-DFT) of this subset of projection data, the dimensions of the transformed projection data correspond to detector position and time. Integrating the magnitude of the 2D-DFT along the dimension corresponding to detector position produced a spectrum of oscillatory energy in the projection data as a function of temporal frequency, relative to scanner rotation frequency (i.e., frequencies greater than $0.5f_{\text{rot}}$ will be aliased). Spectral peaks identified in the oscillatory energy spectrum correspond to either ventilatory or cardiogenic sources of motion. Thus ventilatory and cardiac frequencies were determined from the projection data, using *a priori* knowledge obtained from physiologic monitors (e.g., ventilator settings, EKG-derived heart rate) to determine de-aliased frequency content.

FSCT reconstruction was performed by first phase-binning the projection data according to either ventilatory or cardiac cycle as described in the Theory section, and subsequently reconstructing each phase-binned sinogram using a Feldkamp-type cone-beam reconstruction algorithm [28] (Michigan Image Reconstruction Toolbox, J. A. Fessler, University of Michigan, Ann Arbor, MI) and MATLAB (The Mathworks Inc., Natick, MA).

III. RESULTS

Fig. 4 shows the simulated phantom at time $t = 0$ seconds, alongside standard CT reconstructions and FSCT reconstruction of projection data acquired over 140 scanner rotations. The FSCT image is only shown at the first of 10 motion phase bins. A transient profile is shown through a single row from the phantom and FSCT images, resolving the periodic motion of the phantom over multiple 9.924 Hz oscillation cycles. A static profile through the same row is provided for the

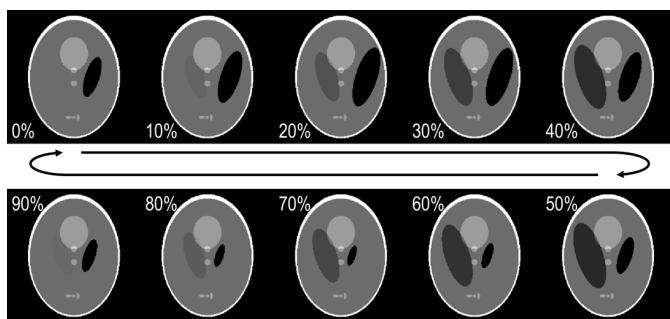


Fig. 3. Simulated phantom shown at 10 discrete phases equally spaced throughout a continuous and periodic deformation cycle. Two ellipses of the standard Shepp-Logan phantom [27] were modified with sinusoidal oscillations in size, intensity, and/or centroid position. Image size was 256 x 256 pixels.

standard reconstructed images. The standard reconstructions are affected by motion artifacts that obscure finer details in lung structure, whereas the FSCT reconstruction yields crisp spatial boundaries within each bin and smooth transient motion between bins.

Fig. 5 shows the error of FSCT reconstruction performed using varying subsets of the total acquired projection data and varying phase bin sizes. Error was assessed by the mean and standard deviation of voxel-wise intensity difference between each reconstructed image compared to the reference phantom images. The lower bound for adequate scanning duration given by (17) is indicated by the dashed line, delineating two domains with different behavior of the reconstruction error with respect to the amount of sampling and number of bins. The minimum sampling criterion is not satisfied at short scanning durations and large number of bins, thus aliasing and streak artifact caused by undersampling produce substantial reconstruction errors. The minimum sampling criterion is satisfied at long scanning durations and small number of bins, with mean voxel-wise intensity difference converging with increased sampling. However when N_{bin} becomes too small, the reconstruction error increases as a result of the increased bin size and motion artifact. For reference, the standard reconstruction using 1 rotation, shown in Fig. 4e, corresponds to the location $N_{\text{bin}} = 1$ and $N_{\text{rot}} = 1$ in the bottom-left corner of Figs. 5a and 5b. Likewise, the standard reconstruction using 140 rotations, shown in Fig. 4g, corresponds to the location $N_{\text{bin}} = 1$ and $N_{\text{rot}} = 140$ in the top-left corner of Figs. 5a and 5b.

A. Thoracic Imaging *in vivo*

Fig. 6 shows frequency content in the projection data acquired during *in vivo* mechanical ventilation. The spectral peaks correspond to either cardiogenic or ventilatory oscillations, potentially aliased relative to the scanner rotation frequency. FSCT reconstruction frequencies were chosen for each set of projection data based on the spectral peaks, using *a priori* knowledge to de-alias higher frequency content. Fig. 7 shows example images reconstructed at both cardiac and ventilatory frequencies using the FSCT approach. Transient profiles from each image are presented through a single slice from the transverse plane, resolving the motions of various intrathoracic organs and tissues across subject phase

bins, equally spaced throughout the periodic motion cycle.² Motion artifact is present in each image wherever extraneous motion occurs at non-harmonic frequencies relative to the reconstruction frequency—for example, cardiogenic motion produces blurring in images reconstructed at the ventilatory frequency, and *vice versa*.

It should be emphasized that each pair of ventilatory and cardiac reconstructions presented in Fig. 7 were obtained from the same projection data. Furthermore the transient profiles are shown through the same spatially-oriented slice. Therefore, any differences in image quality or structural clarity between these paired reconstructions are a direct consequence of modulating the reconstruction frequency and/or number of phase bins.

IV. DISCUSSION

In this study, we have presented an algorithm for reconstructing temporally-resolved CT images of periodic subject motion. This frequency-selective 4D-CT (FSCT) imaging technique involves continuously acquiring X-ray projections during multiple rotations of the source around the oscillating subject, then sorting the acquired projections into multiple subject phase bins, each yielding a complete sinogram for reconstruction of an image sequence.

Respiratory-gated and non-gated 4D-CT are suitable for use during irregular, spontaneous breathing with low subject motion frequency compared to scanner rotation frequency [10], [29]. FSCT extends 4D-CT imaging across a much wider range of application in terms of subject motion frequencies, yet imposes a restricting assumption of regular, periodic motion. Nevertheless, the limitations imposed by the feasible sampling criterion (16) do not restrict practical 4D-CT reconstruction at low frequencies such as spontaneous breathing. This is indicated in Fig. 2 by the available selection of N_{bin} up to 20 for low f_{sub} relative to f_{rot} . However at high frequencies of subject motion, the choice of N_{bin} may be infeasible depending on (16).

Traditional retrospective gating for cardiac CT can be performed by continuously acquiring both EKG and X-ray projections as the subject slowly translates through the scanner [30]. The projection data is then selectively filtered prior to reconstruction, retaining projections corresponding to the diastolic phase and discarding the rest. Despite the potential for high radiation exposure during the scan, a large portion of the projection data may actually not be used for the image reconstruction. Alternatively with prospective triggering, EKG detection of diastole initiates the scanner to emit and detect X-ray beams through a subset of projection angles, typically covering 180° plus half the angle of the detector array [31]. The subject is then translated to scan a different transverse plane upon the next diastolic triggering event. This type of acquisition is informally known as “step-and-shoot” in regard to the repeated process of “stepping” to the next transverse plane followed by “shooting” the X-ray beam for acquisition. Compared to retrospective gating, prospective triggering

²Animations of subject motion are provided as supplementary materials, available online in the supporting documents / multimedia tab.

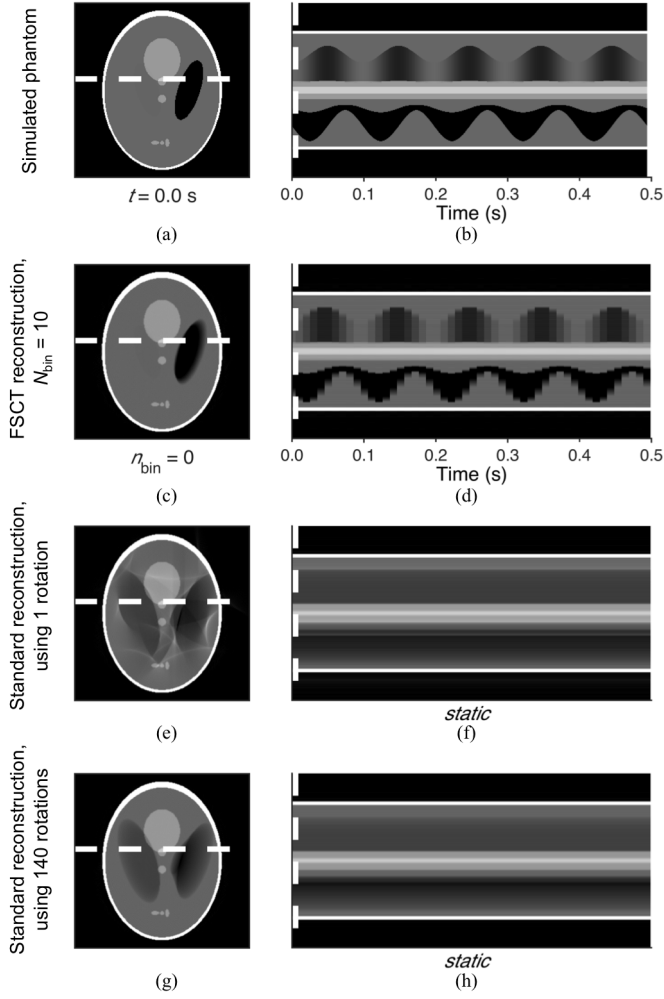


Fig. 4. Comparison between standard CT reconstruction (e,g) and FSCT reconstruction (c) of the simulated phantom oscillating at 9.924 Hz (a). A transient profile shown through a single row (white dashed line) is provided for the simulated phantom (b) and FSCT reconstructed image (d), resolving periodic motion over multiple 9.924 Hz oscillation cycles. A static profile through the same row is provided for the standard reconstructed images (f,h).

reduces the amount of ionizing radiation required for cardiac imaging. For either of these EKG-based methods, the temporal resolution of the image is determined by the duration of acquisition within each cardiac cycle [32]. In other words, temporal resolution depends on how much cardiac motion is averaged in the reconstruction: faster scanner rotation reduces the duration of acquisition within each cardiac cycle, and thus results in less motion artifact.

Multi-segment reconstruction is another effective strategy for improving the temporal resolution of a thoracic image. This approach involves reducing the duration of image acquisition each cardiac cycle by acquiring a subset of projection data (i.e., 180° plus half of the detector fan angle) over multiple cardiac cycles [33]. Multi-segment reconstruction results in a more consistent state of the mediastinum during each acquisition compared to standard EKG-triggering approaches. However the extended scanning protocol increases susceptibility to image corruption from other extraneous motions such as respiration [34]–[36]. Several other techniques have been developed

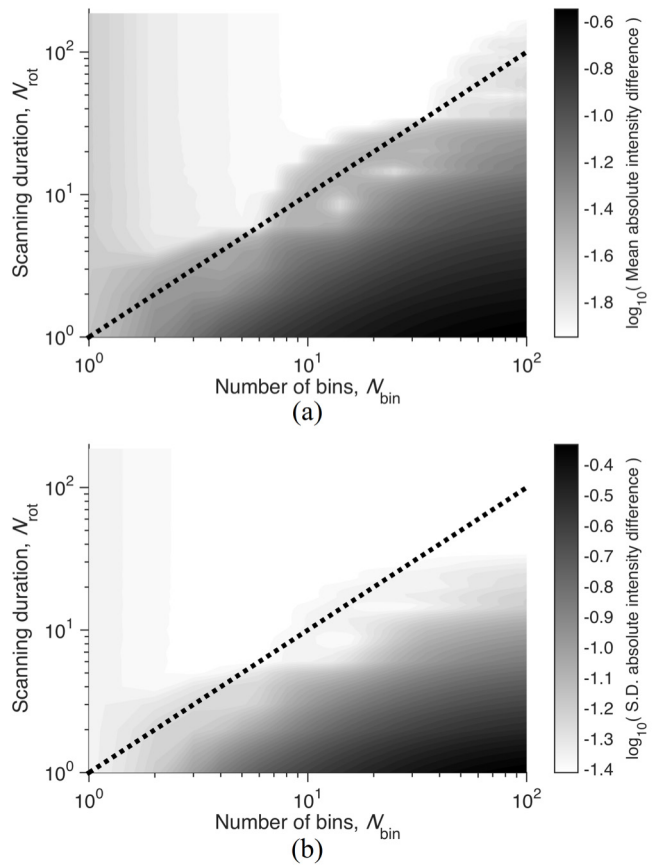


Fig. 5. Contours of error in FSCT reconstructed image of simulated phantom for varying selection of scanning duration N_{rot} and number of bins N_{bin} . Error was assessed by (a) mean and (b) standard deviation of voxel-wise absolute intensity difference between the reconstructed image and the phantom image across all reconstructed phase bins. The lower bound for adequate sampling given by (17), is indicated by the dashed line, using $N_{det} = 1000$, $N_{pro} = 1600$, $f_{rot} = 3.509$ Hz, $f_{sub} = 9.924$ Hz.

for mitigating motion artifact and radiation exposure in cardiac imaging, such as compensation algorithms that modify the projection data to approximate a motionless image of the thorax based on estimated motion models [37]–[41].

Alternative strategies for volumetric imaging during dynamic motion using X-ray CT, such as quasi-static [42] or temporally-averaged [4], [43] approaches, tolerate some amount of either temporal or spatial blurring when using sequential projection acquisition. FSCT fully resolves the spatio-temporal dynamics of subject motion, yet only throughout the cycle of one specified reconstruction frequency. Thus, FSCT images represent a periodic, dynamic steady state of the subject. Imaging high-frequency motions (i.e., greater than the scanner rotation frequency) is an important potential application of the FSCT technique, opening a relatively unexplored area of research in CT imaging. Reconstruction algorithms incorporating direct sinogram alterations introduce some uncertainty in the resulting image due to the use of numerically estimated motion models used to approximate the actual subject motion [37]–[41]. Motion estimation approaches maintain reasonably low exposure to ionizing radiation. Our FSCT technique is intended to provide high-fidelity images of the

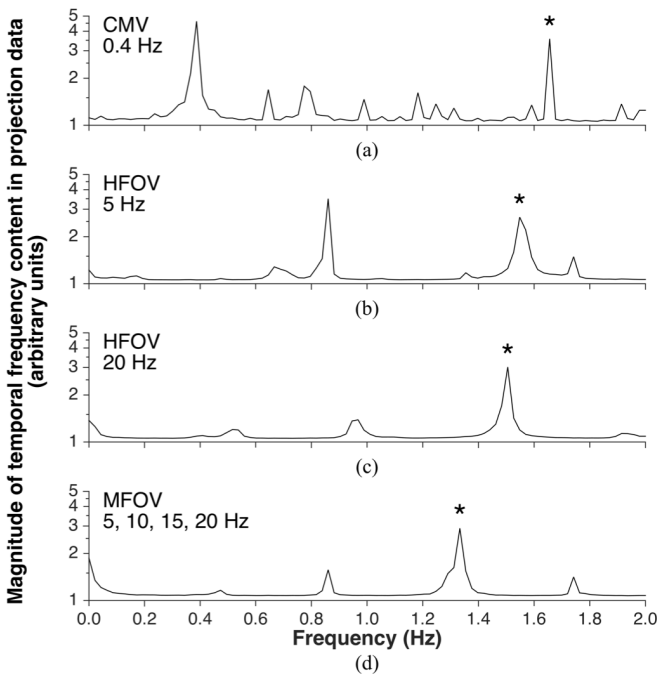


Fig. 6. Frequency content in the projection data acquired during in vivo mechanical ventilation of a pig, using either conventional mechanical ventilation (a), high-frequency oscillatory ventilation (b,c), or multi-frequency oscillatory ventilation (d). Frequency on the horizontal axis obtained from discrete Fourier transform using the scanner rotation frequency $f_{\text{rot}} = 4 \text{ Hz}$ as the sampling frequency. Thus subject motion frequencies greater than $0.5f_{\text{rot}}$ are aliased. Spectral peaks correspond to either ventilatory motion or cardiogenic motion. Spectral peaks corresponding to heart rate are indicated by asterisks.

subject *during* actual periodic motion, albeit at the expense of increased radiation exposure. Thus at present FSCT may be more suitable for research purposes, rather than clinical diagnostic use.

The selection requirements for FSCT imaging parameters were characterized for a given subject motion frequency f_{sub} and desired number of images N_{bin} , yielding a feasible sampling condition (16) as well as an optimal sampling condition (18). The use of a circular X-ray source trajectory allows improved temporal resolution compared to similar phase-correlated reconstruction of projections acquired during a spiral or helical trajectory [24], [25]. FSCT imaging is feasible for periodic subject motions at nearly any frequency provided an appropriate frequency ratio ($f_{\text{sub}}/f_{\text{rot}}$) is used to ensure full sampling without repetition (Fig. 2). Thus FSCT can be used to obtain temporally-resolved image sequences of both high- and low-frequency anatomic motion. Fig. 7 demonstrates several successful reconstructions using FSCT across a wide range of frequencies (0.4 Hz to 20 Hz) relative to the scanner rotation frequency (4 Hz). Ideally, scanner parameters such as f_{rot} could be tuned to minimize feasible scanning duration given a specific subject motion frequency f_{sub} . In practical applications, most commercially available CT scanners offer a small number of choices for f_{rot} and N_{pro} preset by the manufacturer. However unlike conventional CT imaging, the temporal resolution for FSCT is determined not only by the rotation speed of the scanner, but also by a combination of imaging and reconstruction parameters.

Other potential uses of FSCT span a variety of physiologic applications involving periodic motion, including analysis of airway, lung tissue, or blood vessel deformation, tumor localization and tracking, cardiac wall motion abnormalities, as well as joint motion. Future work may also involve four-dimensional image registration to quantify regional strains of thoracic structure during periodic motion [42], [44]. Four-dimensional registration approaches identify smooth transformations between volumetric images through a temporal dimension (or in this case specifically, subject motion phase) [45], [46]. A periodic constraint may be applied to FSCT-registration, ensuring continuity and smoothness of the computed transformation throughout the entire reconstructed sequence, including the wrap-around from the final image to the initial image.

A. Limitations

Some limitations of our technique should be noted. First, the extensive scanning duration required for FSCT reconstruction exposes the subject to prohibitive radiation dosage, i.e., up to two orders-of-magnitude greater than standard X-ray CT imaging. Accordingly, clinical implementation of FSCT imaging in patients may not be warranted without substantial reductions in radiation exposure. Exact control of scanner rotation frequency f_{rot} according to (18) may allow minimization of redundant projection acquisition and thus minimization of scanning duration. Iterative reconstruction of each phase-binned sinogram may allow dose reductions at the expense of increased computational cost [47]. It may be possible to reduce radiation dose further by minimizing the number of acquired projection angles per subject phase bin using half-scan approaches for cone-beam reconstruction [48], [49]. Reductions in scanning duration may be achievable using specialized dual-source CT scanners equipped with two independent X-ray sources and corresponding detector arrays positioned at different projection angles through the subject [50], [51]. Finally, prospective triggering approaches generally reduce radiation exposure compared to retrospective gating approaches [52], [53]. Prospective FSCT imaging may also be possible by synchronizing X-ray beam actuation to specified phases of a particular periodic subject motion cycle, with frequency known *a priori*. In this way, prospective triggering could reduce the total radiation dose by selectively avoiding radiation exposure during non-reconstructed phases.

Although the FSCT technique was evaluated quantitatively in computational simulations, evaluation of the experimentally obtained images presented in Fig. 7 was qualitative. Quantitative assessment of anatomic structures in FSCT images, such as segmented volumes of intrathoracic structures, may require “step-and-shoot” implementation.

Finally, the FSCT technique proposed herein uses only one value of f_{sub} per image sequence. It is possible to reconstruct multiple image sequences from the same raw projection data, simply by using a different value of f_{sub} for each sequence. Fig. 7 shows several cases in which two image sequences were reconstructed: one at the ventilatory frequency and another at the cardiac frequency. However the resulting images will contain resolved motion at only the one specific reconstruction

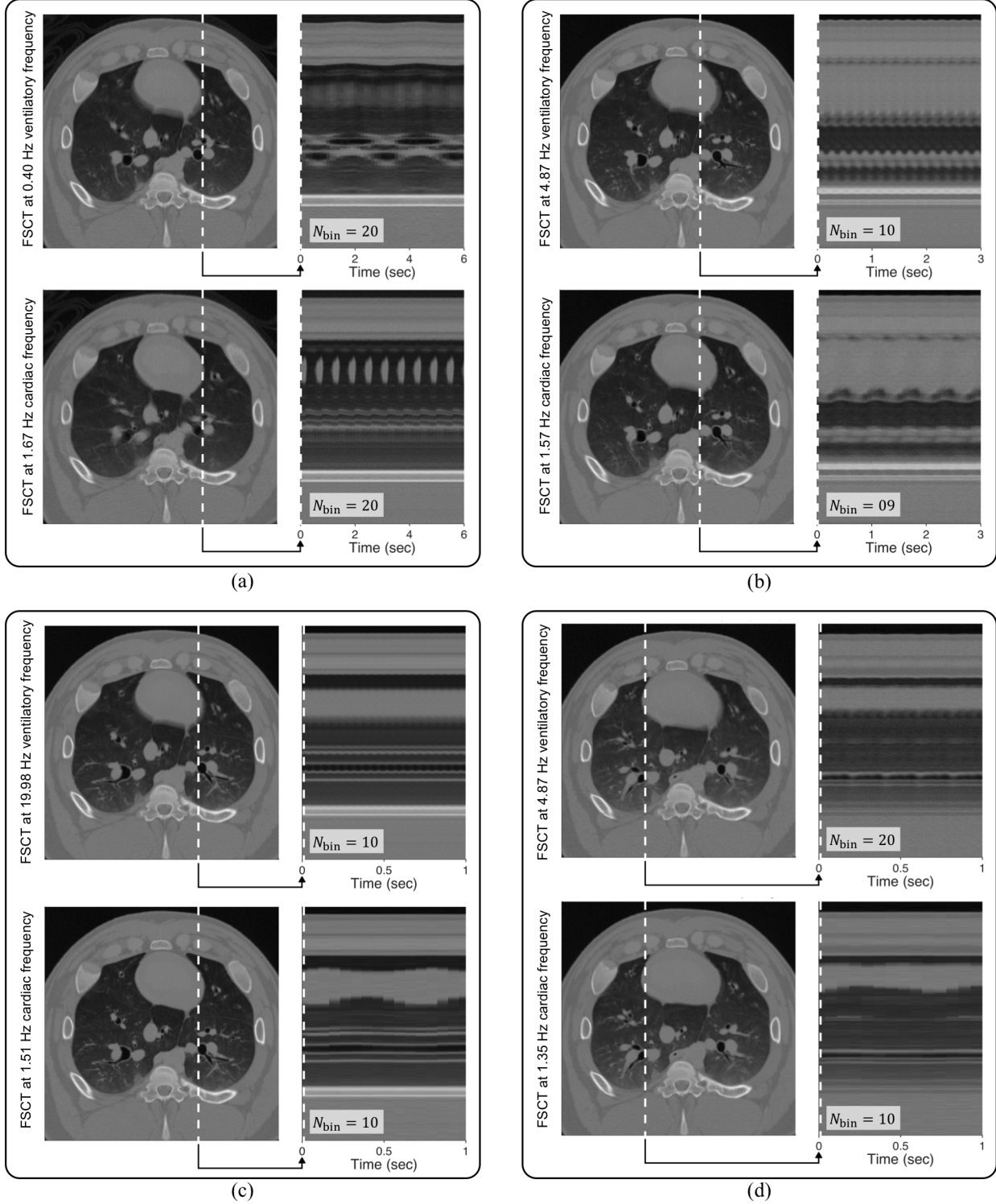


Fig. 7. Example images reconstructed from projection data acquired over 30 seconds of scanning during *in vivo* mechanical ventilation of a pig, using (a) conventional mechanical ventilation at 0.4 Hz (24 min^{-1}), (b) high-frequency oscillatory ventilation at 5 Hz (300 min^{-1}), (c) high-frequency oscillatory ventilation at 20 Hz (1200 min^{-1}), and (d) multi-frequency oscillatory ventilation using a broadband waveform containing energy at 5, 10, 15, and 20 Hz. Both ventilatory and cardiac frequencies were reconstructed from the same projection data. Transient profiles from each image are presented through a single slice from the transverse plane over 1 to 6 seconds, showing resolved motion across subject phase bins equally spaced throughout the periodic motion cycles.

frequency, as well as any harmonics or integer multiples of the reconstruction frequency. All other extraneous motion in the subject will cause motion artifact and blurring. For this reason, blurring around the heart is apparent in images

reconstructed at the ventilatory frequency, whereas blurring in the lungs is apparent in images reconstructed at the cardiac frequency. It may be possible to combine information from both reconstructed images to reduce apparent motion artifact [54].

Additionally, FSCT may not be appropriate for temporally resolving physiologic processes that are either irregular, aperiodic, or otherwise occur on multiple time scales, such as diffusive equilibration during angiography or tracer gas washout.

V. CONCLUSION

Frequency-selective CT imaging produces a temporally-resolved volumetric image sequence of periodic subject motion at a specified reconstruction frequency. This novel technique enables imaging of both low- and high-frequency dynamic periodic motion at a specified frequency, with minimal extraneous motion artifact. The FSCT approach may offer improved imaging fidelity of dynamic subject motion compared to more conventional ‘quasi-static’ approaches. When combined with registration techniques [45], FSCT may provide detailed four-dimensional information of distributed tissue deformation previously inaccessible using standard reconstruction approaches.

ACKNOWLEDGMENT

The authors would like to thank M. K. Fuld and Siemens Healthineers (Forchheim, Germany) for technical assistance. J. Herrmann and D. W. Kaczka are shareholders in Oscillavent, Inc., Iowa City, IA 52240 and E.A. Hoffman is a shareholder in Vida Diagnostics, Inc., Coralville, IA 52241.

REFERENCES

- [1] G. Li *et al.*, “Advances in 4D medical imaging and 4D radiation therapy,” *Technol. Cancer Res. Treat.*, vol. 7, no. 1, pp. 67–81, 2008.
- [2] P. Keall, “4-dimensional computed tomography imaging and treatment planning,” *Seminars Radiat. Oncol.*, vol. 14, no. 1, pp. 81–90, 2004.
- [3] N. J. Pelc, “Recent and future directions in CT imaging,” *Ann. Biomed. Eng.*, vol. 42, no. 2, pp. 260–268, 2014.
- [4] R. B. Easley *et al.*, “Total and regional lung volume changes during high-frequency oscillatory ventilation (HFOV) of the normal lung,” *Respirat. Physiol. Neurobiol.*, vol. 165, no. 1, pp. 54–60, 2009.
- [5] D. W. Kaczka *et al.*, “Multifrequency oscillatory ventilation in the premature lung: Effects on gas exchange, mechanics, and ventilation distribution,” *Anesthesiology*, vol. 123, no. 6, pp. 1394–1403, 2015.
- [6] J. L. M. Kroft, J. J. H. Roelofs, and J. Geleijns, “Scan time and patient dose for thoracic imaging in neonates and small children using axial volumetric 320-detector row CT compared to helical 64-, 32-, and 16-detector row CT acquisitions,” *Pediatric Radiol.*, vol. 40, no. 3, pp. 294–300, 2010.
- [7] J. D. Newell, Jr., *et al.*, “Very low-dose (0.15 mGy) chest CT protocols using the COPDGene 2 test object and a third-generation dual-source CT scanner with corresponding third-generation iterative reconstruction software,” *Invest. Radiol.*, vol. 50, no. 1, pp. 40–45, 2015.
- [8] L. W. Goldman, “Principles of CT and CT technology,” *J. Nucl. Med. Technol.*, vol. 35, no. 3, pp. 115–128, 2007.
- [9] G. Zeng, *Medical Image Reconstruction*, 1st ed. Berlin, Germany: Springer, 2010, pp. 87–174.
- [10] S. S. Vedam, P. J. Keall, V. R. Kini, H. Mostafavi, H. P. Shukla, and R. Mohan, “Acquiring a four-dimensional computed tomography dataset using an external respiratory signal,” *Phys. Med. Biol.*, vol. 48, no. 1, pp. 45–62, 2003.
- [11] J. F. Barrett and N. Keat, “Artifacts in CT: Recognition and avoidance,” *Radiographics*, vol. 24, no. 6, pp. 1679–1691, 2004.
- [12] S. Halliburton *et al.*, “State-of-the-art in CT hardware and scan modes for cardiovascular CT,” *J. Cardiovascular Comput. Tomogr.*, vol. 6, no. 3, pp. 154–163, 2012.
- [13] N. L. Ford, A. R. Wheatley, D. W. Holdsworth, and M. Drangova, “Optimization of a retrospective technique for respiratory-gated high speed micro-CT of free-breathing rodents,” *Phys. Med. Biol.*, vol. 52, no. 19, pp. 5749–5769, 2007.
- [14] D. Ertel, Y. Kyriakou, R. M. Lapp, and W. A. Kalender, “Respiratory phase-correlated micro-CT imaging of free-breathing rodents,” *Phys. Med. Biol.*, vol. 54, no. 12, pp. 3837–3846, 2009.
- [15] J.-J. Sonke, L. Zijp, P. Remeijer, and M. van Herk, “Respiratory correlated cone beam CT,” *Med. Phys.*, vol. 32, no. 4, pp. 1176–1186, 2005.
- [16] L. Husmann *et al.*, “Oronary artery motion and cardiac phases: Dependency on heart rate—Implications for CT image reconstruction,” *Radiology*, vol. 245, no. 2, pp. 567–576, 2007.
- [17] D. Ertel, T. Pflederer, S. Achenbach, and W. A. Kalender, “Real-time determination of the optimal reconstruction phase to control ECG pulsing in spiral cardiac CT,” *Phys. Med.*, vol. 25, no. 3, pp. 122–127, 2009.
- [18] M. Kachelrieß, D.-A. Sennst, W. Maxmoser, and W. A. Kalender, “Kymogram detection and kymogram-correlated image reconstruction from subsecond spiral computed tomography scans of the heart,” *Med. Phys.*, vol. 29, no. 7, pp. 1489–1503, 2002.
- [19] J. J. Pillow, “High-frequency oscillatory ventilation: Mechanisms of gas exchange and lung mechanics,” *Critical Care Med.*, vol. 33, no. 3, pp. S135–S141, 2005.
- [20] J. Thurgood *et al.*, “Functional lung imaging during HFV in preterm rabbits,” *PLoS One*, vol. 7, no. 10, p. e48122, 2012.
- [21] T. Luecke, P. Herrmann, P. Kraincuk, and P. Pelosi, “Computed tomography scan assessment of lung volume and recruitment during high-frequency oscillatory ventilation,” *Critical Care Med.*, vol. 33, no. 3, pp. S155–S162, 2005.
- [22] P. Kraincuk, G. Körmöcz, M. Prokop, G. Ihra, and A. Aloy, “Alveolar recruitment of atelectasis under combined high-frequency jet ventilation: A computed tomography study,” *Intensive Care Med.*, vol. 29, no. 8, pp. 1265–1272, 2003.
- [23] D. G. Mulreany, B. A. Simon, K. J. Murphy, and R. B. Easley, “Volumetric xenon-CT imaging of conventional and high-frequency oscillatory ventilation,” *Acad. Radiol.*, vol. 16, no. 6, pp. 718–725, 2009.
- [24] M. Kachelrieß and W. A. Kalender, “Electrocardiogram-correlated image reconstruction from subsecond spiral computed tomography scans of the heart,” *Med. Phys.*, vol. 25, no. 12, pp. 2417–2431, 1998.
- [25] M. Kachelrieß, S. Ulzheimer, and W. A. Kalender, “ECG-correlated image reconstruction from subsecond multi-slice spiral CT scans of the heart,” *Med. Phys.*, vol. 27, no. 8, pp. 1881–1902, 2000.
- [26] L. Lorentzen and H. Waadeland, *Continued Fractions*, vol. 1, 1st ed. Paris, France: Atlantis Press, 2008, pp. 1–24.
- [27] L. A. Shepp and B. F. Logan, “The Fourier reconstruction of a head section,” *IEEE Trans. Nucl. Sci.*, vol. 21, no. 3, pp. 21–43, Jun. 1974.
- [28] L. A. Feldkamp, L. C. Davis, and J. W. Kress, “Practical cone-beam algorithm,” *J. Opt. Soc. Amer. A, Opt. Image Sci.*, vol. 1, no. 6, pp. 612–619, 1984.
- [29] Y. Cheung, J. Hinkle, S. Joshi, and A. Sawant, “SU-E-J-170: Beyond single-cycle 4DCT: Maximum a posteriori (MAP) reconstruction-based Binning-free multicycle 4DCT for lung radiotherapy,” *Med. Phys.*, vol. 41, no. 6, pp. 195–196, 2014.
- [30] B. Desjardins and E. A. Kazerooni, “ECG-gated cardiac CT,” *Amer. J. Roentgenol.*, vol. 182, no. 4, pp. 993–1010, 2004.
- [31] J. P. Earls, “How to use a prospective gated technique for cardiac CT,” *J. Cardiovascular Comput. Tomogr.*, vol. 3, no. 1, pp. 45–51, 2009.
- [32] M. Mahesh and D. D. Cody, “Physics of cardiac imaging with multiple-row detector CT,” *Radiographics*, vol. 27, no. 5, pp. 1495–1509, 2007.
- [33] T. G. Flohr, R. Raupach, and H. Bruder, “Cardiac CT: How much can temporal resolution, spatial resolution, and volume coverage be improved?” *J. Cardiovascular Comput. Tomogr.*, vol. 3, no. 3, pp. 143–152, 2009.
- [34] C. Herzog *et al.*, “Does two-segment image reconstruction at 64-section CT coronary angiography improve image quality and diagnostic accuracy?” *Radiology*, vol. 244, no. 1, pp. 121–129, 2007.
- [35] D. Schnapauff, F. Teige, B. Hamm, and M. Dewey, “Comparison between the image quality of multisegment and halfscan reconstructions of non-invasive CT coronary angiography,” *Brit. J. Radiol.*, vol. 82, no. 984, pp. 969–975, 2009.
- [36] T. G. Flohr and B. Ohnesorge, “Heart rate adaptive optimization of spatial and temporal resolution for electrocardiogram-gated multislice spiral CT of the heart,” *J. Comput. Assist. Tomogr.*, vol. 25, no. 6, pp. 907–923, 2001.
- [37] A. A. Isola, A. Ziegler, T. Koehler, W. J. Niessen, and M. Grass, “Motion-compensated iterative cone-beam CT image reconstruction with adapted blobs as basis functions,” *Phys. Med. Biol.*, vol. 53, no. 23, pp. 6777–6797, 2008.
- [38] Q. Tang, J. Cammin, S. Srivastava, and K. Taguchi, “A fully four-dimensional, iterative motion estimation and compensation method for cardiac CT,” *Med. Phys.*, vol. 39, no. 7, pp. 4291–4305, 2012.

[39] J. H. Cho and J. A. Fessler, "Motion-compensated image reconstruction for cardiac CT with sinogram-based motion estimation," in *Proc. IEEE Nucl. Sci. Symp. Med. Imag. Conf.*, Seoul, South Korea, Nov. 2013, pp. 1–5.

[40] C. Rohkohl, H. Bruder, K. Stierstorfer, and T. G. Flohr, "Improving best-phase image quality in cardiac CT by motion correction with MAM optimization," *Med. Phys.*, vol. 40, no. 3, p. 31901, 2013.

[41] S. Kim, Y. Chang, and J. B. Ra, "Cardiac motion correction based on partial angle reconstructed images in X-ray CT," *Med. Phys.*, vol. 42, no. 5, pp. 2560–2571, 2015.

[42] D. W. Kaczka, K. Cao, G. E. Christensen, J. H. T. Bates, and B. A. Simon, "Analysis of regional mechanics in canine lung injury using forced oscillations and 3D image registration," *Ann. Biomed. Eng.*, vol. 39, no. 3, pp. 1112–1124, 2011.

[43] G. E. Christensen, J. H. Song, W. Lu, I. El Naqa, and D. A. Low, "Tracking lung tissue motion and expansion/compression with inverse consistent image registration and spirometry," *Med. Phys.*, vol. 34, no. 6, pp. 2155–2163, 2007.

[44] Y. Yin, E. A. Hoffman, and C.-L. Lin, "Mass preserving nonrigid registration of CT lung images using cubic B-spline," *Med. Phys.*, vol. 36, no. 9, pp. 4213–4222, 2009.

[45] B. Zhao *et al.*, "Tissue-volume preserving deformable image registration for 4DCT pulmonary images," in *Proc. IEEE Conf. Comput. Vis. Pattern Recognit. Workshops*, Las Vegas, NV, USA, Jul. 2016, pp. 41–49.

[46] H. Sundar, H. Litt, and D. Shen, "Estimating myocardial motion by 4D image warping," *Pattern Recognit.*, vol. 42, no. 11, pp. 2514–2526, 2009.

[47] B. De Man and J. A. Fessler, "Statistical iterative reconstruction for X-ray computed tomography," in *Biomedical Mathematics: Promising Directions in Imaging, Therapy Planning, and Inverse Problems*, 1st ed. Madison, WI, USA: Medical Physics Publishing, 2010, pp. 113–140.

[48] A. N. Primak, C. H. McCollough, M. R. Bruesewitz, J. Zhang, and J. G. Fletcher, "Relationship between noise, dose, and pitch in cardiac multi-detector row CT," *Radiographics*, vol. 26, no. 6, pp. 1785–1794, 2006.

[49] S. W. Lee and G. Wang, "A grangeat-type half-scan algorithm for cone-beam CT," *Med. Phys.*, vol. 30, no. 4, pp. 689–700, 2003.

[50] M. Petersilka, H. Bruder, B. Krauss, K. Stierstorfer, and T. G. Flohr, "Technical principles of dual source CT," *Eur. J. Radiol.*, vol. 68, no. 3, pp. 362–368, 2008.

[51] D. Ertel, E. Kröber, Y. Kryiakou, O. Langner, and W. A. Kalender, "Modulation transfer function-based assessment of temporal resolution: Validation for single- and dual-source CT," *Radiology*, vol. 248, no. 3, pp. 1013–1017, 2008.

[52] T.-Y. Lee and R. K. Chhem, "Impact of new technologies on dose reduction in CT," *Eur. J. Radiol.*, vol. 76, no. 1, pp. 28–35, 2010.

[53] W. P. Shuman *et al.*, "Prospective versus retrospective ECG gating for 64-detector CT of the coronary arteries: Comparison of image quality and patient radiation dose," *Radiology*, vol. 248, no. 2, pp. 431–437, 2008.

[54] R. M. Lapp, M. Kachelreß, D. Ertel, Y. Kryiakou, and W. A. Kalender, "Cardiac phase-correlated image reconstruction and advanced image processing in pulmonary CT imaging," *Eur. Radiol.*, vol. 19, no. 4, pp. 1035–1042, 2009.

Minimizing Parenchymal Strain Heterogeneity During Oscillatory Ventilation

Abstract Number:

2063

Abstract Type:

AUA Abstract Submission

Authors:

David Kaczka¹, Jacob Herrmann¹

Institutions:

¹University of Iowa, Iowa City, IA

Presenting Author:

Dr. David Kaczka, MD PhD

Introduction:

Gas flow in the lung during oscillatory ventilation is distributed in a heterogeneous and frequency-dependent manner [1]. However severe ventilation heterogeneity may contribute to impairments in gas exchange, ventilation-to-perfusion mismatch, and ventilator-induced lung injury (VILI). Minimizing acinar strain heterogeneity may reduce the risk of VILI while producing efficient carbon dioxide elimination. In this study we used a gas transport model to optimize oscillatory ventilator waveforms, in which the spectral content of each flow waveform was adjusted to minimize parenchymal strain heterogeneity during eucapnic ventilation [2,3].

Methods:

A heterogeneous canine lung model consisting of N terminal viscoelastic acini was ventilated with a simulated oscillatory flow waveform composed of M simultaneous frequencies. The relative magnitudes of flow at each frequency was numerically optimized according to a cost function Φ , defined as the coefficient of variation of acinar volumetric distension. Using a Monte Carlo technique, we estimated the optimal oscillatory waveform that produced the lowest Φ , and thus the lowest degree of parenchymal strain heterogeneity. The relative magnitudes of each oscillatory component was adjusted to achieve eucapnia.

Results:

Optimal oscillatory waveforms were characterized by flows with large amplitudes at low frequencies, combined with small amplitude flows at high frequencies. Average acinar strain during eucapnic ventilation was reduced when additional higher frequency components were included in the waveform.

Conclusion:

Superposition of multiple simultaneous oscillatory frequencies provides more uniform ventilation distribution compared to single frequency oscillatory ventilation, as well as more mechanically efficient gas exchange to achieve eucapnia. An optimal combination of frequencies, amplitudes, and phases in an oscillatory ventilator waveform may be determined according to the distribution of flows throughout the heterogeneous lung periphery. Work supported by DOD grant PR151761.

Optimization of Spectral Content in Oscillatory Ventilator Waveforms

Jacob Herrmann¹, David W. Kaczka¹

¹University of Iowa, Iowa City, IA

Introduction: Oscillatory flows, when used in a lung protective ventilation strategy, are distributed throughout the respiratory system in a heterogeneous and frequency-dependent manner [1]. Ventilation heterogeneity contributes to impairments in gas exchange and ventilator-induced lung injury (VILI), due to regional overdistention and atelectrauma. Thus minimizing acinar strain heterogeneity may also minimize the risk of VILI. In this study, we developed an optimization algorithm for tuning the spectral content of oscillatory ventilator waveforms, in order to minimize acinar strain heterogeneity in computational model. Emphasis was placed on the development of oscillatory waveforms comprised of multiple simultaneous frequencies, which may be ‘tuned’ to local mechanical properties [2].

Materials & Methods:

For optimization of M simultaneous frequencies delivered to a heterogeneous lung model with N terminal viscoelastic acini [1], we defined an input oscillatory waveform as a sum of sinusoids with M discrete frequencies and amplitudes. We further defined an objective function Φ , as the coefficient of variation of acinar root-mean-square volumes:

$$\Phi = \bar{V}_{\text{rms}}^{-1} \sqrt{\frac{1}{N} \sum_{n=1}^N (V_{\text{rms},n} - \bar{V}_{\text{rms}})^2}$$

where $V_{\text{rms},n}$ is the root-mean-square volume over time in the n^{th} acinus, and \bar{V}_{rms} is the average across all N acini. Minimization of Φ therefore minimizes acinar strain heterogeneity. For each value of M (i.e. 1, 2, 3, ...), 100 randomized initial guesses based on a Monte Carlo technique were used for a numerical constrained nonlinear minimization routine (MATLAB v8.4, The Mathworks Inc., Natick MA).

Results & Discussion: The optimal solution for small numbers of frequencies (i.e. $M \leq 4$) was easily determined using a random search over the design variable space. Figure 1 shows the optimal solution found using random search over 3 frequencies. The optimal solution for $M > 4$ frequencies became a poorly defined problem due to the presence of many local minima in Φ . Nonetheless, the optimal solution for $M + 1$ frequencies generally included the same frequencies found in the unique solution for M frequencies, with a similar amplitude distribution.

Conclusions: Superposition of multiple simultaneous frequencies provides more uniform ventilation distribution compared to single frequency oscillatory ventilation, with less potential for VILI. An optimal combination of frequencies, amplitudes, and phases in an oscillatory ventilator waveform may be determined according to the frequency-dependent distribution of flows throughout a heterogeneous lung periphery.

References:

- [1] AA Colletti, R Amini, DW Kaczka. *Comput Biol Med*, 2011. 41(10): 936-945.
- [2] DW Kaczka et al. *Anesthesiology*, 2015. 123(6):1394-1403.

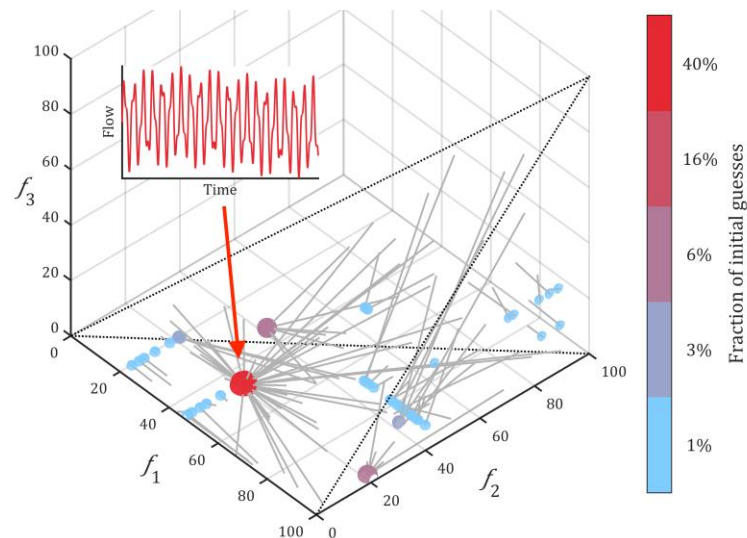


Figure 1. Convergence of the minimization algorithm from randomized initial guesses (indicated by grey lines) to local minima (colored spheres). In this case, the optimal solution (red sphere) for $M = 3$ frequencies (f_1, f_2, f_3 shown in Hz) yielded 27% reduction in Φ compared to the optimal solution for $M = 1$ frequency. The resulting optimized flow waveform over one second is shown.

Frequency-Selective CT Image Registration for Assessment of Regional Periodic Lung Deformation

Jacob Herrmann¹, Wei Shao¹, Joseph Reinhardt¹, Eric Hoffman¹, Gary Christensen¹, and David Kaczka¹¹University of Iowa, Iowa City, IA

Introduction: Mechanical ventilation is a life-sustaining intervention delivering flow and pressure to maintain gas exchange in patients with acute respiratory failure. Regional maldistribution of ventilation may unintentionally result in ventilation-to-perfusion mismatching or ventilator-induced lung injury (VILI), especially in mechanically-heterogeneous injured lungs. High-frequency oscillatory ventilation (HFOV) is an alternative ventilation modality designed to minimize VILI through the delivery of small tidal volumes at high instantaneous flow rates. However, the distribution of flow throughout the lung during HFOV may be heterogeneous and frequency-dependent. Multi-frequency oscillatory ventilation (MFOV) has been recently proposed to enhance lung-protective ventilation by delivering flow at multiple frequencies simultaneously [1]. In this study, we used Frequency-Selective CT (FSCT) imaging [2] combined with four-dimensional (4D) image registration [3] to compare the regional distributions of periodic structural deformation during HFOV and MFOV.

Materials & Methods: Experiments were approved by the University of Iowa Institutional Animal Care and Use Committee (Protocol number 5031314). Sedated and paralyzed pigs were ventilated using conventional mechanical ventilation (CMV) at a rate of 20 min⁻¹ and tidal volume between 10-12 mL kg⁻¹, HFOV delivered at 5 Hz, and MFOV delivered using uniform flow amplitudes at 5, 10, 15, and 20 Hz, and scanned using a Siemens Somatom Force. FSCT was used to reconstruct temporally-resolved image sequences of structural deformations during periodic ventilation [2]. A 4D tissue-volume preserving image registration technique was then used to obtain regional maps of expansion and contraction relative to a single arbitrarily-selected reference image [3]. Within each region-of-interest in the reference image, periodic expansion and contraction were assessed by the discrete Fourier transform of the normalized time-varying Jacobian determinants.

Results & Discussion: Total volumetric strain (peak-to-peak mean \pm standard deviation) during HFOV ($7.9\% \pm 3.1\%$) and MFOV ($6.9\% \pm 2.5\%$) were substantially lower than during CMV ($31.3\% \pm 11.6\%$). The distribution of strain amplitudes during HFOV delivered at 5 Hz tended to vary primarily in the ventral-dorsal direction, in accordance with the gravitational field in supine position (Figure 1). Regional strain amplitudes during MFOV varied with frequency, with different lung regions selectively filtering the harmonic frequency content of the broadband oscillatory flow.

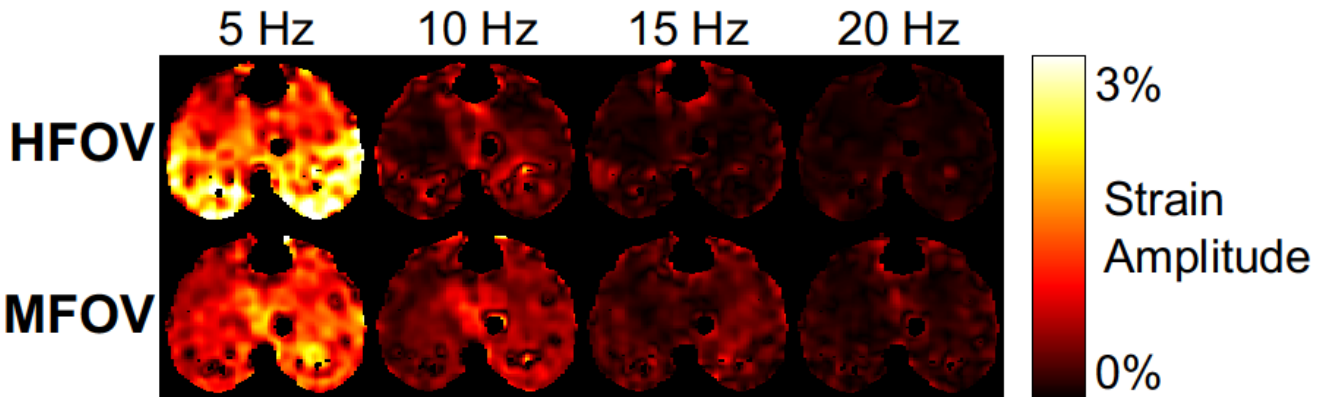


Figure 1: Regional distributions of volumetric strain amplitudes during HFOV and MFOV shown in transverse cross-section, using discrete Fourier transform of normalized time-varying Jacobian determinants.

Conclusion: Parenchymal stretch during oscillatory ventilation is regionally heterogeneous and frequency-dependent. The broadband spectral content of multi-frequency oscillatory ventilation may enhance gas transport in the presence of periodic parenchymal deformation with higher harmonics, which may be further adjusted to compensate for patient-specific regional heterogeneity.

References:

- [1] DW Kaczka et al. *Anesthesiology* 123(6):1394-1403, 2015.
- [2] J Herrmann, EA Hoffman, DW Kaczka. *IEEE Trans Med Imaging*, 2017. In press.
- [3] B Zhao et al. *Proc IEEE Conf Comput Vis Pattern Recognit* 41-49, 2016.

Computational Modeling of Primary Blast Lung Injury: Implications for Ventilator Management

Jacob Herrmann¹, Merryn H. Tawhai², David W. Kaczka¹

¹ University of Iowa, Iowa City, IA

² University of Auckland, Auckland, New Zealand

Background

Primary blast lung injury (PBLI) is a potentially fatal condition affecting victims in proximity to explosive detonations in combat and terrorist attack settings. Sudden stresses and strains throughout the lung are induced by pressure waves, resulting in parenchymal tissue damage and derecruitment, alveolar hemorrhage, air emboli, and/or pneumothoraces. The resulting structural injuries may lead to severe ventilation-perfusion mismatch, hypoxia, and respiratory failure. Although mechanical ventilation is often required in blast victims, maldistribution of gas flow in a mechanically heterogeneous lung may lead to further injury. In this study, we developed a computational model of a human lung to simulate the effects of PBLI on the distribution of gas flow during mechanical ventilation.

Methods

A computational model of a human airway network was generated using central airways obtained from segmented X-ray computed tomographic scans, and algorithmically generated peripheral airways (M.H. Tawhai *et al.*, *J Appl Physiol* 97(6):2310-2321, 2004). The model consisted of 60,494 cylindrical airway segments, with 30,243 terminal bronchi subtended by viscoelastic acini. Distributed mechanical properties of tissues and airways were simulated to represent typical healthy and blast-injured lungs, the latter characterized by bilateral derecruitment and increased tissue stiffness, focusing on the perihilar regions of the model. Gas flow delivered at the airway opening was distributed throughout the lung according to regional mechanical impedance, at frequencies ranging from conventional mechanical ventilation (0.2 Hz) to high-frequency oscillatory ventilation (2 to 20 Hz).

Results

Delivered flow was heterogeneously distributed in the blast-injured lung during both conventional mechanical ventilation and high-frequency oscillatory ventilation. During conventional mechanical ventilation, flow was distributed primarily according to local tissue stiffness. At higher frequencies, the distribution of flow became increasingly heterogeneous and frequency-dependent, with some regions being underventilated while other regions experienced substantially greater distension.

Conclusion

The distribution of parenchymal distension during mechanical ventilation depends on injury severity and ventilatory modality. Computational modeling may aid in predicting the progression of ventilator-induced lung injury, and may also provide a means for investigating alternative ventilation modalities employing lung-protective strategies.

Multi-Objective Optimization of Multi-Frequency Oscillatory Ventilation

Jacob Herrmann¹, Merryn Tawhai², and David Kaczka¹

¹University of Iowa, Iowa City, IA, ²University of Auckland, Auckland, New Zealand

Introduction: Ventilator-induced lung injury (VILI) in mechanically ventilated patients may result from extreme stresses, strains, and strain rates associated with parenchymal overdistension, as well as repetitive alveolar collapse and reopening. VILI is especially hazardous within injured lungs, in which mechanical heterogeneity leads to heterogeneous and frequency-dependent distribution of peripheral flows and pressures. Multi-frequency oscillatory ventilation (MFOV) is a novel lung-protective ventilatory modality, relying on the delivery of oscillatory flows at multiple simultaneous frequencies. With appropriate spectral energy content, MFOV waveforms can provide more even ventilation distribution compared to traditional single-frequency oscillatory ventilation (SFOV) [1]. Since the goal of MFOV is to improve morbidity and mortality in ventilated patients, we hypothesized that the spectral content of MFOV waveforms could be tuned to minimize risk for VILI. To test this hypothesis, we developed a computational lung model to optimize the spectral content of simulated MFOV waveforms. Various objective functions were used to modulate the relative contributions of strain, strain rate, and mechanical power imparted to the parenchymal tissues [2].

Methods: The computational model consisted of a central airway tree segmented from a computed tomographic image of a supine pig, with algorithmically generated peripheral airways. The model consisted of 60,494 airway segments in total, with 30,243 viscoelastic acini. Eucapnic ventilation was simulated using a Monte Carlo technique, to choose from MFOV waveforms consisting of four frequencies (5, 10, 15, and 20 Hz) with randomized volume amplitudes and phases. Corresponding distributions of acinar strain, strain rate, and mechanical power throughout the model were determined for each MFOV waveform, and used to compute objective functions with variable emphasis on the relative percent contribution to VILI.

Results: Our simulations demonstrated that MFOV waveforms were superior to SFOV for both healthy and injured lung models. The optimized volume amplitudes at each frequency in the MFOV waveform were modulated according to the relative objective function weighting of strain vs. strain rate, as well as the degree of lung mechanical heterogeneity. Increasing contribution of strain rate to VILI, as opposed to strain, resulted in decreasing volume amplitudes at higher frequencies in the optimized MFOV waveforms. Alternatively, optimized MFOV waveforms minimizing mechanical power tended to favor increased volume amplitudes at higher frequencies (Figure 1).

Conclusion: These results in a computational lung model indicate that frequency content in MFOV waveforms may be tuned to minimize risk for VILI. Our unique modeling and optimization approaches allow for the selection of patient-specific MFOV waveforms, especially when combined with experimental evidence to justify physiologically-relevant objective emphasis on parenchymal injury.

References:

- [1] DW Kaczka et al. *Anesthesiology* 123(6):1394-1403, 2015.
- [2] L Gattinoni et al. *Intensive Care Med* 42(10):1567-1575, 2016.

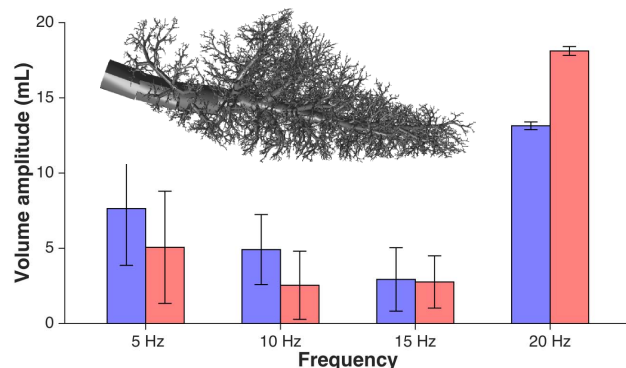


Figure 1. Computational model of porcine lung (inset). Optimal volume amplitudes at each frequency are shown, representing the mean and standard deviation of the waveforms producing the lowest percentile of mechanical power in healthy (blue) and injured (red) conditions.

1
2
3
4
5 **Parenchymal Strain Heterogeneity During Oscillatory Ventilation:**
6 **Why Two Frequencies are Better than One**
7
8
9

10 Jacob Herrmann ^{1,2}
11 Merryn H. Tawhai ³
12 David W. Kaczka ^{1,2,4}
13
14

¹ Department of Anesthesia
University of Iowa
Iowa City, Iowa

² Department of Biomedical Engineering
University of Iowa
Iowa City, Iowa

³ Auckland Bioengineering Institute
University of Auckland
Auckland, New Zealand

⁴ Department of Radiology
University of Iowa
Iowa City, Iowa

36 Address Correspondence to:
37

38 David W. Kaczka
39 Department of Anesthesia
40 The University of Iowa Hospital and Clinics
41 200 Hawkins Drive
42 Iowa City, IA 52242
43 Voice: 319-356-0772
44 Fax: 319-356-1120
45 Email: david-kaczka@uiowa.edu
46

47 **ABSTRACT**

48 High frequency oscillatory ventilation (HFOV) relies on low tidal volumes cycled at
49 supraphysiologic rates, producing fundamentally different mechanisms for gas transport and
50 exchange compared with conventional mechanical ventilation. Despite the appeal of using low
51 tidal volumes to mitigate the risks of ventilator-induced lung injury (VILI), HFOV has not
52 improved mortality for most clinical indications. This may be due to non-uniform and
53 frequency-dependent distribution of flow throughout the lung. The goal of this study was to
54 compare parenchymal strain heterogeneity during eucapnic HFOV when using oscillatory
55 waveforms that consisted of either a single discrete frequency or two simultaneous frequencies.
56 We utilized on a three-dimensional, anatomically-structured canine lung model for simulating
57 frequency-dependent ventilation distribution. Gas transport was simulated via direct alveolar
58 ventilation, advective mixing at bifurcations, turbulent and oscillatory dispersion, and molecular
59 diffusion. Volume amplitudes at each oscillatory frequency were iteratively optimized to attain
60 eucapnia. Ventilation using single-frequency HFOV demonstrated increasing heterogeneity of
61 acinar flow and CO₂ elimination with frequency, for frequencies greater than the resonant
62 frequency. For certain pairs of frequencies, a linear combination of the two corresponding
63 ventilation distributions yielded reduced acinar strain heterogeneity compared to either frequency
64 alone. Our model demonstrates that superposition of two simultaneous oscillatory frequencies
65 can achieve more uniform ventilation distribution, and therefore lessen the potential for
66 ventilator-induced lung injury, compared to traditional single-frequency HFOV.

67 (219 / 250 words)

68

69

70 **NEW & NOTEWORTHY**

71 In this study we simulated oscillatory ventilation with multiple simultaneous frequencies using a
72 computational lung model that includes distributed flow and gas transport. A mechanism of
73 benefit was identified by which ventilation with two simultaneous frequencies results in reduced
74 acinar strain heterogeneity compared to either frequency alone. This finding suggests the
75 possibility of tuning the spectral content of ventilator waveforms according to patient-specific
76 mechanical heterogeneity.

77 (65 / 75 words)

78

79 **Keywords:** Computational models, Biological models, oscillatory ventilation, Ventilation
80 distribution, Disease models, Animal, Lung pathology, Respiratory mechanics

81

82

83 **NOMENCLATURE**

84	A_S	Area of cross-section S
85	ARDS	Acute respiratory distress syndrome
86	CO_2	Carbon dioxide
87	CT	Computed tomography
88	d	Diameter of airway segment
89	D_{eff}	Effective diffusivity
90	D_{mol}	Molecular diffusivity
91	$D_{\text{dis}}^{\text{lam}}$	Laminar oscillatory dispersion coefficient
92	$D_{\text{dis}}^{\text{turb}}$	Turbulent oscillatory dispersion coefficient
93	f	Oscillation frequency in Hz
94	f_{res}	Resonant frequency in Hz
95	F	Fluid velocity amplitude distribution
96	G	Concentration amplitude distribution
97	HFOV	High-frequency oscillatory ventilation
98	j	Unit imaginary number, equal to $\sqrt{-1}$
99	J_n	Peak volumetric strain in the n^{th} acinus
100	k	Index through oscillation frequencies
101	K	Number of discrete oscillation frequencies in multi-frequency waveform
102	l	Length of airway segment
103	MFOV	Multi-frequency oscillatory ventilation
104	$\dot{M}_n \text{CO}_2$	Molar flux of CO_2 for n^{th} acinus
105	$\dot{\mathbf{M}} \text{CO}_2$	Vector of acinar CO_2 molar fluxes

106	n	Index through individual acini
107	N	Total number of acini
108	P_{atm}	Atmospheric pressure
109	ΔP_{CO_2}	Vector of CO ₂ partial pressure differentials between acini and airway opening
110	r	Correlation coefficient
111	\mathcal{R}	Universal gas constant
112	$\Re\{\dots\}$	Real part of the complexed-valued argument
113	Re	Reynolds number
114	Re _{crit}	Critical Reynolds number, transition between laminar and turbulent flow
115	$R_{\text{T}}^{\text{diff}}$	Diffusive transport resistance
116	$R_{\text{T}}^{\text{mix}}$	Diffusive transport resistance
117	$R_{\text{T}}^{\text{tot}}$	Total transport resistance
118	\mathbf{R}_{T}	Transport resistance matrix
119	t	Time
120	T	Temperature
121	\bar{U}_{RMS}	Root-mean-square mean-axial velocity
122	V_{D}	Total dead space volume
123	$ V_{\text{D},n} $	Magnitude of oscillatory dead space volume delivered to n^{th} acinus
124	$ V_{\text{F},n} $	Magnitude of oscillatory fresh gas volume delivered to n^{th} acinus
125	V_{mix}	Oscillatory mixing volume
126	V_n	Time-varying volume of the n^{th} acinus
127	V_{seg}	Volume of airway segment
128	V_{T}	Tidal volume

129	V_T^{euc}	Eucapnic tidal volume
130	$ \dot{V}_{\text{seg}} $	Magnitude of oscillatory flow through airway segment
131	\dot{V}_{ao}	Flow at the airway opening
132	\dot{V}_A	Eucapnic total acinar ventilation
133	$\dot{V}_{\text{ao}}^{\text{DDM}} \text{CO}_2$	CO_2 elimination at the airway opening <i>via</i> diffusion, dispersion, and mixing
134	$\dot{V}_n \text{CO}_2$	CO_2 elimination at acinus n
135	$\dot{V}_n^{\text{DDM}} \text{CO}_2$	CO_2 elimination at acinus n <i>via</i> diffusion, dispersion, and mixing
136	$\dot{V}_n^{\text{DAV}} \text{CO}_2$	CO_2 elimination at acinus n <i>via</i> direct acinar ventilation
137	$\dot{V}_{\text{tot}} \text{CO}_2$	Total CO_2 elimination at the airway opening
138	$\dot{V}_{\text{tot}}^{\text{euc}} \text{CO}_2$	Eucapnic total CO_2 elimination at the airway opening
139	$\mathcal{S}_{\dot{V}}$	Flow distribution similarity index
140	S	Cross-section of airway
141	VILI	Ventilator-induced lung injury
142	w	Fluid velocity
143	x, y, z	Spatial coordinate axes
144	863	Conversion factor between partial pressure in mmHg and gas volume fraction, accounting for the difference between standard temperature and pressure dry air, and body temperature and pressure air saturated with water vapor.
145		
146		
147	β	Relative amplitude scaling factor for multi-frequency oscillatory ventilation waveform
148		
149	γ	Concentration gradient
150	$\varepsilon_{V,n}$	Volumetric strain at acinus n
151	θ	Concentration

152	π	Radians in semi-circle
153	ν	Kinematic viscosity
154	ϕ	Phase offset of sinusoidal flow oscillation
155	Ψ_{euc}	Eucapnic flow amplitude scaling factor of multi-frequency oscillatory ventilation
156		waveform
157	ω	Angular frequency
158		
159		
160		

161 **INTRODUCTION**

162 High-frequency oscillatory ventilation (HFOV) relies on low tidal volumes cycled at
163 supraphysiologic rates, which produces fundamentally different mechanisms for gas transport
164 compared with conventional mechanical ventilation. Despite the appeal of using low tidal
165 volumes to mitigate the risks of ventilator-induced lung injury (VILI) in conditions such as the
166 acute respiratory distress syndrome (ARDS), HFOV has not improved mortality in most clinical
167 applications (8, 22, 23, 38). The nonsuperiority of HFOV over conventional mechanical
168 ventilation (CMV) may be due to its tendency to distribute flow throughout the lung in a non-
169 uniform and frequency-dependent manner, especially in the presence of lung tissue mechanical
170 heterogeneity (4, 6). Reductions in prescribed tidal volume during HFOV may therefore be
171 counterbalanced by increased strain heterogeneity (13). That is, oscillatory ventilation at a single
172 discrete frequency may result in some lung regions being underventilated and predisposed to
173 atelectrauma, while other regions are overventilated and subject to volutrauma (3). VILI has also
174 been associated with increased strain rate (26) and mechanical power (11), which depend on both
175 frequency and amplitude of oscillatory stretch and therefore may be regionally amplified during
176 heterogeneous ventilation. Thus, maldistribution of oscillatory flow may increase the risk for
177 worsening VILI. Furthermore heterogeneous distribution of flow may contribute to ventilation-
178 perfusion mismatching and inefficient gas exchange (13).

179 In a previous study of HFOV in preterm lambs (16), we demonstrated that oscillation
180 with multiple *simultaneous* frequencies resulted in improved gas exchange and lung recruitment
181 at lower distending pressures, compared to more traditional ‘single-frequency’ oscillatory
182 ventilation. We hypothesized that these short-term physiologic improvements resulted from a
183 more even distribution of ventilation throughout the heterogeneous surfactant-deficient lung. We

184 further conjectured that during ‘multi-frequency’ oscillatory ventilation (MFOV), flow
185 oscillations are distributed throughout the injured lung in accordance with local mechanical
186 properties of the parenchyma and air-liquid interface. Thus particular regions of the lung may be
187 preferentially ventilated by some frequencies, yet simultaneously reject other frequencies (4, 13).
188 Such a mechanical filtering effect during MFOV waveform may maximize the participation of
189 various lung regions in gas exchange, despite different ‘preferred’ frequencies within each
190 region. As a result, MFOV may produce more efficient CO₂ elimination compared to traditional
191 single-frequency oscillatory ventilation, along with a possible reduction in net parenchymal
192 strain heterogeneity and less potential for VILI.

193 In this study, we hypothesized that oscillatory ventilation with two simultaneous
194 frequencies results in more uniform parenchymal strain distribution compared to oscillation with
195 either frequency alone, with a reduction in peak strains required to maintain eucapnic CO₂
196 elimination. To test this hypothesis we relied on our previously published computational model
197 of the canine lung (13), which allowed for simulated gas transport via direct alveolar ventilation,
198 mixing at bifurcations, turbulent and oscillatory dispersion, as well as molecular diffusion. We
199 compared the distributions of parenchymal strain during traditional single frequency HFOV, and
200 then selected candidate pairs of frequencies for dual-frequency oscillatory ventilation based on a
201 ventilation distribution similarity index. Finally, we assessed whether such a similarity index
202 can be an appropriate criterion for selecting complementary frequencies during dual-frequency
203 oscillatory ventilation.

204

205 **METHODS**206 Model Overview

207 A complete description of our computational lung model can be found in Herrmann et al.
208 (13). Briefly, the model structure is based on a three-dimensional central airway tree, segmented
209 from a computed tomographic image of a supine dog. Peripheral airways with diameters smaller
210 than 2 mm were generated using a space-filling algorithm (34). The model consisted of 40,085
211 cylindrical airway segments in total, with 19,932 viscoelastic acini. Each airway segment was
212 characterized by a unique length l and diameter d , with luminal volume given by:

$$V_{\text{seg}} = \frac{1}{4}\pi d^2 l. \quad (1)$$

213 Regional pleural pressure was assumed to vary with gravity according to the hydrostatic weight
214 of the lung in a supine orientation by 0.25 cmH₂O per cm lung height (19, 21), with an average
215 value of -5 cmH₂O. Acinar viscoelasticity was determined according to a second-order
216 polynomial function of local transpulmonary pressure (4, 6, 18). Longitudinal and shunt
217 impedances for each airway segment accounted for pressure losses associated with oscillatory
218 flow, isothermal gas compression, as well as soft tissue and cartilaginous viscoelasticity (17).
219 Flow oscillations delivered at the trachea were distributed throughout the lung periphery using a
220 recursive flow-dividing scheme, according to the local input impedance at each node in the tree
221 (6). Flow in each segment was characterized as laminar or turbulent according to the Reynolds
222 number Re (31):

$$\text{Re} = \frac{\bar{U}_{\text{RMS}}d}{\nu}, \quad (2)$$

223 where \bar{U}_{RMS} is the root-mean-square of the time-varying mean axial velocity and ν is kinematic
 224 viscosity of the gas. The transition from laminar to turbulent oscillatory flow was assumed to
 225 occur at the critical Reynolds number $\text{Re}_{\text{crit}} = 30$ (14, 31).

226 *Gas Transport Mechanisms*

227 The transport of CO₂ throughout the airway network was solved as a steady-state
 228 problem, being time-averaged throughout the oscillatory ventilation cycle and with total CO₂
 229 elimination equal to metabolic CO₂ production (13). The molar flux of CO₂ through each airway
 230 segment was driven by a concentration gradient, and characterized by its effective diffusivity
 231 D_{eff} :

$$D_{\text{eff}} = \begin{cases} D_{\text{mol}} + \sum_{k=1}^K D_{\text{dis}}^{\text{lam}}(f_k) & , \quad \text{Re} < \text{Re}_{\text{crit}} \\ D_{\text{mol}} + D_{\text{dis}}^{\text{tur}} & , \quad \text{Re} \geq \text{Re}_{\text{crit}} \end{cases}. \quad (3)$$

232 During laminar oscillatory flow at multiple frequencies (i.e., $\text{Re} < \text{Re}_{\text{crit}}$), D_{eff} is equal to the
 233 sum of its molecular diffusivity D_{mol} and the laminar dispersion coefficients $D_{\text{dis}}^{\text{lam}}$ computed at
 234 each discrete frequency f_k (Appendix A-1). However during turbulent oscillatory flow, D_{eff} is
 235 equal to the sum of D_{mol} and the frequency-independent dispersion coefficient $D_{\text{dis}}^{\text{tur}}$ (9, 35) of the
 236 form:

$$D_{\text{dis}}^{\text{tur}} = 0.7 \bar{U}_{\text{RMS}} d. \quad (4)$$

237 Equation (4) is consistent with previous computational studies (9, 30) based on theoretical (35)
 238 and experimental results (29). Oscillatory flows were assumed to be either fully laminar or fully
 239 turbulent, ignoring transitional flows. The resulting CO₂ transport resistance due to diffusion
 240 and dispersion is given by:

$$R_{\text{T}}^{\text{diff}} = \frac{4\mathcal{R}Tl}{\pi d^2 D_{\text{eff}}}, \quad (5)$$

241 where \mathcal{R} is the universal gas constant and T is absolute temperature of the gas.

242 In our previous model of convective gas transport (13), we described the linear transport
243 resistance due to gas mixing (R_T^{mix}) during repeated division and recombination of oscillatory
244 flow past airway bifurcations during oscillation at a single discrete frequency. With this
245 approach, R_T^{mix} is characterized by the oscillation frequency, f , and the mixing volume, V_{mix} ,
246 which quantifies the volume of gas that passes completely through an airway during each period
247 of oscillation. However during oscillation with multiple simultaneous frequencies, V_{mix} is
248 computed over one period of the fundamental frequency (f_0) of the broadband flow waveform:

$$V_{\text{mix}} = \int_0^{1/f_0} \dot{V}_{\text{mix}}(t) dt, \quad (6)$$

249 where \dot{V}_{mix} is the flow contributing to V_{mix} , given by:

$$\dot{V}_{\text{mix}}(t) = \begin{cases} \dot{V}(t) & , \quad [\dot{V}(t) > 0] \text{ and } [V(t) > V_{\text{seg}}] \\ 0 & , \quad \text{otherwise} \end{cases}. \quad (7)$$

250 $\dot{V}(t)$ is the time-varying flow in an airway segment, V_{seg} is the luminal volume of the airway
251 segment, and $V(t)$ is the time integral of flow:

$$V(t) = \int_0^t \dot{V}(\tau) d\tau. \quad (8)$$

252 In practice, V_{mix} may be computed using numerical integration techniques (15). An example
253 flow waveform through a hypothetical airway segment of volume 70 mL, along with the
254 corresponding \dot{V}_{mix} and V_{mix} for the segment, is shown in Figure 1. For the special case of
255 single-frequency oscillation, this numerical computation of V_{mix} is consistent with the analytical
256 expression for V_{mix} in our previous model (13). The resulting gas transport resistance due to
257 mixing, R_T^{mix} , is then given by:

$$R_T^{\text{mix}} = \frac{\mathcal{R}T}{f_0 V_{\text{mix}}} . \quad (9)$$

258 The total transport resistance, R_T^{tot} , in each airway segment is given by the parallel combination
 259 of diffusive/dispersive and mixing resistances:

$$R_T^{\text{tot}} = \left(\frac{1}{R_T^{\text{diff}}} + \frac{1}{R_T^{\text{mix}}} \right)^{-1} . \quad (10)$$

260 R_T^{tot} describes the relationship between CO₂ molar flux through an airway segment and CO₂
 261 partial pressure difference across the airway segment. Combining the transport resistances of all
 262 airways in the model yields a system of equations describing the relationship between acinar CO₂
 263 partial pressure $P_n \text{CO}_2$ and acinar CO₂ molar flux due to diffusion, dispersion, and mixing
 264 $\dot{M}_n \text{CO}_2$:

$$\mathbf{R}_T \dot{\mathbf{M}} \text{CO}_2 = \Delta \mathbf{P} \text{CO}_2 , \quad (11)$$

265 where \mathbf{R}_T is a full matrix of transport resistances, $\dot{\mathbf{M}} \text{CO}_2$ is a vector of acinar CO₂ molar fluxes,
 266 and $\Delta \mathbf{P} \text{CO}_2$ is a vector of CO₂ partial pressure differentials between acini and airway opening
 267 (13). After solving Equation (11) to obtain $\dot{\mathbf{M}} \text{CO}_2$, acinar CO₂ elimination due to diffusion,
 268 dispersion, and mixing, $\dot{V}_n^{\text{DDM}} \text{CO}_2$, is computed as:

$$\dot{V}_n^{\text{DDM}} \text{CO}_2 = \frac{\mathcal{R}T}{P_{\text{atm}}} \dot{M}_n \text{CO}_2 . \quad (12)$$

269 During ventilation with large tidal volumes, gas transport occurs primarily via direct ventilation,
 270 whereby fresh gas is advected directly between the airway opening and acini. Under such
 271 circumstances, CO₂ elimination from the n^{th} acinus due to convective ventilation, $\dot{V}_n^{\text{DAV}} \text{CO}_2$, is
 272 determined by the rate of fresh gas delivery:

$$\dot{V}_n^{\text{DAV}}\text{CO}_2 = \frac{P_n\text{CO}_2}{863} \sum_{k=1}^K f_k \cdot |V_{F,n}(f_k)|, \quad (13)$$

273 where $P_n\text{CO}_2$ is the CO_2 partial pressure of the n^{th} acinus, 863 is a conversion factor between
 274 partial pressure in mmHg and gas volume fraction (13), and $V_{F,n}(f_k)$ is the fresh gas delivered to
 275 the n^{th} acinus per oscillation at the k^{th} frequency:

$$|V_{F,n}(f_k)| = \sum_{k=1}^K \max\left(0, \frac{|\dot{V}_n(f_k)|}{\pi f_k} - |V_{D,n}^*|\right), \quad (14)$$

276 where $|\dot{V}_n(f_k)|$ is the magnitude of oscillatory flow delivered at the k^{th} frequency. Total CO_2
 277 elimination for each acinus, $\dot{V}_n\text{CO}_2$, is computed as the sum of $\dot{V}_n^{\text{DDM}}\text{CO}_2$ and $\dot{V}_n^{\text{DAV}}\text{CO}_2$. Total
 278 CO_2 elimination for the entire lung model, $\dot{V}_{\text{tot}}\text{CO}_2$, is then the sum of $\dot{V}_n\text{CO}_2$ across all acini:

$$\dot{V}_{\text{tot}}\text{CO}_2 = \sum_{n=1}^N (\dot{V}_n^{\text{DDM}}\text{CO}_2 + \dot{V}_n^{\text{DAV}}\text{CO}_2). \quad (15)$$

279 Figure 2 illustrates which of the modeled gas transport mechanisms dominates overall gas
 280 transport during eucapnic single-frequency ventilation between 0.3 Hz and 26 Hz. Direct acinar
 281 ventilation accounts for the majority of total respiratory gas exchange at low frequencies (i.e.,
 282 below 2 Hz), yet is entirely absent at high frequencies (i.e., above 5 Hz). The greatest
 283 contribution to the overall rate of gas transport in individual airways derives from the transport
 284 mechanism describing bifurcation mixing due to the repetitive division and recombination of
 285 gases. The contribution of turbulent mixing to gas transport in individual airways increases at
 286 higher frequencies, dominating in the larger central airways during delivery of small volume
 287 amplitudes at high instantaneous flow rates. This behavior is consistent with the analysis of
 288 bifurcating flow regimes by Jan et al. (14) as well as the numerical simulations performed by
 289 Choi et al. (5).

290 Comparison of Single-Frequency and Dual-Frequency Oscillation

291 To identify plausible candidate frequency pairs for dual-frequency simulations, each
 292 combination of two distinct oscillatory frequencies was considered by taking the inner product
 293 between their respective normalized acinar flow distributions:

$$\mathcal{S}_{\dot{V}}(f_1, f_2) = \frac{\sum_{n=1}^N |\dot{V}_n(f_1)| |\dot{V}_n(f_2)|}{\sqrt{\sum_{n=1}^N |\dot{V}_n(f_1)|^2} \sqrt{\sum_{n=1}^N |\dot{V}_n(f_2)|^2}}, \quad (16)$$

294 where $\mathcal{S}_{\dot{V}}$ —the value of the inner product—quantifies the ventilation distribution similarity.
 295 Thus $\mathcal{S}_{\dot{V}} = 1$ implies two identical distributions, whereas $\mathcal{S}_{\dot{V}} = 0$ implies two orthogonal
 296 distributions. Figure 3 shows a schematic lung with three mechanically heterogeneous
 297 compartments as a simplified example of quantifying ventilation distribution similarity.

298 Figure 4A shows the contours of $\mathcal{S}_{\dot{V}}$ for each permutation of two frequencies from 0.2
 299 Hz to 40 Hz, spaced over 0.2 Hz intervals. Identifying pairs of frequencies with the lowest
 300 degree of similarity (i.e., the smallest values of $\mathcal{S}_{\dot{V}}$) reveals the most complementary pairs, i.e.,
 301 those pairs which are most able to compensate for each other's respective underventilated and
 302 overventilated regions. Alternatively, the Pearson correlation coefficient (r) between normalized
 303 acinar flow distributions for each frequency pair can also be used to identify complementary
 304 distributions. Positive values of r correspond to similar distributions, such that acini tend to
 305 receive either above-average or below-average amounts of flow at both frequencies. By contrast,
 306 negative values of r correspond to dissimilar distributions, such that acini tend to receive above-
 307 average flow at one frequency yet below-average at the other. Figure 4B shows the contours of
 308 r for each permutation of two frequencies between 0.2 Hz and 40 Hz. Identifying pairs of

309 frequencies with the most negative correlation coefficients reveals the most complementary
310 pairs.

311 Based on the contour maps shown in Figure 4, we selected a pair of frequencies
312 representing a low value of $\mathcal{S}_{\dot{V}}$ (i.e., dissimilar ventilation distributions) for simulation of gas
313 transport. We selected the local minimum of the $\mathcal{S}_{\dot{V}}$ contour map corresponding to 12 Hz and 26
314 Hz. For comparison, another pair of frequencies with a high value of $\mathcal{S}_{\dot{V}}$ was also selected for
315 simulation, at 0.3 Hz and 12 Hz. For each pair of frequencies, multiple waveforms were
316 constructed to define flow at the airway opening (\dot{V}_{ao}) according to the following template:

$$\dot{V}_{ao}(t) = \Psi_{euc}[\beta \sin(2\pi f_1 t) + (1 - \beta) \sin(2\pi f_2 t + \phi)], \quad (17)$$

317 where β is a scaling factor adjusting the relative contributions of f_1 versus f_2 such that $0 \leq \beta \leq$
318 1, ϕ is the relative phase offset between the flow oscillations such that $0 \leq \phi \leq 2\pi$, and
319 $\Psi_{euc} > 0$ is a scaling factor used to adjust the flow amplitudes delivered by the MFOV
320 waveform. For any combination of f_1 , f_2 , β , and ϕ , the corresponding value of Ψ_{euc} was
321 iteratively optimized to attain eucapnic CO₂ elimination, which was approximated according to
322 the assumed weight of the animal (13). For simplicity, the value of ϕ was constrained to be zero
323 for all simulations.

324 Following the determination of eucapnic scaling, the distribution of peak acinar
325 volumetric strain ($\varepsilon_{V,n}$) was computed by calculating the range of time-varying acinar volume,
326 $V_n(t)$, divided by the minimum value:

$$\varepsilon_{V,n} = \frac{\max[V_n(t)] - \min[V_n(t)]}{\min[V_n(t)]}. \quad (18)$$

327 The distribution of acinar root-mean-square volume ($V_{\text{RMS},n}$) was also used to assess distributed
328 ventilation heterogeneity:

$$V_{\text{RMS},n} = \sqrt{f_0 \int_0^{1/f_0} [V_n(t) - \bar{V}_n]^2 dt} , \quad (19)$$

329 where \bar{V}_n is time-averaged acinar volume given by:

$$\bar{V}_n = f_0 \int_0^{1/f_0} V_n(t) dt . \quad (20)$$

330 The values of $V_{\text{RMS},n}$ and \bar{V}_n in Equations (19) and (20) were numerically approximated using
331 trapezoidal integration (15).

332 Simulations

333 The recursive algorithms for computing and storing impedances and determining
334 advective flow division throughout the tree were written in C++. Computation time for
335 generating advective flow distribution at each distinct f was ~ 3 s on a 64-bit computer with an
336 Intel Core i7-950 processor operating at 3.07 GHz with 12 GB RAM. The gas transport model
337 was written and executed in MATLAB (version R2016a, The Mathworks, Natick, MA). Total
338 computation time for each distinct dual-frequency simulation was ~ 70 s.¹

339

340

¹ A sample MATLAB script for computing the gas transport model is available from the authors upon request.

341 **RESULTS**

342 Two pairs of frequencies were selected for gas transport simulations based on ventilation
343 distribution similarity ($\mathcal{S}_{\dot{V}}$) and correlation coefficient (r), as indicated by the labeled points on
344 the contour maps of Figure 4. The frequency pair with similar distributions was chosen at 0.3 Hz
345 and 12 Hz, with $\mathcal{S}_{\dot{V}} = 0.98$ and $r = +0.69$. The pair with dissimilar distributions was chosen at
346 12 Hz and 26 Hz, with $\mathcal{S}_{\dot{V}} = 0.85$ and $r = -0.64$. Figure 5 shows the anatomic distributions of
347 acini receiving relatively more or less oscillatory flow at 0.3 Hz, 12 Hz, and 26 Hz compared to a
348 perfectly uniform distribution. Acinar flow magnitudes were normalized relative to their
349 corresponding values for a symmetric, homogeneous lung with rigid airway walls and no gas
350 compression (6). Figure 6 shows scatter plots comparing normalized ventilation distributions
351 between frequencies for both selected frequency pairs. The dissimilar distributions at 12 Hz and
352 26 Hz exhibit a majority of acini (72.7 %) that are preferentially ventilated by only one
353 frequency or the other, whereas the similar distributions at 0.3 Hz and 12 Hz exhibit only a
354 minority of acini (17.3 %) with the same complementary behavior.

355 Figure 7 shows the required eucapnic flow scaling for dual-frequency waveforms
356 constructed from various linear combinations of each frequency in the selected frequency pairs,
357 according to Equation (17). For all values of β , values of Ψ_{euc} were iteratively adjusted to
358 achieve total CO₂ elimination within 0.3 % error of the predicted metabolic CO₂ production of
359 $1.93 \cdot 10^{-3} \text{ L s}^{-1}$ for a 25 kg dog. Figure 8 shows the resulting distributions of acinar peak
360 volumetric strain ($\varepsilon_{V,n}$), and Figure 9 shows distributions of acinar root-mean-square volume
361 ($V_{\text{RMS},n}$). Comparing distributed ventilation using oscillations at only a single frequency (i.e., at
362 $\beta = 0$ or $\beta = 1$ only), 0.3 Hz ventilation produced the least heterogeneity in both strain and
363 V_{RMS} , but also the largest magnitudes of strain, compared to either 12 Hz or 26 Hz. For example,

364 the range of $\varepsilon_{V,n}$, reported as median (minimum, maximum), was 15.5 % (12.3 %, 19.4 %)
365 during single-frequency ventilation at 0.3 Hz, compared to 2.8 % (6.5 %, 2.1 %) at 12 Hz or 1.6
366 % (0.5 %, 3.4 %) at 26 Hz. For the dual-frequency waveforms constructed using 0.3 Hz and 12
367 Hz, no improvement in ventilation heterogeneity was observed for any linear combination of the
368 two frequencies, compared to either single frequency alone (i.e., $0 < \beta < 1$ compared to $\beta = 0$
369 or $\beta = 1$). However for waveforms using 12 Hz and 26 Hz oscillations, an optimal value of
370 $\beta = 0.4$ was found to provide the greatest reduction in the difference between the maximum and
371 minimum values of normalized acinar strain and V_{RMS} . Specifically at $\beta = 0.4$, the range of
372 normalized strain was reduced by 50.8 % compared to 26 Hz ($\beta = 0$) and 37.2 % compared to
373 12 Hz ($\beta = 1$).

374

375 **DISCUSSION**

376 In this study, we extended an existing computational model of distributed flow and gas
377 transport (13) to simulate ventilation heterogeneity during oscillatory ventilation with either a
378 single frequency or two frequencies delivered simultaneously. By choosing pairs of frequencies
379 with complementary ventilation distributions, we demonstrated that regional underventilation at
380 one frequency may be compensated by regional overventilation at the other frequency. Thus, an
381 ‘optimal’ linear combination of two frequencies can be identified that yields the least amount of
382 parenchymal strain heterogeneity compared to either single frequency alone (Figures 8B and 9B).
383 However, for a pair of oscillatory frequencies yielding similar ventilation distributions, no linear
384 combination was found to reduce ventilation heterogeneity (Figures 8A and 9A). This finding
385 suggests that it is possible to optimize the spectral content of oscillatory waveforms to achieve
386 substantial reductions in ventilation heterogeneity and parenchymal strain.

387 In these simulations of eucapnic oscillatory ventilation in a canine lung, low frequencies
388 produced the lowest degree of ventilation heterogeneity, yet the largest magnitudes of regional
389 strain. However, increasing oscillatory frequency resulted in reduced regional strain but
390 increased strain heterogeneity, especially for frequencies greater than the resonant frequency of
391 this model, $f_{\text{res}} = 7.5 \text{ Hz}$ (13). The resonant frequency indicates the transition from flows
392 dominated by elastic forces ($f < f_{\text{res}}$) to flows dominated by inertial forces ($f > f_{\text{res}}$) (4, 6).
393 Thus high-frequency oscillatory ventilation (HFOV) may reduce parenchymal strain, yet
394 increase both strain rate and strain heterogeneity compared to conventional mechanical
395 ventilation (20, 25, 26). This trade-off may in part explain the nonsuperiority of HFOV over
396 conventional mechanical ventilation in patients with mechanically heterogeneous lungs (8, 22,
397 38).

398 Our computational model highlights a means by which both parenchymal strain and
399 strain heterogeneity may be minimized. If multiple frequencies are delivered simultaneously, the
400 respective contributions of each frequency to the combined distribution of parenchymal strain
401 may be tuned towards a particular objective, e.g., minimizing strain heterogeneity. By extending
402 this concept of dual-frequency oscillation to the more general case of three or more frequencies
403 (16), one may further exploit frequency-dependent ventilation distribution to mitigate adverse
404 consequences of parenchymal strain heterogeneity. This proposed mechanism of benefit may in
405 part explain improvements in oxygenation and gas exchange reported during experimental use of
406 multi-frequency oscillatory ventilation (MFOV) in surfactant-deficient preterm lungs (16).
407 These findings are also relevant to high-frequency percussive ventilation (HFPV), which
408 involves high frequency oscillations superimposed on conventional mechanical ventilation
409 waveforms (1, 7, 28). Large reductions in parenchymal strain at lower frequencies may be
410 achieved during HFPV by supplementary gas transport using a relatively small contribution of
411 superimposed high frequency oscillation.

412 Two criteria were proposed to evaluate candidate frequency pairs in this study: the
413 ventilation distribution similarity ($\mathcal{S}_{\dot{V}}$) and the correlation coefficient (r). As shown in Figure 4,
414 $\mathcal{S}_{\dot{V}}$ and r demonstrate close agreement with each other over the range of frequencies from 0.1 Hz
415 to 30 Hz, suggesting that the outcome of candidate frequency pair selection may not be specific
416 to the particular criterion used for evaluation.

417 Although peak acinar volumetric strain and specific ventilation are typically used to
418 assess regional ventilation heterogeneity during tidal breathing (2, 27), these metrics may not be
419 directly applicable during oscillation with two or more frequencies, since the corresponding
420 regional volume fluctuations will not oscillate between a consistent minimum and maximum.

421 Rather, parenchymal strain may exhibit various local minima and maxima. Thus ventilation
422 heterogeneity during multi-frequency oscillation may be more appropriately characterized by the
423 root-mean-square of regional volume fluctuations (V_{RMS}) (16). V_{RMS} describes the variance of
424 regional distension about a mean lung volume, which is proportional to volume amplitude during
425 single-frequency oscillatory ventilation, yet also accounts for oscillation at multiple distinct
426 frequencies. In Figures 8 and 9 the distributions of peak acinar volumetric strain ($\varepsilon_{V,n}$) and
427 $V_{\text{RMS},n}$ exhibited close agreement, suggesting that the analysis of ventilation heterogeneity is not
428 sensitive to the choice of either metric.

429 Limitations

430 The modeling assumptions and validation for the single-frequency gas transport model
431 have been presented in our previous study (13). Additional comparison to distributed strain
432 measured on the pleural surface of excised canine lungs is provided in Appendix A-2. Our
433 currently proposed extension to accommodate two frequencies of oscillations simultaneously has
434 been derived using a similar conceptual framework. However to our knowledge, no robust
435 experimental data is available to validate these model simulations. Specific or quantitative
436 predictions based on this model should therefore be treated with appropriate caution.
437 Particularly, our simulations assume that the mechanical behavior of the lung is linear and time-
438 invariant. Thus superposition of two sinusoidal oscillations at the airway opening results in a
439 simple linear combination of the respective flow distributions at each frequency. However,
440 nonlinear mechanical properties of an actual mammalian lung may lead to unpredictable
441 distortion and interaction of superimposed oscillations (32, 33, 39). Experimental imaging
442 techniques such as frequency-selective computed tomography (12) or optical coherence

443 tomography (24) may be used to further assess the extent of nonlinear mechanical behavior
444 during multi-frequency oscillation *in situ*.

445 This particular analysis of simulated multi-frequency oscillation examined only two
446 specific pairs of frequencies, to establish the feasibility of using a multi-frequency approach to
447 reduce parenchymal strain heterogeneity compared to single-frequency oscillation in a
448 computational model. Furthermore the simulations were performed using a model of healthy
449 canine lungs, with all mechanical heterogeneity derived only from gravitational gradients in
450 transpulmonary pressure and airway network asymmetries. Nonetheless this healthy model
451 exhibited substantial ventilation heterogeneity at high frequencies (10, 20), indicating that
452 exploiting frequency-dependent ventilation heterogeneity may be possible even within lungs
453 with homogeneous tissue compliance. The particular distribution of regional strain may be
454 appreciably altered under injured conditions (13), yet the rationale for applying a multi-
455 frequency approach remains the same (16). The results of these simulations warrant further
456 investigation, involving optimization of the spectral content in oscillatory waveforms, or using a
457 larger number of distinct frequencies. Such an optimization procedure may involve an
458 evaluation of the ventilation distribution similarity, similar to that presented in Figure 4.
459 However the prospect of translating these computational modeling results into a practical *in vivo*
460 approach for identification of optimal frequencies presents several considerable technical
461 challenges, not the least of which is non-invasive quantification of frequency-dependent
462 ventilation heterogeneity (10, 27).

463

464 **CONCLUSION**

465 Although high frequency oscillatory ventilation achieves CO₂ elimination with reduced
466 parenchymal strain compared to conventional mechanical ventilation, increased strain
467 heterogeneity during HFOV may be injurious to the lung. Heterogeneity of regional mechanical
468 properties and airway network asymmetry result in frequency-dependent distributions of
469 oscillatory flow, especially at high frequencies. Such frequency-dependent heterogeneity in
470 ventilation may be exploited by combining multiple simultaneous frequencies of oscillation.
471 Dual-frequency oscillatory ventilation may provide more uniform ventilation throughout the
472 heterogeneous lung, such that regional maldistribution of parenchymal strain can be minimized
473 by using oscillatory frequencies with dissimilar ventilation distributions. This unique oscillatory
474 modality may thus have utility for the treatment of patients with heterogeneous lung injury, by
475 minimizing the extremes of cyclic parenchymal strain and reducing the risk of ventilator-induced
476 lung injury.

477

478 **ACKNOWLEDGMENTS**

479 Portions of this work were excerpted from Master of Science thesis “Simulation of Ventilation
480 Distribution and Gas Transport During Oscillatory Ventilation” by Jacob Herrmann, Boston
481 University, 2015. The authors thank Drs. Bela Suki, Brett Simon, J. Jane Pillow, and Joseph
482 Tien for their many helpful suggestions during the course of this work.

483

484 **GRANTS**

485 This work was supported in part by the Medical Technologies Centre of Research Excellence at
486 the University of Auckland (M. H. Tawhai), National Institutes of Health Grants UM1
487 HL108724, R01 HL112986, and R01 HL126383 (D. W. Kaczka), and the University of Iowa,
488 Department of Anesthesia (D. W. Kaczka, J. Herrmann), and by the Office of the Assistant
489 Secretary of Defense for Health Affairs, through the Peer Reviewed Medical Research Program
490 under Award No. W81XWH-16-1-0434 (D. W. Kaczka). Opinions, interpretations, conclusions
491 and recommendations are those of the authors and are not necessarily endorsed by the U.S.
492 Department of Defense.

493

494 **DISCLOSURES**

495 D. W. Kaczka and J. Herrmann are co-inventors on a pending patent involving multi-frequency
496 oscillatory ventilation (MFOV). In addition, they are co-founders and shareholders of
497 OscillaVent, Inc.

498

499 **AUTHOR CONTRIBUTIONS**

500 J.H., M.H.T., and D.W.K. conception and design of research; J.H. and M.H.T. performed
501 experiments; J.H., M.H.T., and D.W.K. analyzed data; J.H., M.H.T., and D.W.K. interpreted
502 results of experiments; J.H. and D.W.K. prepared figures; J.H. and D.W.K. drafted manuscript;
503 J.H., M.H.T., and D.W.K. edited and revised manuscript; J.H., M.H.T., and D.W.K. approved
504 final version of manuscript.

505

506

507 **FIGURE LEGENDS**

508 Figure 1. Illustration of method for computing V_{mix} during ventilation with multiple frequencies
509 of oscillation. In this example, two frequencies are used—3 Hz and 7 Hz—such that $f_0 = 1$ Hz.
510 The shading indicates where the conditions of $\dot{V}(t) > 0$ (light and dark) and $V(t) > V_{\text{seg}}$ (dark)
511 are satisfied. V_{mix} can be calculated from the sum of flow integrals indicated by dark shading for
512 which both conditions are satisfied. Equivalently, V_{mix} can be calculated from the sum of the
513 lengths of the dark lines denoting the local maxima of $V(t) - V_{\text{seg}}$.

514 Figure 2. Airway segments and acini labeled according to gas transport mechanisms. (A)
515 Decision trees used for labeling airway segments according to the dominant gas transport
516 mechanism contributing to the overall rate of gas transport within each individual airway. Acini
517 are labeled if fresh gas is advected via bulk flow directly into the acinar space. (B) Airways and
518 acini colored according to gas transport mechanisms during eucapnic ventilation at various
519 frequencies using the tidal volumes indicated in mL. Acini that do not receive fresh gas
520 ventilation are not shown. Gravitational direction (g) is indicated for a supine orientation.

521 Figure 3. Two examples of ventilation distribution similarity ($\mathcal{S}_{\dot{V}}$) and correlation coefficient (r)
522 in a schematic lung with three mechanically heterogeneous compartments. The frequency-
523 dependent fraction of oscillatory flow received by each compartment is indicated for two
524 frequencies f_1 and f_2 . In the case of similar distributions (A), the central compartment receives
525 the greatest proportion of oscillatory flow at both frequencies, and the corresponding value of $\mathcal{S}_{\dot{V}}$
526 is close to unity whereas r is close to +1. In the case of dissimilar distributions (B), the
527 compartments underventilated at f_1 are overventilated at f_2 , and vice versa—thus the value of $\mathcal{S}_{\dot{V}}$
528 is close to zero and r is close to -1. See text for definitions of $\mathcal{S}_{\dot{V}}$ and r .

529 Figure 4. Contours of (A) ventilation distribution similarity ($\mathcal{S}_{\dot{V}}$), and (B) correlation coefficient
530 (r), in the canine lung model for pairs of frequencies between 0.1 and 40 Hz. The line of identity
531 (dotted line) represents comparisons between each frequency and itself, such that $\mathcal{S}_{\dot{V}}(f_1, f_1) = 1$
532 and $r(f_1, f_1) = +1$. The contours of $\mathcal{S}_{\dot{V}}$ are symmetric about the line of identity, such that
533 $\mathcal{S}_{\dot{V}}(f_1, f_2) = \mathcal{S}_{\dot{V}}(f_2, f_1)$ and $r(f_1, f_2) = r(f_2, f_1)$. Labeled points correspond to frequency pairs
534 selected for further examination: 12 Hz and 26 Hz (circle), 0.3 Hz and 12 Hz (triangle). See text
535 for definitions of $\mathcal{S}_{\dot{V}}$ and r .

536 Figure 5. Acini labeled according to relative share of delivered oscillatory flow during 0.3 Hz,
537 12 Hz, and 26 Hz ventilation. Acinar flow is normalized by the flow amplitude delivered at the
538 trachea divided by the total number of acini, such that values above or below 1 represent acini
539 receiving more (red) or less (blue) than their respective shares of uniformly distributed flow,
540 respectively. Note that color bars are scaled differently for each frequency to emphasize the
541 regional distributions of relative over- and under-ventilation. Various view angles are provided,
542 with gravitational direction (g) indicated for a supine orientation (directed downwards, out of the
543 page, or upwards).

544 Figure 6. Scatter plots comparing normalized acinar flow distributions at two frequencies, where
545 each point represents a single acinus, and horizontal or vertical position correspond to
546 normalized flow amplitude in each acinus at either frequency. Two examples are shown: (A)
547 similar distributions at 0.3 Hz vs. 12 Hz with $\mathcal{S}_{\dot{V}} = 0.98$ and $r = +0.69$ (left), and (B) dissimilar
548 distributions at 12 Hz vs. 26 Hz with $\mathcal{S}_{\dot{V}} = 0.85$ and $r = -0.64$ (right). The four quadrants
549 delineate acini that receive either above-average (i.e., greater than 1.0) or below-average (i.e.,
550 less than 1.0) amounts of oscillatory flow at one or both frequencies.

551 Figure 7. Eucapnic flow scaling (Ψ_{euc}) for dual-frequency waveforms constructed according to
552 Equation (17) using $0 \leq \beta \leq 1$ to scale the contribution of each frequency, using oscillations at
553 either 0.3 Hz and 12 Hz (A), or 12 Hz and 26 Hz (B). Each point represents a single simulation.
554 Corresponding volume waveforms at the airway opening are shown for each frequency pair at
555 select values of β .

556 Figure 8. Distributions of acinar peak volumetric strain (ε_V) for dual-frequency waveforms
557 constructed according to Equation (17) using $0 \leq \beta \leq 1$ to scale the contribution of each
558 frequency, using oscillations at either 0.3 Hz and 12 Hz (A), or 12 Hz and 26 Hz (B).
559 Distributions are represented by the median (solid line) and full range between minimum and
560 maximum value (shaded region). Normalized distributions are shown with the mean value
561 normalized to unity (dotted line).

562 Figure 9. Distributions of acinar root-mean-square volume (V_{RMS}) for dual-frequency waveforms
563 constructed according to Equation (17) using $0 \leq \beta \leq 1$ to scale the contribution of each
564 frequency, using oscillations at either 0.3 Hz and 12 Hz (A), or 12 Hz and 26 Hz (B).
565 Distributions are represented by the median (solid line) and full range between minimum and
566 maximum value (shaded region). Normalized distributions are shown with the mean value
567 normalized to unity (dotted line).

568 Figure A-1. Comparison between experimental and simulated acinar area strains. Experimental
569 data for pleural surface area strain reported by Lehr et al. (20) is indicated by mean (black
570 circles) and standard deviation (error bars) at 1 Hz, 15 Hz, and 30 Hz. Equivalent area strain for
571 our model assuming isotropic deformation during simulated ventilation is shown as mean
572 (dashed grey line) and standard deviation (solid grey lines). (A) Area strain amplitude is
573 reported during oscillation using a constant ratio of 7.6 % oscillatory volume amplitude relative
574 to total lung volume (see text for additional experimental details). (B) Area strain phase is
575 reported relative to volume phase measured at the airway opening.

576

577

578 APPENDIX

579

580 **A-1. Laminar Oscillatory Dispersion**

581 In this analysis of laminar oscillatory dispersion during flow with multiple simultaneous
 582 frequencies, we follow the reasoning and nomenclature of Watson (37). Consider multi-
 583 frequency oscillatory flow in a tube with velocity profile:

$$w(x, y, t) = \sum_{k=1}^K \Re\{F_k(x, y)e^{j\omega_k t}\}, \quad (\text{A-1})$$

584 where k denotes the angular oscillation frequencies $\omega_k = 2\pi f_k$ from 1 to K , j is the unit
 585 imaginary number, and $F_k = F_k(x, y)$ is velocity amplitude distribution over the cross-section in
 586 the x - y plane, which is periodic in time t . The operator $\Re\{\dots\}$ denotes the real part of the
 587 complex-valued argument within the brackets. The concentration profile of a contaminant
 588 species contained in the carrier gas will then be of the form (37):

$$\theta(x, y, z, t) = -\gamma z + \sum_{k=1}^K \Re\{\gamma G_k(x, y)e^{j\omega_k t}\}, \quad (\text{A-2})$$

589 where z is the axial direction, γ is a constant corresponding to a linear concentration gradient in
 590 the axial direction, and $G_k = G_k(x, y)$ is the modulated amplitude distribution over the cross-
 591 section in the x - y plane and is periodic in time t with angular frequency ω_k , such that the
 592 concentration amplitude distribution is given by γG_k . The rate of molar flux of the contaminant
 593 has advective and diffusive terms integrated over the cross-section S is given by (37):

$$\iint_S \left[w\theta - D_{\text{mol}} \frac{\partial \theta}{\partial z} \right] dx dy, \quad (\text{A-3})$$

which expands to:

$$\iint_S \left[\gamma D_{\text{mol}} + \frac{1}{2} \left\{ \sum_{k=1}^K (F_k e^{j\omega_k t} + F_k^* e^{-j\omega_k t}) \right\} \left(-\gamma z \right. \right. \\ \left. \left. + \frac{1}{2} \gamma \left\{ \sum_{k=1}^K (G_k e^{j\omega_k t} + G_k^* e^{-j\omega_k t}) \right\} \right) \right] dx dy, \quad (\text{A-4})$$

594 where the asterisks denote complex conjugates. The expansion of the product produces
 595 oscillatory terms (i.e. terms preceding $e^{j\omega_k t} e^{j\omega_k t} = e^{2j\omega_k t}$ or preceding $e^{j\omega_k t} e^{-j\omega_i t} =$
 596 $e^{j(\omega_k - \omega_i)t}$ with $i \neq k$) and steady terms (i.e. terms preceding $e^{j\omega_k t} e^{-j\omega_k t} = 1$). The mean rate
 597 of flux, averaged over time, is:

$$\iint_S \left[\gamma D_{\text{mol}} + \frac{1}{4} \gamma \left\{ \sum_{k=1}^K (F_k G_k^* + F_k^* G_k) \right\} \right] dx dy, \quad (\text{A-5})$$

598 wherein all oscillatory terms are reduced to zero in the time-averaging, and only the steady terms
 599 remain (37). The effective diffusivity is:

$$D_{\text{eff}} = D_{\text{mol}} (1 + R_D), \quad (\text{A-6})$$

600 where R_D is the relative increase in diffusivity compared to molecular diffusivity, given by:

$$R_D = -\frac{1}{4D_{\text{mol}} A_S} \iint_S \left[\sum_{k=1}^K (F_k G_k^* + F_k^* G_k) \right] dx dy, \quad (\text{A-7})$$

601 which rearranges to:

$$R_D = \sum_{k=1}^K \left(\frac{1}{4D_{\text{mol}} A_S} \iint_S [F_k G_k^* + F_k^* G_k] dx dy \right), \quad (\text{A-8})$$

602 where A_S is the area of the cross-section S , and the term inside the summation is identical to the
 603 relative increase in diffusivity for any individual frequency of oscillation (37). Thus the
 604 effective diffusivity is given by:

$$D_{\text{eff}} = D_{\text{mol}} + \sum_{k=1}^K D_{\text{dis}}^{\text{lam}}(f_k). \quad (\text{A-9})$$

605 Equation (A-9) relies on the reduction of time-averaged oscillatory terms to zero over a long
 606 period of oscillation, i.e., the elimination of $e^{2j\omega_k t}$ and $e^{j(\omega_k - \omega_i)t}$ terms in the transition from
 607 Equation (A-4) to Equation (A-5). Therefore, this model of dispersion during simultaneous
 608 multiple frequencies may not apply when the beat frequency (i.e., the difference between any
 609 two frequencies) is small.

610

611 **A-2. Comparison with Experimental Strain Measurements**

612 In our previous work (13), we demonstrated that the tidal volume required for eucapnic
 613 ventilation during single-frequency oscillatory ventilation was consistent with the experimental
 614 findings of Venegas et al. (36). The distribution of volumetric strain within lungs *in vivo* is
 615 difficult to quantify experimentally, especially during rapid motion such as during high-
 616 frequency oscillatory ventilation. Lehr et al. (20) used stroboscopic photography to capture
 617 time-varying motion of grid points marked on the pleural surface of an excised canine lung.
 618 They reported area strain measurements during oscillations at 1 Hz, 15 Hz, and 30 Hz. We may
 619 compare our simulated distributions of volumetric strain to the area strain distributions reported
 620 by Lehr et al. by first adjusting the simulated volume oscillations to achieve the same ratio of
 621 volume amplitude to total lung volume. Lehr et al. reported using 100 mL volume oscillations
 622 applied to a lung of total volume 1320 mL, expecting volumetric strains of approximately 7.6 %.
 623 Assuming isotropic expansion and contraction, they expected the corresponding area strains to
 624 be two-thirds of the volumetric strain, or approximately 5.1 %. Figure A-1 shows the mean and
 625 standard deviation of pleural surface area strain amplitudes and phases reported by Lehr et al., as

626 well as the equivalent acinar area strain amplitudes and phases computed from our simulations
627 (assuming isotropic deformation). Both acinar strain amplitude heterogeneity and phase
628 heterogeneity increase at high oscillation frequencies above resonant frequency (7.5 Hz in our
629 model). This trend is also consistent with increasing heterogeneity in alveolar pressure
630 amplitudes and phases measured by Fredberg et al. (10), although pressure measurements alone
631 cannot be used to infer volumetric strain.

632

633 **REFERENCES**

634

635 1. **Allan PF, Osborn EC, Chung KK, Wanek SM.** High-frequency percussive ventilation
636 revisited. *J Burn Care Res* 31: 510–520, 2010.

637 2. **Amelon R, Cao K, Ding K, Christensen GE, Reinhardt JM, Raghavan ML.** Three-
638 dimensional characterization of regional lung deformation. *J Biomech* 44: 2489–2495,
639 2011.

640 3. **Amini R, Herrmann J, Kaczka DW.** Intratidal overdistention and derecruitment in the
641 injured lung: A simulation study. *IEEE Trans Biomed Eng* 64: 681–689, 2017.

642 4. **Amini R, Kaczka DW.** Impact of ventilation frequency and parenchymal stiffness on
643 flow and pressure distribution in a canine lung model. *Ann Biomed Eng* 41: 2699–2711,
644 2013.

645 5. **Choi J, Xia G, Tawhai MH, Hoffman EA, Lin C-L.** Numerical study of high-frequency
646 oscillatory air flow and convective mixing in a CT-based human airway model. *Ann
647 Biomed Eng* 38: 3550–71, 2010.

648 6. **Colletti AA, Amini R, Kaczka DW.** Simulating ventilation distribution in heterogenous
649 lung injury using a binary tree data structure. *Comput Biol Med* 41: 936–945, 2011.

650 7. **Eastman A, Holland D, Higgins J, Smith B, Delagarza J, Olson C, Brakenridge S,
651 Foteh K, Friese R.** High-frequency percussive ventilation improves oxygenation in
652 trauma patients with acute respiratory distress syndrome: a retrospective review. *Am J
653 Surg* 192: 191–195, 2006.

654 8. **Ferguson ND, Cook DJ, Guyatt GH, Mehta S, Hand L, Austin P, Zhou Q, Matte A,
655 Walter SD, Lamontagne F, Granton JT, Arabi YM, Arroliga AC, Stewart TE,**

656 **Slutsky AS, Meade MO.** High-frequency oscillation in early acute respiratory distress
657 syndrome. *N Engl J Med* 368: 795–805, 2013.

658 9. **Fredberg JJ.** Augmented diffusion in the airways can support pulmonary gas exchange. *J
659 Appl Physiol* 49: 232–238, 1980.

660 10. **Fredberg JJ, Keefe DH, Glass GM, Castile RG, Frantz ID.** Alveolar pressure
661 nonhomogeneity during small-amplitude high-frequency oscillation. *J Appl Physiol* 57:
662 788–800, 1984.

663 11. **Gattinoni L, Tonetti T, Cressoni M, Cadringher P, Herrmann P, Moerer O, Protti A,
664 Gotti M, Chiurazzi C, Carlesso E, Chiumello D, Quintel M.** Ventilator-related causes
665 of lung injury: the mechanical power. *Intensive Care Med* 42: 1567–1575, 2016.

666 12. **Herrmann J, Hoffman EA, Kaczka DW.** Frequency-Selective Computed Tomography:
667 Applications During Periodic Thoracic Motion. *IEEE Trans Med Imaging* 62: 1–1, 2017.

668 13. **Herrmann J, Tawhai MH, Kaczka DW.** Regional gas transport in the heterogeneous
669 lung during oscillatory ventilation. *J Appl Physiol* 121: 1306–1318, 2016.

670 14. **Jan DL, Shapiro AH, Kamm RD.** Some features of oscillatory flow in a model
671 bifurcation. *J Appl Physiol* 67: 147–159, 1989.

672 15. **Kaczka DW, Barnas GM, Suki B, Lutchen KR.** Assessment of time-domain analyses
673 for estimation of low-frequency respiratory mechanical properties and impedance spectra.
674 *Ann Biomed Eng* 23: 135–151, 1995.

675 16. **Kaczka DW, Herrmann J, Zonneveld CEE, Tingay DG, Lavizzari A, Noble PB,
676 Pillow JJ.** Multifrequency oscillatory ventilation in the premature lung: effects on gas
677 exchange, mechanics, and ventilation distribution. *Anesthesiology* 123: 1394–1403, 2015.

678 17. **Kaczka DW, Massa CB, Simon BA.** Reliability of estimating stochastic lung tissue

679 heterogeneity from pulmonary impedance spectra: a forward-inverse modeling study. *Ann*
680 *Biomed Eng* 35: 1722–1738, 2007.

681 18. **Kaczka DW, Smallwood JL.** Constant-phase descriptions of canine lung, chest wall, and
682 total respiratory system viscoelasticity: effects of distending pressure. *Respir Physiol*
683 *Neurobiol* 183: 75–84, 2012.

684 19. **Lai-Fook SJ, Rodarte JR.** Pleural pressure distribution and its relationship to lung
685 volume and interstitial pressure. *J Appl Physiol* 70: 967–78, 1991.

686 20. **Lehr JL, Butler JP, Westerman PA, Zatz SL, Drazen JM.** Photographic measurement
687 of pleural surface motion during lung oscillation. *J Appl Physiol* 59: 623–33, 1985.

688 21. **Loring SH, O'Donnell CR, Behazin N, Malhotra A, Sarge T, Ritz R, Novack V,
689 Talmor DS.** Esophageal pressures in acute lung injury: do they represent artifact or useful
690 information about transpulmonary pressure, chest wall mechanics, and lung stress? *J Appl*
691 *Physiol* 108: 515–522, 2010.

692 22. **Maitra S, Bhattacharjee S, Khanna P, Baidya DK.** High-frequency ventilation does not
693 provide mortality benefit in comparison with conventional lung-protective ventilation in
694 acute respiratory distress syndrome: A meta-analysis of the randomized controlled trials.
695 *Anesthesiology* 122: 1–11, 2014.

696 23. **Meade MO, Young D, Hanna S, Zhou Q, Bachman TE, Bollen C, Slutsky AS, Lamb
697 SE, Adhikari NKJ, Mentzelopoulos SD, Cook DJ, Sud S, Brower RG, Thompson BT,
698 Shah S, Stenzler A, Guyatt G, Ferguson ND.** Severity of hypoxemia and effect of high-
699 frequency oscillatory ventilation in acute respiratory distress syndrome. *Am J Respir Crit
700 Care Med* 196: 727–733, 2017.

701 24. **Mertens M, Tabuchi A, Meissner S, Krueger A, Schirrmann K, Kertscher U, Pries**

702 **AR, Slutsky AS, Koch E, Kuebler WM.** Alveolar dynamics in acute lung injury:
703 Heterogeneous distension rather than cyclic opening and collapse. *Crit Care Med* 37:
704 2604–2611, 2009.

705 25. **Mulreany DG, Simon BA, Murphy KJ, Easley RB.** Volumetric xenon-CT imaging of
706 conventional and high-frequency oscillatory ventilation. *Acad Radiol* 16: 718–725, 2009.

707 26. **Protti A, Maraffi T, Milesi M, Votta E, Santini A, Pugni P, Andreis DT, Nicosia F,
708 Zannin E, Gatti S, Vaira V, Ferrero S, Gattinoni L.** Role of strain rate in the
709 pathogenesis of ventilator-induced lung edema. *Crit Care Med* 44: e838–e845, 2016.

710 27. **Reinhardt JM, Ding K, Cao K, Christensen GE, Hoffman EA, Bodas S V.**
711 Registration-based estimates of local lung tissue expansion compared to xenon CT
712 measures of specific ventilation. *Med Image Anal* 12: 752–763, 2008.

713 28. **Rizkalla NA, Dominick CL, Fitzgerald JC, Thomas NJ, Yehya N.** High-frequency
714 percussive ventilation improves oxygenation and ventilation in pediatric patients with
715 acute respiratory failure. *J Crit Care* 29: 314.e1-314.e7, 2014.

716 29. **Scherer PW, Shendelman LH, Greene NM, Bouhuys A.** Measurement of axial
717 diffusivities in a model of the bronchial airways. *J Appl Physiol* 38: 719–723, 1975.

718 30. **Slutsky AS, Drazen JM, Ingram RH, Kamm RD, Shapiro AH, Fredberg JJ, Loring
719 SH, Lehr JL.** Effective pulmonary ventilation with small-volume oscillations at high
720 frequency. *Science* 209: 609–71, 1980.

721 31. **Slutsky AS, Kamm RD, Rossing TH, Loring SH, Lehr JL, Shapiro AH, Ingram RH,
722 Drazen JM.** Effects of frequency, tidal volume, and lung volume on CO₂ elimination in
723 dogs by high frequency (2-30 Hz), low tidal volume ventilation. *J Clin Invest* 68: 1475–
724 1484, 1981.

725 32. **Suki B, Bates JHT.** A nonlinear viscoelastic model of lung tissue mechanics. *J Appl*
726 *Physiol* 71: 826–833, 1991.

727 33. **Suki B, Hantos Z, Daróczy B, Alkaysi G, Nagy S.** Nonlinearity and harmonic distortion
728 of dog lungs measured by low-frequency forced oscillations. *J Appl Physiol* 71: 69–75,
729 1991.

730 34. **Tawhai MH, Hunter PJ, Tschirren J, Reinhardt JM, McLennan G, Hoffman EA.**
731 CT-based geometry analysis and finite element models of the human and ovine bronchial
732 tree. *J Appl Physiol* 97: 2310–2321, 2004.

733 35. **Taylor G.** The Dispersion of Matter in Turbulent Flow through a Pipe. *Proc R Soc A*
734 *Math Phys Eng Sci* 223: 446–468, 1954.

735 36. **Venegas JG, Hales CA, Strieder DJ.** A general dimensionless equation of gas transport
736 by high-frequency ventilation. *J Appl Physiol* 60: 1025–30, 1986.

737 37. **Watson EJ.** Diffusion in oscillatory pipe flow. *J Fluid Mech* 133: 233–244, 1983.

738 38. **Young D, Lamb SE, Shah S, MacKenzie I, Tunnicliffe W, Lall R, Rowan K,**
739 **Cuthbertson BH.** High-frequency oscillation for acute respiratory distress syndrome. *N*
740 *Engl J Med* 368: 806–813, 2013.

741 39. **Zhang Q, Suki B, Lutchen KR.** Harmonic distortion from nonlinear systems with
742 broadband inputs: applications to lung mechanics. *Ann Biomed Eng* 23: 672–681, 1995.

743

744

Figure 1

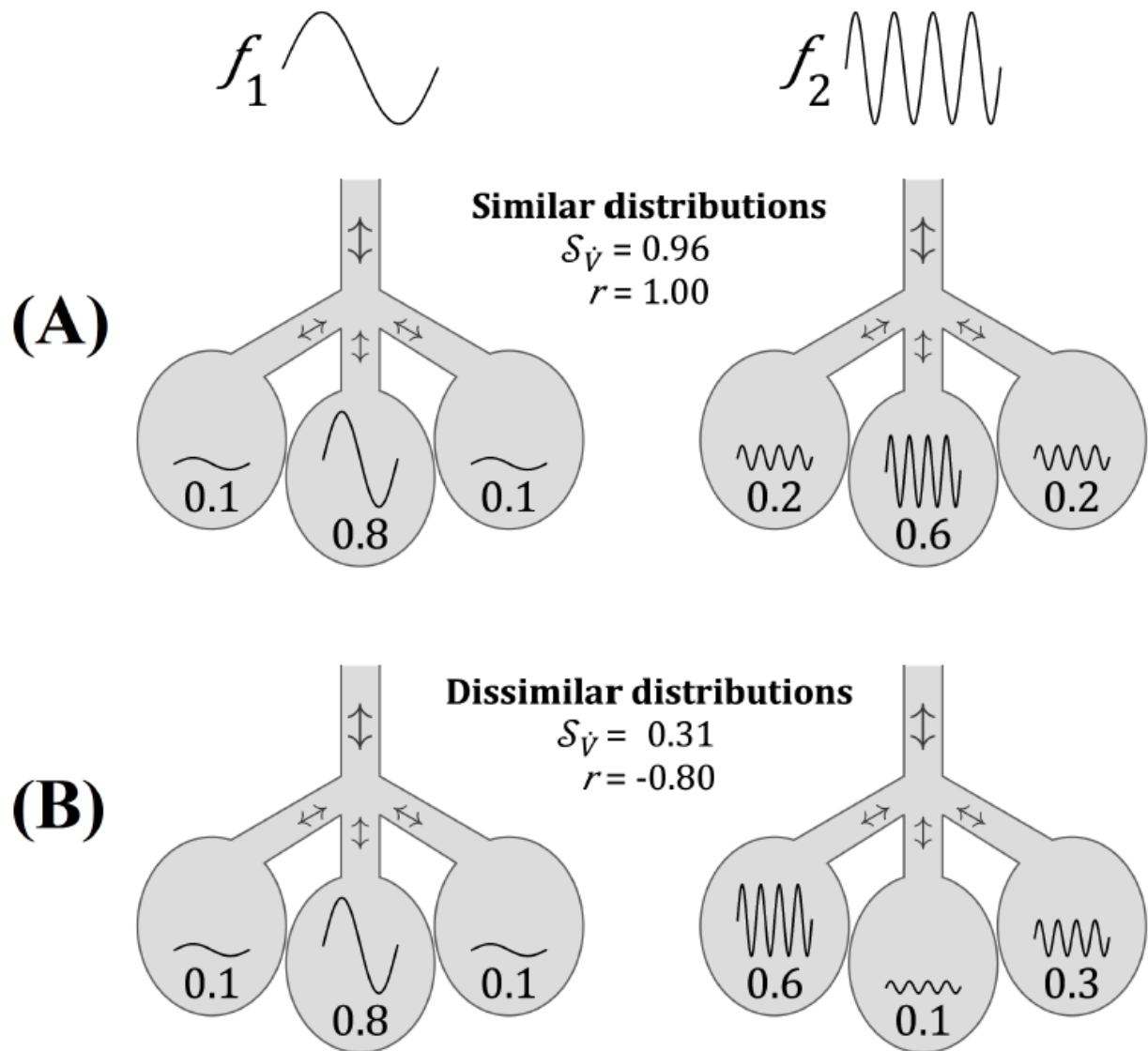


Figure 2 Dominant Gas Transport Mechanism in Individual Airway Segments

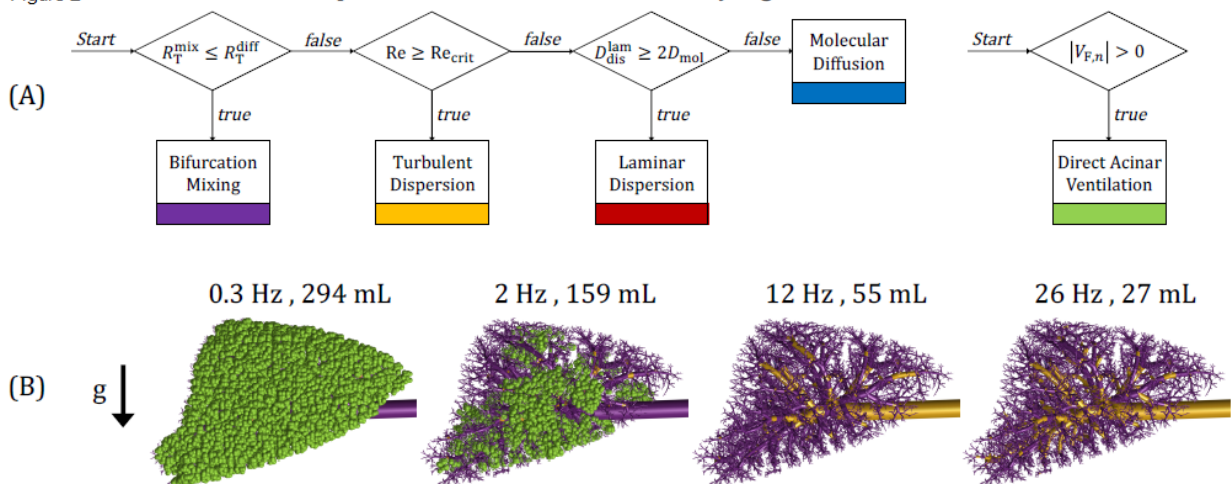


Figure 3

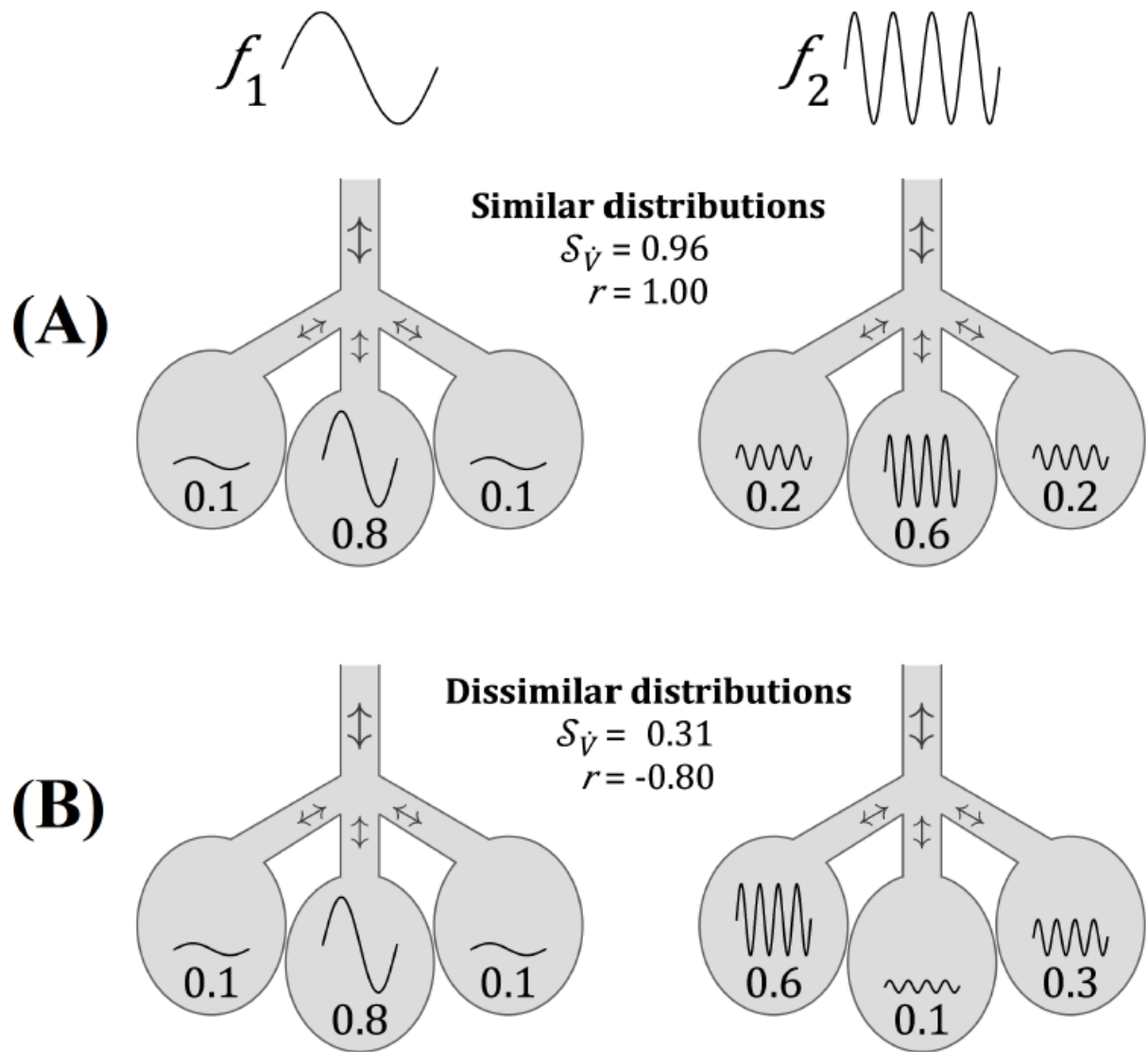


Figure 4 Ventilation Distribution Similarity Index ($S_{\dot{V}}$)

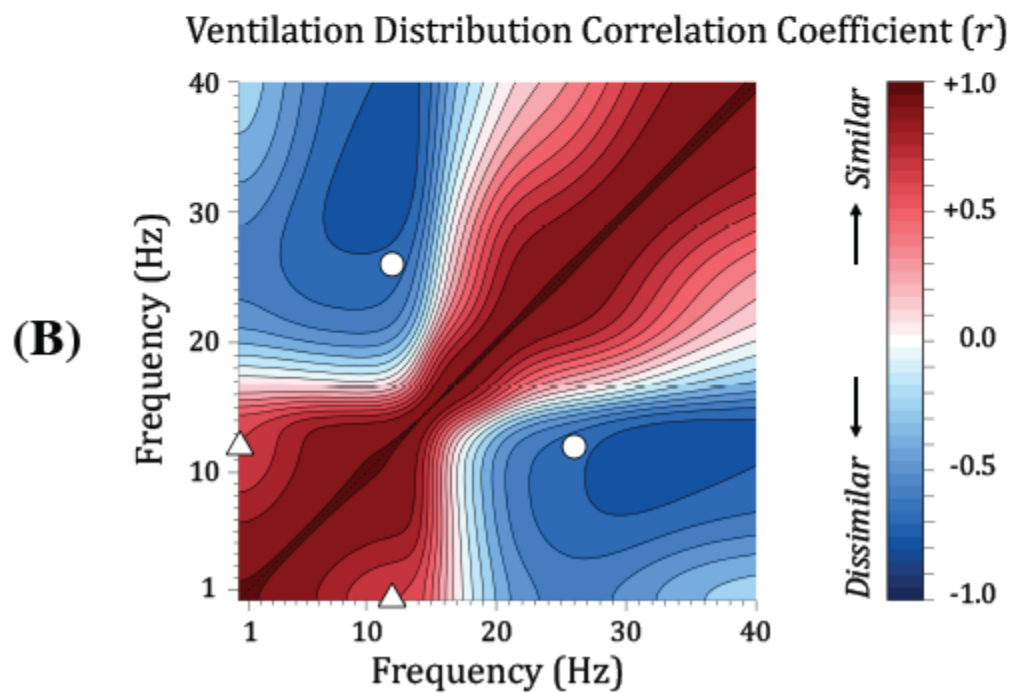
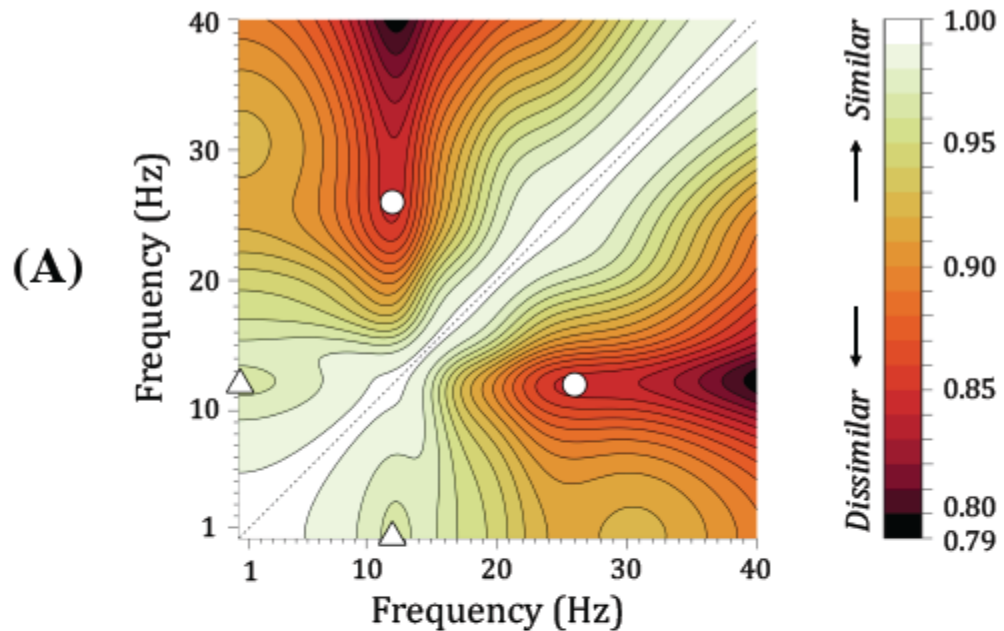


Figure 5

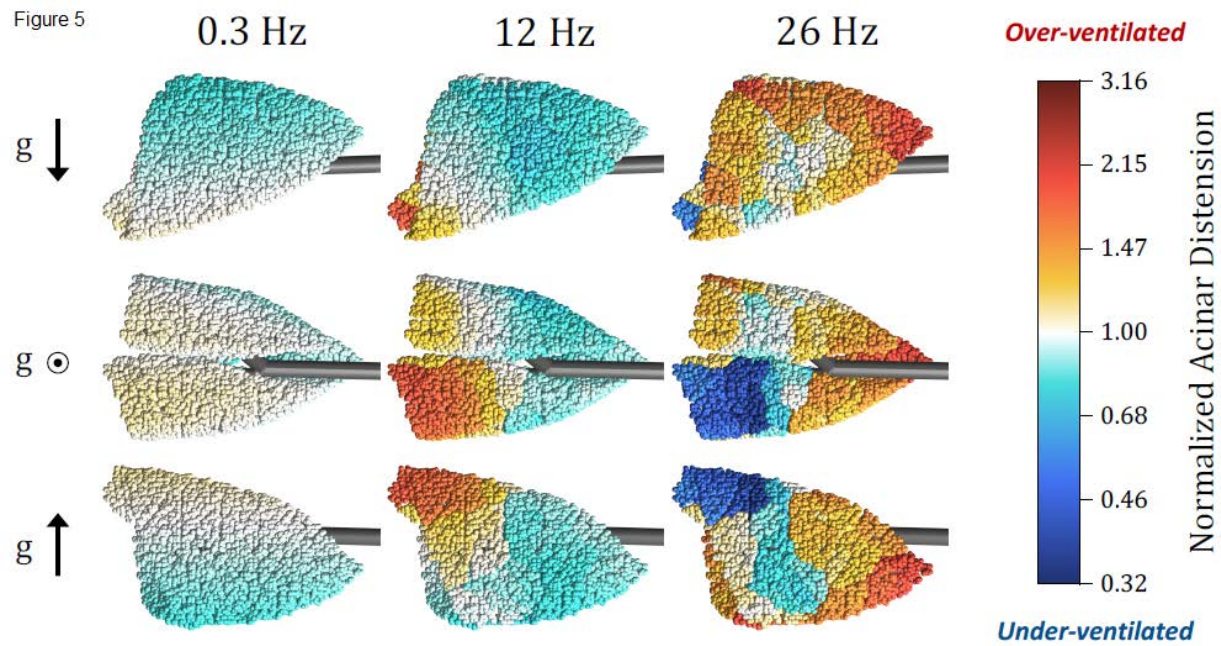


Figure 6

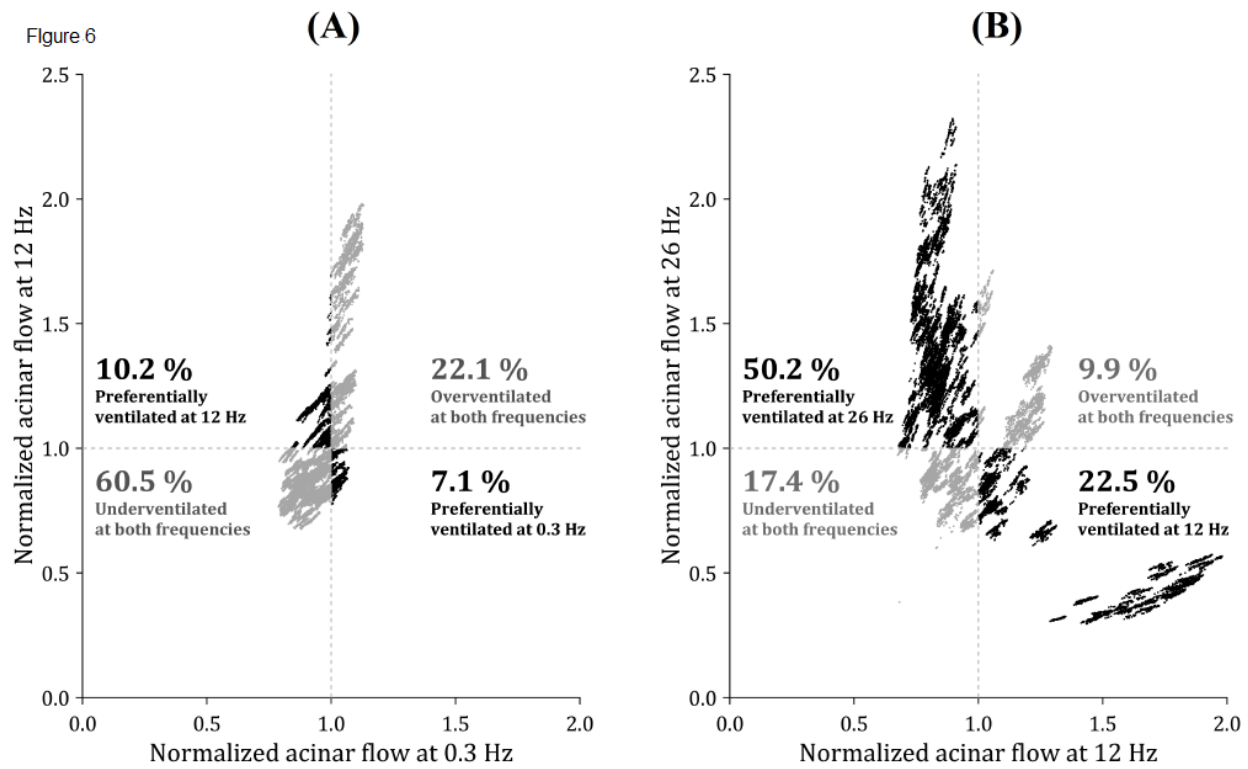


Figure 7

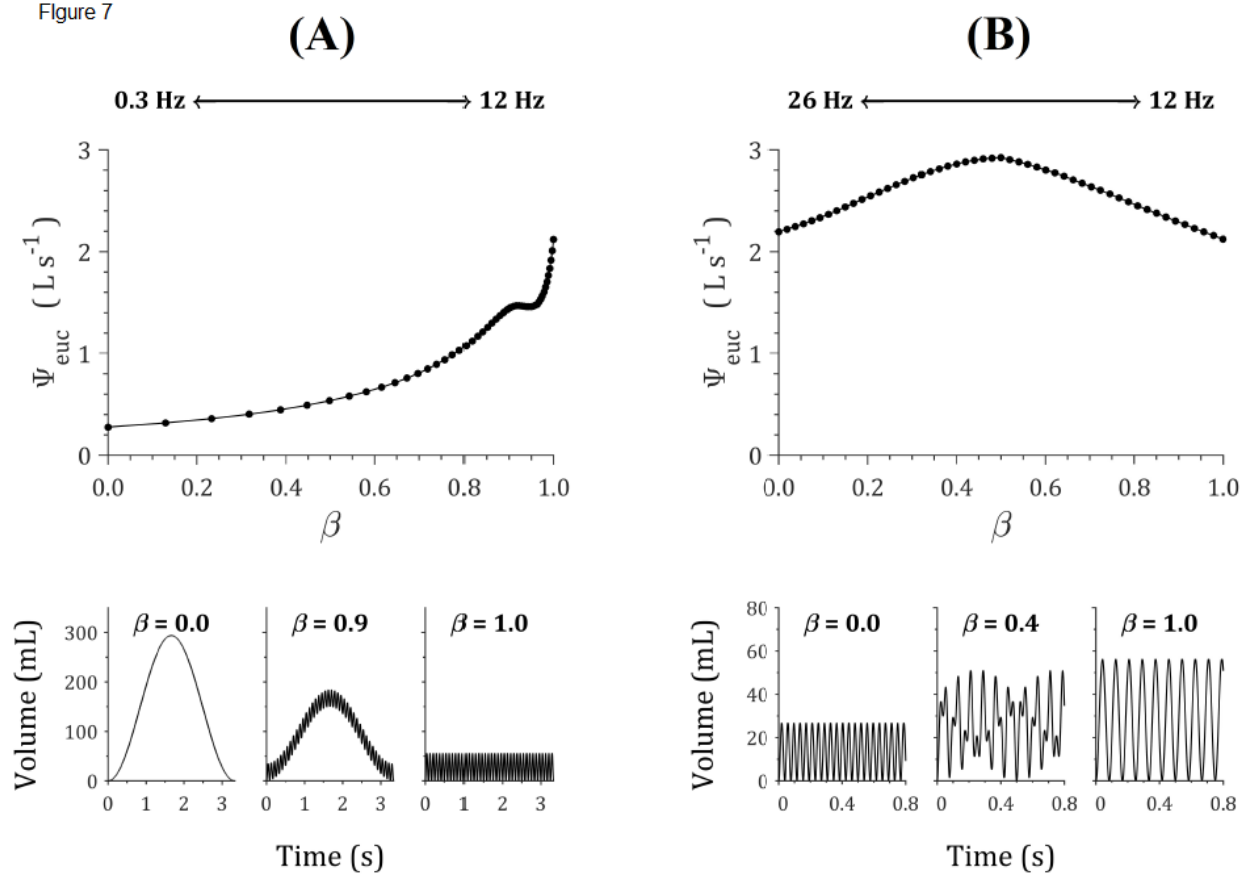


Figure 8

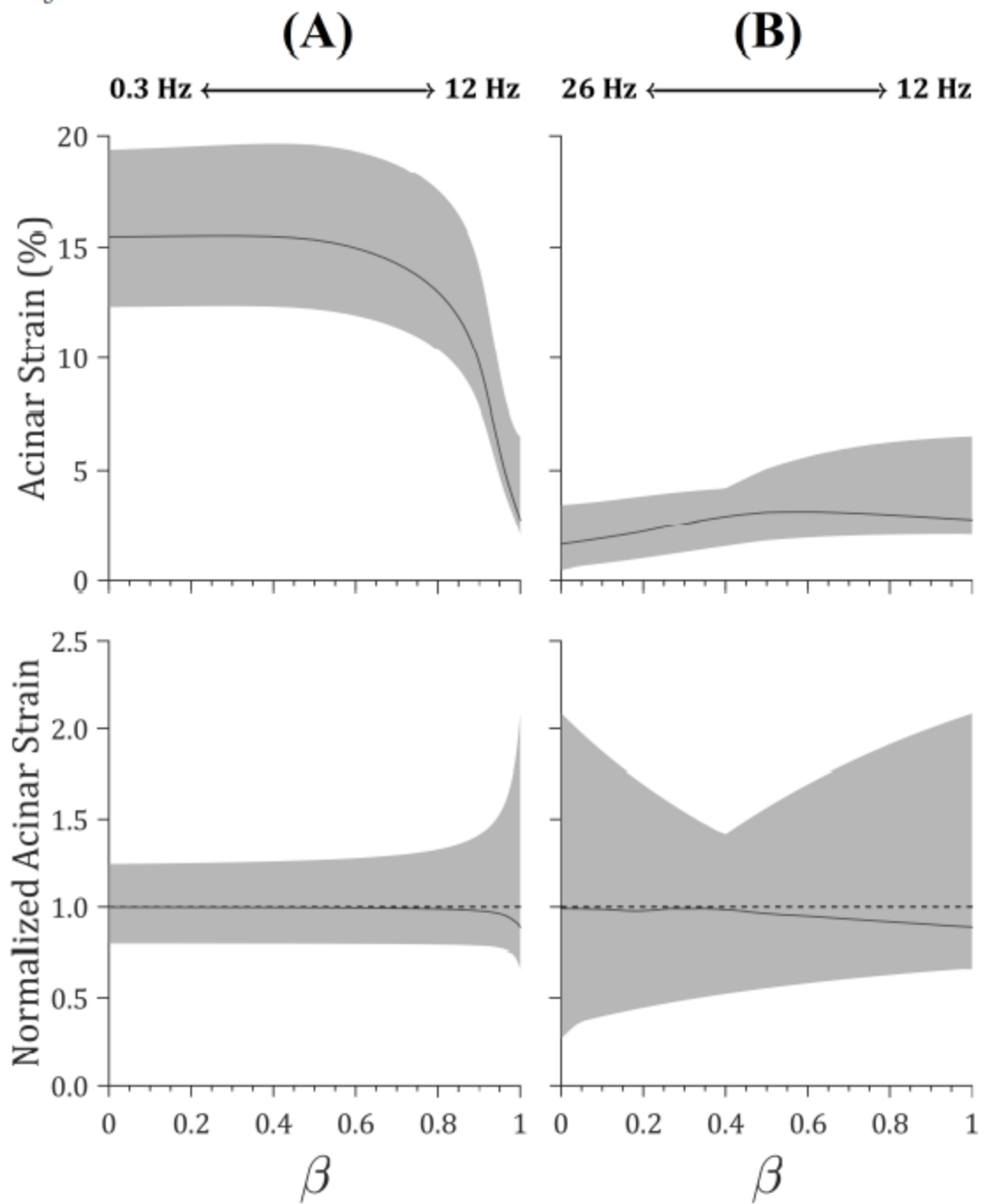
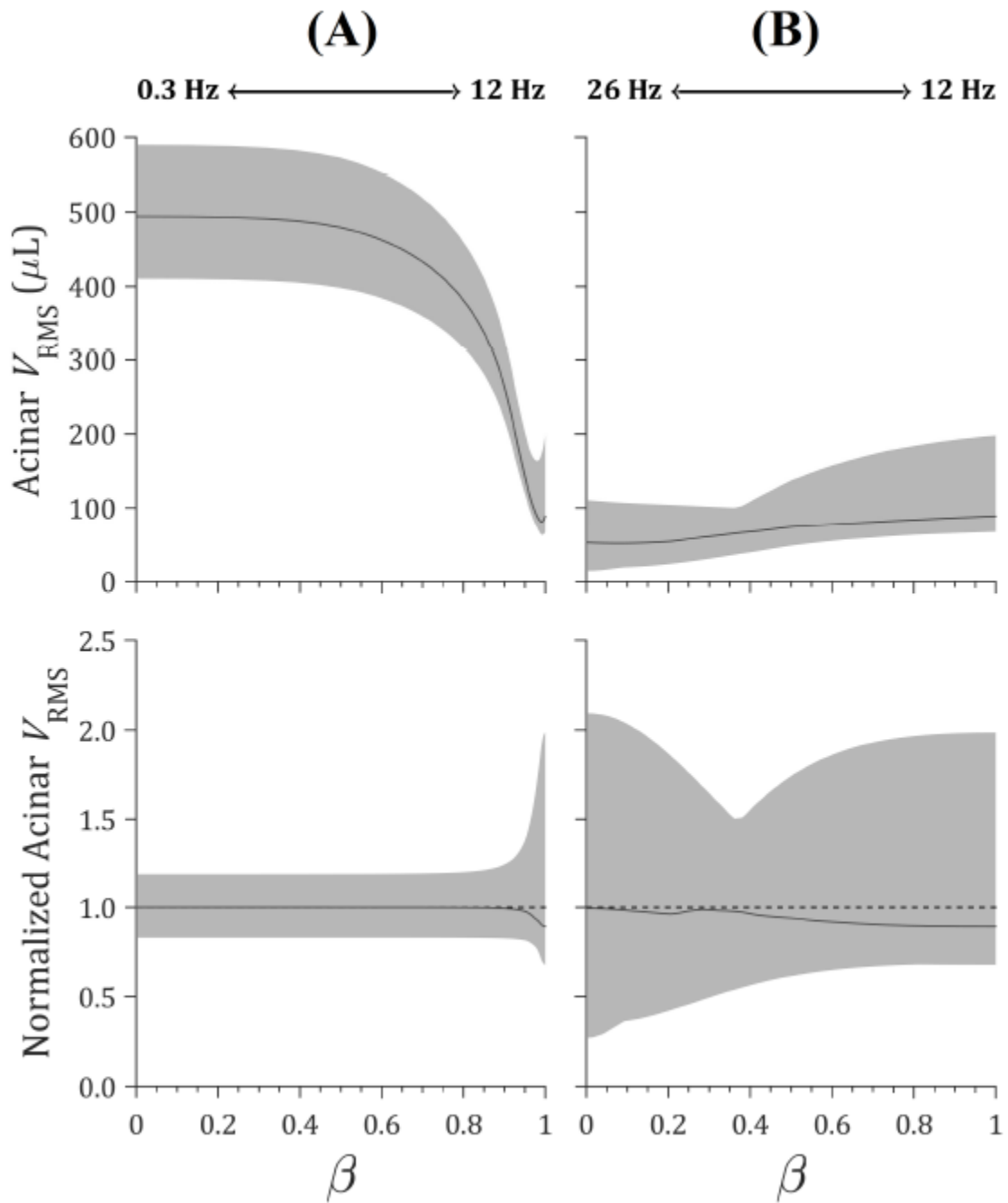
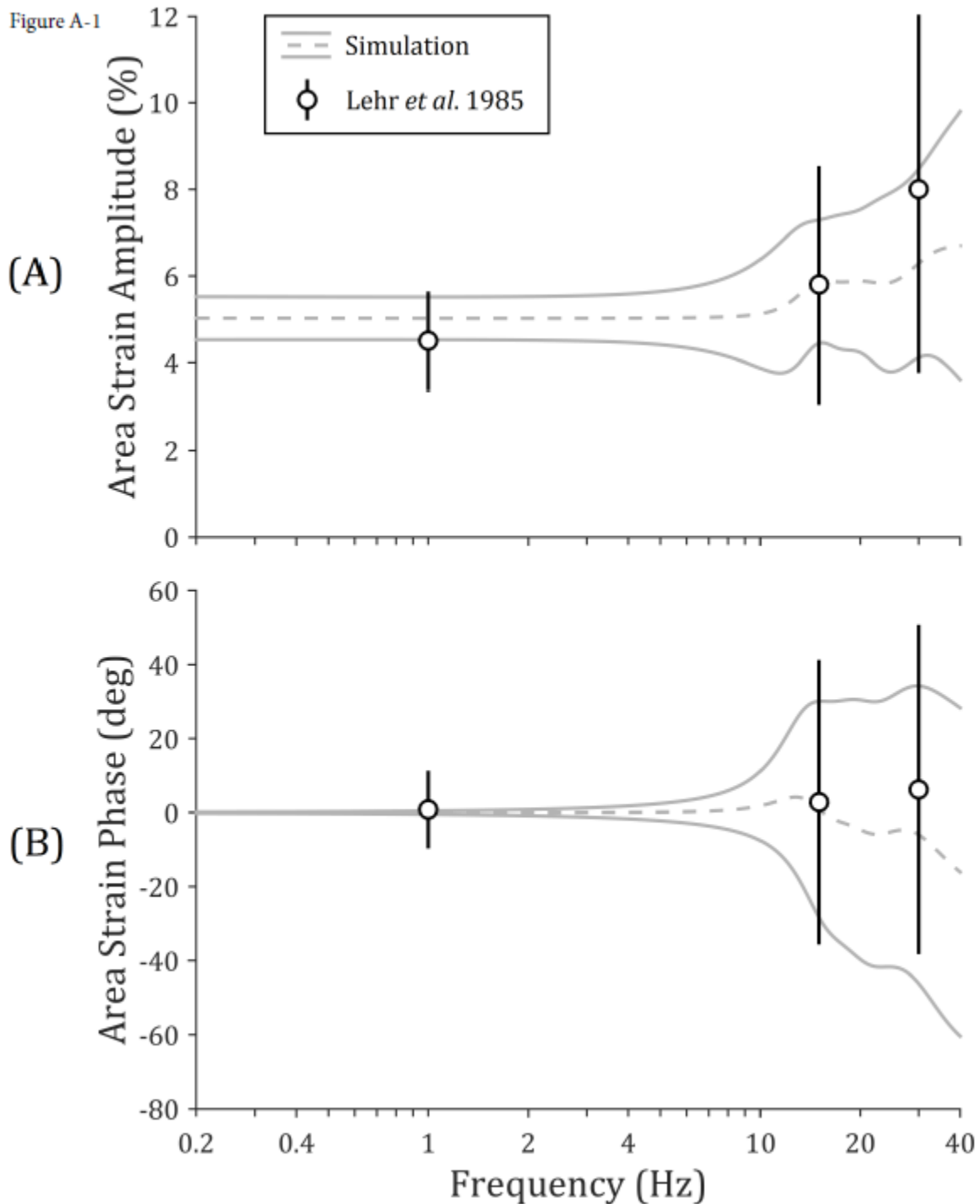


Figure 9





Regional gas transport in the heterogeneous lung during oscillatory ventilation

Jacob Herrmann,^{1,2} Merryn H. Tawhai,³ and David W. Kaczka^{1,2,4}

¹Department of Anesthesia, University of Iowa, Iowa City, Iowa; ²Department of Biomedical Engineering, University of Iowa, Iowa City, Iowa; ³Auckland Bioengineering Institute, University of Auckland, Auckland, New Zealand; and ⁴Department of Radiology, University of Iowa, Iowa City, Iowa

Submitted 1 February 2016; accepted in final form 29 September 2016

Herrmann J, Tawhai MH, Kaczka DW. Regional gas transport in the heterogeneous lung during oscillatory ventilation. *J Appl Physiol* 121: 1306–1318, 2016. First published October 7, 2016; doi:10.1152/japplphysiol.00097.2016.—Regional ventilation in the injured lung is heterogeneous and frequency dependent, making it difficult to predict how an oscillatory flow waveform at a specified frequency will be distributed throughout the periphery. To predict the impact of mechanical heterogeneity on regional ventilation distribution and gas transport, we developed a computational model of distributed gas flow and CO₂ elimination during oscillatory ventilation from 0.1 to 30 Hz. The model consists of a three-dimensional airway network of a canine lung, with heterogeneous parenchymal tissues to mimic effects of gravity and injury. Model CO₂ elimination during single frequency oscillation was validated against previously published experimental data (Venegas JG, Hales CA, Strieder DJ, *J Appl Physiol* 60: 1025–1030, 1986). Simulations of gas transport demonstrated a critical transition in flow distribution at the resonant frequency, where the reactive components of mechanical impedance due to airway inertia and parenchymal elastance were equal. For frequencies above resonance, the distribution of ventilation became spatially clustered and frequency dependent. These results highlight the importance of oscillatory frequency in managing the regional distribution of ventilation and gas exchange in the heterogeneous lung.

high-frequency oscillatory ventilation; gas exchange; lung injury; respiratory mechanics; computational model

NEW & NOTEWORTHY

Regional ventilation in the injured lung is heterogeneous and frequency dependent, making it difficult to predict how an oscillatory flow waveform at a specified frequency will be distributed throughout the periphery. In this study, we developed a computational model of distributed gas flow and CO₂ elimination during oscillatory ventilation. Our simulations indicate that ventilation distribution in a heterogeneous lung is spatially clustered and frequency-dependent, indicating that oscillatory frequency is an important factor in regional gas exchange.

FOR PATIENTS WITH the acute respiratory distress syndrome (ARDS), flow is distributed throughout the lung periphery in a nonuniform and frequency-dependent manner due to mechanical heterogeneity (3, 10). Patients with ARDS are particularly susceptible to the harmful processes of cyclic overdistension and derecruitment, collectively termed ventilator-induced lung injury (VILI). The ensuing mechanical stresses associated with these processes result in the release of inflammatory mediators that may contribute significantly to multiple organ failure and

death (37). Intratidal overdistension and derecruitment often occur simultaneously in different regions of injured lung due to nonuniform distribution of flow (8). Thus optimizing the magnitude and distribution of flow to mitigate VILI is a critical objective of mechanical ventilation in ARDS.

Lung-protective ventilation significantly reduces mortality in patients with ARDS, using high positive end-expiratory pressures to prevent derecruitment and small tidal volumes to avoid overdistension (1). High-frequency oscillatory ventilation (HFOV) is an alternative modality that applies ventilatory rates >2 Hz and is used as a rescue therapy for ARDS patients whose condition is refractory to conventional or lung-protective ventilation (31). Despite the use of smaller tidal volumes compared with lung-protective ventilation, multicenter clinical trials of HFOV in adult ARDS patients failed to demonstrate improvements in mortality (12, 56). This may be due to heterogeneous and frequency-dependent distributions of flow in the periphery, which may contribute to regional lung injury that is not easily observed in patients.

There are several mechanisms by which gas transport occurs during oscillatory flow: direct alveolar ventilation, asymmetric velocity profiles, inspiratory-expiratory differences in velocity profiles, turbulent and oscillatory dispersion, pendelluft phenomenon, cardiogenic mixing, collateral ventilation, and molecular diffusion (9, 31). The relative magnitude of each mechanism's effect within any particular region of the lung may depend on the combination of velocity profile, oscillatory frequency, and airway geometry (9, 30). Computational modeling of gas transport in the lung allows for useful predictions of the impact of frequency and tidal volume on regional gas transport in critically ill patients. Such predictions may provide insight into derangements of gas exchange in mechanically heterogeneous lungs. Computational models exist for predicting effects of specific gas transport mechanisms on total gas exchange during either conventional mechanical ventilation (32) or HFOV (14). Few models are applicable to gas transport in a branching airway structure over a wide range of frequencies (25, 33), yet these are limited by assumptions of symmetrical airway networks and uniform distributions of flow. Current computational models are limited in their ability to simulate heterogeneous gas transport (e.g., CO₂ elimination) spanning a range of frequencies and tidal volumes encompassing conventional mechanical ventilation and HFOV.

The goal of this study was to develop a computational model of regional flow and gas exchange in a three-dimensional airway network during oscillatory ventilation. Specifically, our objectives were: 1) to generate frequency-dependent distributions of advective flow throughout an anatomically structured airway network, imposing either homogeneous or heterogeneous distributions of tissue elastance to reflect healthy and

Address for reprint requests and other correspondence: D. W. Kaczka, Dept. of Anesthesia, Univ. of Iowa Hospital and Clinics, 200 Hawkins Dr., Iowa City, IA 52242 (e-mail: david-kaczka@uiowa.edu).

injured parenchymal mechanics; 2) to simulate gas exchange for any given tidal volume, oscillatory frequency, and flow distribution, based on models of diffusive and advective gas transport phenomena; and finally 3) to assess the frequency-dependence of tidal volumes required for eucapnic ventilation, as well as ventilation heterogeneity for healthy and injured lungs.

Glossary

<i>a</i>	Exponent of frequency, in proportional relationship to total CO ₂ elimination	CT-derived central airways
ARDS	Acute respiratory distress syndrome	Algorithmically generated peripheral airways
<i>b</i>	Exponent of tidal volume, in proportional relationship to total CO ₂ elimination	
CO ₂	Carbon dioxide	
CT	Computed tomography	
C _n CO ₂	Concentration of CO ₂ for <i>n</i> th acinus	
<i>d</i>	Diameter of airway segment	
D _{eff}	Effective diffusivity	
D _{mol}	Molecular diffusivity	
D _{lam}	Laminar oscillatory dispersion coefficient	
D _{dis}	Turbulent oscillatory dispersion coefficient	
D _{turb}		
HFOV	High frequency oscillatory ventilation	
<i>f</i>	Oscillation frequency in Hz	
f _{res}	Resonant frequency in Hz	
f _{min}	Frequency in Hz of local minimum normalized acinar flow magnitude	
f _{max}	Frequency in Hz of local maximum normalized acinar flow magnitude	
\mathcal{F}	Normalized frequency	
<i>l</i>	Length of airway segment	
$\dot{M}_n\text{CO}_2$	Molar flux of CO ₂ for <i>n</i> th acinus	
$\dot{M}_{\text{seg}}^{\text{diff}}\text{CO}_2$	Diffusive component of molar flux of CO ₂ through an airway segment	
$\dot{M}\text{CO}_2$	Vector of acinar CO ₂ molar fluxes	
<i>n</i>	Index through individual acini	
<i>N</i>	Total number of acini	
P _{ao} CO ₂	Partial pressure of CO ₂ at airway opening	
P _a CO ₂	Partial pressure of CO ₂ in mixed arterial blood	
P _n CO ₂	Partial pressure of CO ₂ for <i>n</i> th acinus	
ΔPCO_2	Vector of partial pressure differentials between acini and airway opening	
Q	Normalized flow cost	
r^2	Coefficient of determination	
R	Universal gas constant	
Re	Reynolds number	
Re _{crit}	Critical Reynolds number, transition between laminar and turbulent flow	
$R_{\text{T}}^{\text{diff}}$	Diffusive transport resistance	
$R_{\text{T}}^{\text{mix}}$	Diffusive transport resistance	
$R_{\text{T}}^{\text{tot}}$	Total transport resistance	
R_{T}	Transport resistance matrix	
<i>T</i>	Temperature	
\bar{U}_{RMS}	Root-mean-square mean-axial velocity	
V _D	Total dead space volume	
V _{D,nl}	Magnitude of oscillatory dead space volume delivered to <i>n</i> th acinus	
V _{F,nl}	Magnitude of oscillatory fresh gas volume delivered to <i>n</i> th acinus	
V _{mix}	Oscillatory mixing volume	
V _{seg}	Volume of airway segment	
V _T	Tidal volume	
V _T ^{euc}	Eucapnic tidal ε volume	
\dot{V}_{seg}	Magnitude of oscillatory flow through airway segment	
\dot{V}_{A}	Eucapnic total acinar ventilation	
$\dot{V}_{\text{ao}}^{\text{DDM}}\text{CO}_2$	CO ₂ elimination at the airway opening via diffusion, dispersion, and mixing	
$\dot{V}_n\text{CO}_2$	CO ₂ elimination at acinus <i>n</i> via diffusion, dispersion, and mixing	
$\dot{V}_n^{\text{DDM}}\text{CO}_2$	CO ₂ elimination at acinus <i>n</i> via direct acinar ventilation	
$\dot{V}_n^{\text{DAV}}\text{CO}_2$	Total CO ₂ elimination at the airway opening	
$\dot{V}_{\text{tot}}\text{CO}_2$	Eucapnic total CO ₂ elimination at the airway opening	
$\dot{V}_{\text{tot}}^{\text{euc}}\text{CO}_2$	Ventilator-induced lung injury	
$\beta_0, \beta_1, \beta_2$	Power-law regression coefficients	
π	Radians in semicircle	
ϵ	Constant of proportionality for mixing transport resistance	
ν	Kinematic viscosity	

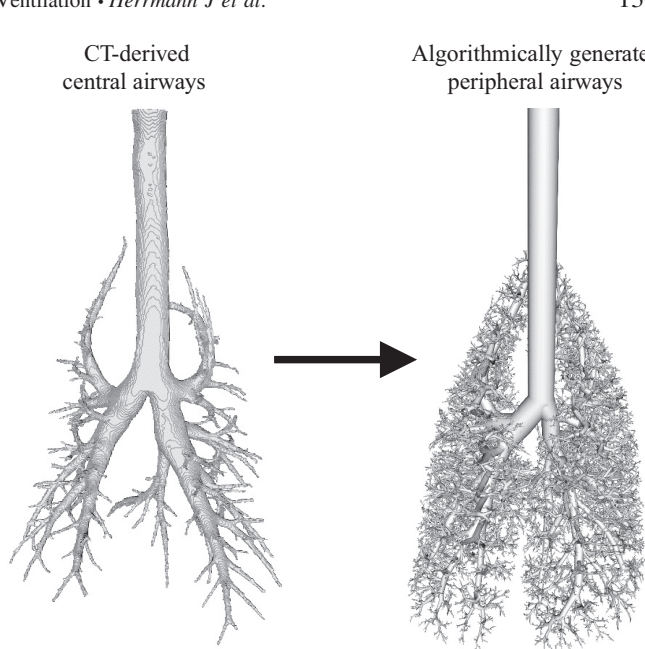


Fig. 1. Central airways of a canine lung as segmented from an X-ray computed tomographic scan in a supine dog (left) and resulting anatomically based 3-dimensional airway network (right) generated using a space-filling algorithm (38, 39).

METHODS

Model structure. The model structure is based on a three-dimensional network of a canine airway tree shown in Fig. 1, in which each airway segment was assumed to be an ideal cylinder with dimensions and spatial position based on a thoracic CT scan of a supine dog inflated to total lung capacity (22). Airways <2 mm diameter were algorithmically generated within the constrained boundaries of segmented lung lobes (38). The length (*l*) and diameter (*d*) of each segment were then scaled down from total

lung capacity to a mean airway opening pressure of 10 cmH₂O, where the size scaling for each airway was determined according to its time-averaged local transmural pressure, defined as the difference between mean luminal pressure and local pleural pressure (3, 41). Local pleural pressure in the model was assumed to vary with gravity by 0.25 cmH₂O/cm according to the hydrostatic weight of pleural fluid in a supine dog (26), with an average value of -5 cmH₂O. Airway dimensions defined longitudinal and shunt impedances to oscillatory flow, which are briefly summarized here from Colletti et al. (10). Airway segment longitudinal impedance was determined assuming Womersley-type oscillatory flow in a cylinder (42, 54). Airway segment shunt impedance was given by a parallel combination of isothermal gas compression compliance, soft tissue viscoelasticity, and cartilaginous viscoelasticity (10, 24). Each terminal airway in the tree was subtended by a viscoelastic "constant-phase" element representing acinar wall distensibility (17) in parallel with gas compression compliance (10, 24). The arrangements of all longitudinal and shunt impedances in the model were defined according to Kaczka et al. (24). Flow oscillations at the airway opening were distributed throughout the lung periphery using a recursive flow-dividing scheme, apportioning flows at each topological branching point among parallel pathways according to their respective total input impedances (10).

Acinar viscoelasticity was determined according to a second-order polynomial function of local transpulmonary pressure (3). Heterogeneous injury was simulated by modulating acinar tissue elastance according to a gravitationally weighted gradient noise distribution using a Perlin method (11), which produces a textured distribution that is smoother and more natural compared with purely random variations in tissue properties (10). Gravitational weighting increased the magnitude of the noise distribution toward the dependent regions of the model, loosely mimicking the effects of fluid accumulation in injured lungs. The resulting distribution of injured acinar tissue elastance demonstrated a mean \pm standard deviation of 1.93 ± 1.19 cmH₂O/ μ L, compared with the healthy case of 0.31 ± 0.02 cmH₂O/ μ L. Cross-sectional views of acinar tissue elastance are provided in Fig. 2.

To simplify computation of mechanical impedance and flow distribution in the frequency-domain we did not consider intratidal variations in model structure or mechanical properties (2). Additionally, CO₂ transport throughout the airway network was solved as a steady-state problem, i.e., time-averaged throughout the oscillatory ventilation cycle and with CO₂ elimination equal to CO₂ production.

Diffusive transport. To approximate CO₂ diffusion in the tree, we assumed that molar flux of CO₂ in the axial direction of each airway segment due only to diffusive phenomena ($\dot{M}_{\text{seg}}^{\text{diff}}\text{CO}_2$) was proportional to its axial partial pressure difference ($\Delta P_{\text{seg}}\text{CO}_2$):

$$\dot{M}_{\text{seg}}^{\text{diff}}\text{CO}_2 = \frac{1}{R_T^{\text{diff}}} \Delta P_{\text{seg}}\text{CO}_2 \quad (1)$$

where R_T^{diff} is the diffusive transport resistance:

$$R_T^{\text{diff}} = \frac{4\mathcal{R}Tl}{\pi d^2 D_{\text{eff}}} \quad (2)$$

The \mathcal{R} parameter is the universal gas constant, T is body temperature, and D_{eff} the effective diffusivity constant for CO₂ contained in the airway segment. Under zero-flow conditions, D_{eff} is equal to the molecular diffusivity D_{mol} . However during advective flow, the effective diffusivity D_{eff} includes dispersive components to account for enhanced diffusion resulting from transient velocity profile changes during laminar oscillatory flow (50) or the mixing of eddies during turbulent oscillatory flow (14, 40):

$$D_{\text{eff}} = \begin{cases} D_{\text{mol}} + D_{\text{dis}}^{\text{laminar}}, & \text{Re} < \text{Re}_{\text{crit}} \\ D_{\text{mol}} + D_{\text{dis}}^{\text{turbulent}}, & \text{Re} \geq \text{Re}_{\text{crit}} \end{cases} \quad (3)$$

where $D_{\text{dis}}^{\text{laminar}}$ and $D_{\text{dis}}^{\text{turbulent}}$ are the laminar and turbulent oscillatory dispersion coefficients, respectively, and Re is the Reynolds number given by the airway segment diameter d , kinematic gas viscosity ν , and root-mean-square mean-axial velocity \bar{U}_{RMS} :

$$\text{Re} = \frac{\bar{U}_{\text{RMS}}d}{\nu} \quad (4)$$

The critical Reynolds number ($\text{Re}_{\text{crit}} = 30$) characterizes the transition from laminar to turbulent oscillatory flow (35). While $D_{\text{dis}}^{\text{laminar}}$ is dependent on oscillatory frequency (35, 50), $D_{\text{dis}}^{\text{turbulent}}$ depends only on the root-mean-square mean-axial velocity that characterizes eddy mixing strength (14). To account for additional advective gas mixing at airway bifurcations, we developed a mixing transport resistance (R_T^{mix}) for each segment:

$$R_T^{\text{mix}} = \frac{\mathcal{R}T}{fV_{\text{mix}}} \quad (5)$$

where f is the oscillatory frequency of the advective flow waveform in Hz, and V_{mix} is the amplitude of volume flux through the airway segment. Thus, R_T^{mix} characterizes net gas transport from mixing the volume of gas passing completely through an airway segment during each period of oscillatory flow. Therefore R_T^{mix} will be nonzero only when this oscillating volume exceeds the volume of the airway segment, V_{seg} , given by:

$$V_{\text{mix}} > V_{\text{seg}} = \frac{1}{4}\pi d^2 l \quad (6)$$

where V_{mix} is:

$$V_{\text{mix}} = \frac{|\dot{V}_{\text{seg}}(f)|}{\pi f} - V_{\text{seg}} \quad (7)$$

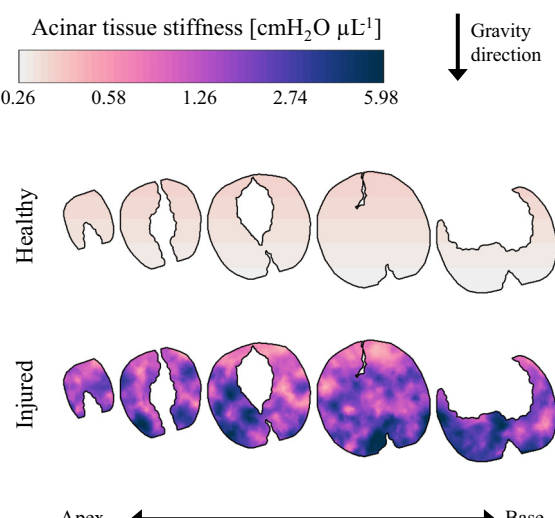


Fig. 2. Transverse cross sections of simulated regional acinar tissue stiffness for healthy (upper) and injured (lower) conditions, spatially interpolated between acinar elements for visualization.

and $|\dot{V}_{\text{seg}}(f)|$ is the magnitude of oscillatory flow in the airway segment at frequency f . The mixing transport resistance is derived in more detail in APPENDIX A-1.

The total transport resistance for each airway ($R_{\text{T}}^{\text{tot}}$) is the parallel combination of diffusive and mixing transport resistances:

$$R_{\text{T}}^{\text{tot}} = \frac{1}{\frac{1}{R_{\text{T}}^{\text{diff}}} + \frac{1}{R_{\text{T}}^{\text{mix}}}} = \frac{R_{\text{T}}^{\text{diff}} R_{\text{T}}^{\text{mix}}}{R_{\text{T}}^{\text{diff}} + R_{\text{T}}^{\text{mix}}} \quad (8)$$

An upper bound on $R_{\text{T}}^{\text{tot}}$ is obtained in the zero-flow limiting case when $V_{\text{mix}} \rightarrow 0$ and $R_{\text{T}}^{\text{mix}} \rightarrow \infty$. In this case $R_{\text{T}}^{\text{tot}} = R_{\text{T}}^{\text{diff}}$ and $D_{\text{eff}} = D_{\text{mol}}$.

Once $R_{\text{T}}^{\text{tot}}$ is computed for each airway in the network, a mesh analysis (APPENDIX A-2) forms a system of equations for solving the molar flux of CO_2 at each acinus, given the partial pressure differential between each acinus and the airway opening:

$$R_{\text{T}} \dot{M} \text{CO}_2 = \Delta P \text{CO}_2 \quad (9)$$

where R_{T} is a full matrix of transport resistances (APPENDIX A-2), $\dot{M} \text{CO}_2$ is a vector of acinar CO_2 molar fluxes (i.e., for the n th acinus: $\dot{M}_n \text{CO}_2$), and $\Delta P \text{CO}_2$ is a vector of CO_2 partial pressure differentials between acini and airway opening (i.e., for the n th acinus: $\Delta P_n \text{CO}_2 = P_n \text{CO}_2 - P_{\text{ao}} \text{CO}_2$). Each row of the system corresponds to the mesh formed by the airways connecting a single acinus to the airway opening. The partial pressure of CO_2 at the airway opening was assumed to be zero. After solving the system of equations, the CO_2 elimination due to diffusion, dispersion, and mixing ($\dot{V}_n^{\text{DDM}} \text{CO}_2$) for each acinus can be converted from the molar flux using the ideal gas law:

$$\dot{V}_n^{\text{DDM}} \text{CO}_2 = \frac{RT}{P_{\text{atm}}} \dot{M}_n \text{CO}_2 \quad (10)$$

The mesh analysis ensures conservation of mass between CO_2 elimination at the airway opening ($\dot{V}_{\text{ao}}^{\text{DDM}} \text{CO}_2$) and the sum of $\dot{V}_n^{\text{DDM}} \text{CO}_2$ across all acini.

Advective transport. The distribution of advective flow throughout the airway tree was computed using a recursive flow divider algorithm (10). Direct acinar ventilation occurs when volume amplitudes at the airway opening are sufficiently large to allow fresh gas mixing directly with acinar gas during inspiration, effectively bypassing $R_{\text{T}}^{\text{diff}}$ and $R_{\text{T}}^{\text{mix}}$ in Eq. 8. To model this mechanism of gas transport, we assume that the volume of fresh gas delivered to each acinus is completely mixed during inspiration and that the same volume of mixed gas is completely removed during expiration, according to Fig. 3. CO_2 elimination due to direct acinar ventilation is computed according to the concept of “personal dead space,” which apportions an amount of inspired fresh gas to each individual acinus (13).

In this manner, the dead space of all conducting airways was successively distributed in proportion to the flow distribution through subtending airways until reaching the terminal acini. Thus the distribution of personal dead space is dependent on frequency, in accordance with the distribution of flow. We determined the CO_2 elimination due to direct acinar ventilation ($\dot{V}_n^{\text{DAV}} \text{CO}_2$) for a particular acinar compartment by comparing its personal dead space volume [$V_{D,n}(f)$] to the total volume delivered to that acinus over one period of oscillation:

$$\dot{V}_n^{\text{DAV}} \text{CO}_2 = \frac{P_n \text{CO}_2}{863} f |V_{F,n}| \quad (11)$$

where 863 is a conversion factor between partial pressure in mmHg and gas volume fraction,¹ $P_n \text{CO}_2$ is the partial pressure of acinar CO_2 , and

¹ The conversion factor accounts for the difference between standard temperature and pressure dry (STPD) air and body temperature and pressure air saturated with water vapor (BTPS).

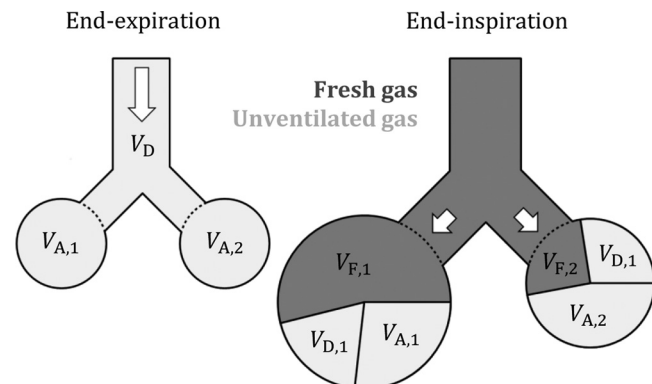


Fig. 3. Direct acinar ventilation is modeled by assuming complete mixing within each n th terminal acinus of inspired fresh gas ($V_{F,n}$), inspired dead space gas ($V_{D,n}$), and residual volume ($V_{A,n}$). The concept of “personal dead space” is used to distribute the total dead space (V_D) throughout all acini in proportion to the magnitude of the ventilation distribution (13).

$|V_{F,n}|$ is the magnitude of frequency-dependent fresh gas volume delivered to the acinus given by:

$$|V_{F,n}| = \begin{cases} \frac{|\dot{V}_n(f)|}{\pi f} - |V_{D,n}(f)|, & \frac{|\dot{V}_n(f)|}{\pi f} > |V_{D,n}(f)| \\ 0, & \text{otherwise} \end{cases} \quad (12)$$

$|\dot{V}_n(f)|$ is the magnitude of oscillatory flow at frequency f in the terminal acinus. Note that if the total volume of inspired gas delivered to an acinus over one period of oscillation is less than the personal dead space of that acinus, there will be no contribution of direct acinar ventilation to CO_2 elimination from that particular acinus. Total dead space volume (V_D) was calculated as the sum of all cylindrical airway segment volumes.

Total transport and eucapnia. Total CO_2 elimination ($\dot{V}_{\text{tot}} \text{CO}_2$) for the model at a specified frequency was computed from the sum of CO_2 elimination across all N acini:

$$\dot{V}_{\text{tot}} \text{CO}_2 = \sum_{n=1}^N \dot{V}_n \text{CO}_2 \quad (13)$$

where n indexes individual acini, and the CO_2 elimination in each acinus ($\dot{V}_n \text{CO}_2$) is determined by the sum of CO_2 elimination via direct acinar ventilation and by solving the system of transport resistances:

$$\dot{V}_n \text{CO}_2 = \dot{V}_n^{\text{DAV}} \text{CO}_2 + \dot{V}_n^{\text{DDM}} \text{CO}_2 = \frac{P_n \text{CO}_2}{863} f |V_{F,n}| + \frac{RT}{P_{\text{atm}}} \dot{M}_n \text{CO}_2 \quad (14)$$

Equation 14 assumes that each acinar CO_2 partial pressure is equal to its corresponding end-capillary CO_2 partial pressure. Mixed-venous blood was assumed to enter each capillary with 46 mmHg CO_2 partial pressure. However end-capillary CO_2 partial pressure for each acinus is determined by the rates of acinar CO_2 elimination and perfusion. Thus the distribution of $P_n \text{CO}_2$ is dependent on the distribution of acinar CO_2 elimination, and Eq. 14 for total CO_2 elimination must be solved iteratively. An optimization routine minimized the error in conservation of mass for each acinar compartment, such that CO_2 elimination via ventilation (i.e., Eq. 14) was equal to the product of perfusion rate and CO_2 content difference between end-capillary and mixed-venous blood (53). Eucapnic ventilation was assumed to occur when total CO_2 elimination for the model approximately equaled the predicted metabolic CO_2 production for a 25 kg dog ($1.93 \cdot 10^{-3} \cdot \text{L s}^{-1}$) (18).

Simulations. The recursive algorithms for computing and storing impedances and determining advective flow division throughout the

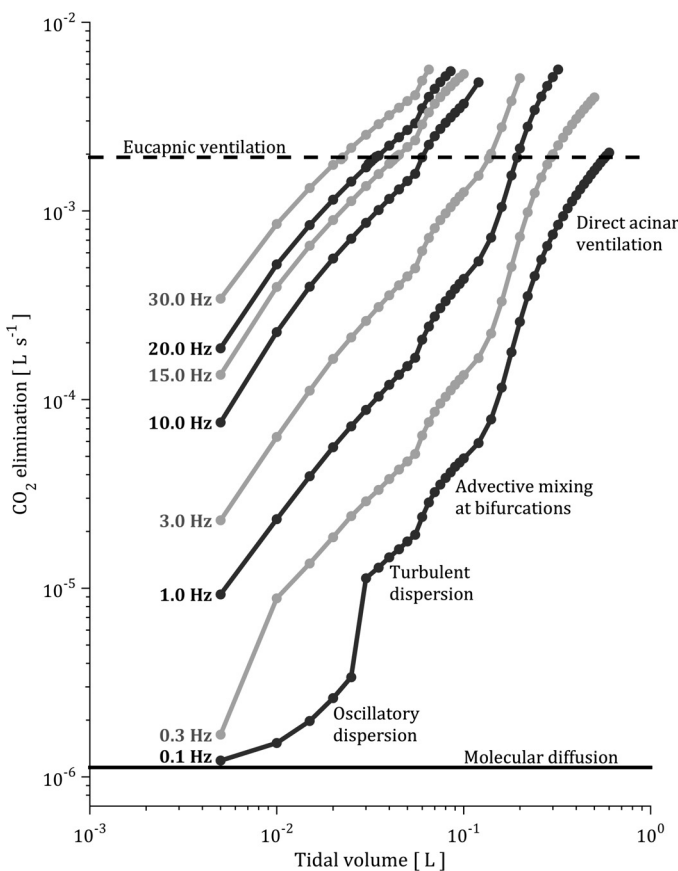


Fig. 4. Simulation results for $\dot{V}_{\text{tot}}\text{CO}_2$ as a function of V_T and f . Solid black line represent the lower bound of total CO_2 elimination due solely to molecular diffusion (i.e., zero-flow conditions), while the dashed horizontal line represents total CO_2 elimination to achieve eucapnia for a 25 kg dog. Text labels indicate dominant gas transport mechanism during 0.1 Hz oscillation.

tree were written in C++. Computation time for generating advective flow distribution at each distinct f was ~3 s on a 64-bit computer with an Intel Core i7-950 processor operating at 3.07 GHz with 12 GB RAM. The gas transport model was written and executed in MATLAB (version 7.13, The Mathworks, Natick, MA). Total computation time for each distinct f and V_T simulation was ~300 s.

The mechanical impedance and ventilation distribution for the model were computed at 115 distinct frequencies, spanning 0.1–100 Hz. The resonant frequency (f_{res}), at which the reactive component of total lung impedance is zero, was determined by interpolation. Gas transport distributions were computed for a range of volume amplitudes at each frequency between 0.1 and 30 Hz, with emphasis on smaller volume amplitudes at higher frequencies. Volume amplitudes

were selected between 5 and 600 ml, chosen to ensure that a simulation representative of eucapnic ventilation was computed at each frequency. The tidal volume required for eucapnic ventilation (V_T^{euc}) as a function of frequency was regressed to a power-law (47):

$$V_T^{\text{euc}}(f) = \beta_0 + \beta_1 f^{\beta_2} \quad (15)$$

The parameters β_0 , β_1 , and β_2 were estimated using a nonlinear least-squares technique (MATLAB v7.13).

To quantify the heterogeneity of ventilation distribution, we examined the amplitude and phase histograms of acinar flows as functions of oscillatory frequency for both health and injured conditions, along with the histograms for acinar CO_2 elimination. Acinar flow magnitudes were normalized relative to the theoretical values obtained for a perfectly symmetric, homogeneous lung with rigid airway walls and no gas compression (i.e., perfectly uniform ventilation distribution). Acinar flow phases were normalized relative to the tracheal flow phase, constrained to be within $\pm 180^\circ$. Bin sizing for normalized acinar flow magnitudes, phases, and $\dot{V}_n\text{CO}_2$ were 167 per decade, 1.39 per degree, and 167 per decade, respectively.

RESULTS

Validation. Figure 4 shows simulation results for $\dot{V}_{\text{tot}}\text{CO}_2$ as a function of V_T and f during oscillatory ventilation with a single frequency. Simulations are shown for each frequency with increasing V_T increments of 5 ml, until $\dot{V}_{\text{tot}}\text{CO}_2$ exceeded the predicted value for eucapnia. The required CO_2 elimination to maintain eucapnia ($\dot{V}_{\text{tot}}^{\text{euc}}\text{CO}_2$) is also indicated, as well as $\dot{V}_{\text{tot}}\text{CO}_2$ produced by molecular diffusion only (i.e., zero-flow conditions) which establishes the lower bound of CO_2 elimination regardless of V_T or f . There are noticeably different behaviors for $\dot{V}_{\text{tot}}\text{CO}_2$ with respect to V_T and f . Specifically, there are certain ranges of volume amplitudes for which certain gas transport mechanisms dominate the others: starting from the lower bound molecular diffusion, there are dramatic increases in $\dot{V}_{\text{tot}}\text{CO}_2$ with the advent of oscillatory dispersion, followed by turbulent dispersion, advective mixing at bifurcations, and finally direct acinar ventilation. These ranges were identified by iteratively eliminating specific gas transport mechanisms from the model, and then resimulating $\dot{V}_{\text{tot}}\text{CO}_2$.

Figure 5 shows V_T^{euc} as a function of frequency over localized frequency domains $0.1 \text{ Hz} < f < 1 \text{ Hz}$ and $2 \text{ Hz} < f < 30 \text{ Hz}$. Regression curves are extended beyond the fit domains to demonstrate the relative reductions in required volume amplitudes that occur inside each range compared with the extrapolated fit of the other range. Parameter estimates are provided in Tables 1 and 2. Expected values for low-frequency gas exchange (i.e., $0.1 \text{ Hz} < f < 1 \text{ Hz}$) are derived from standard equations of gas exchange during conventional mechanical

Fig. 5. Simulation results representing model predictions for eucapnic ventilation at various single frequencies of oscillation (dashed black lines). Dotted vertical black lines represent the resonant frequency (f_{res} ; elastic and inertial components of impedance equal and opposite). Model predictions of tidal volume required for eucapnic ventilation derived from power-law regressions over low frequencies (purple: $0.1 \leq f \leq 1 \text{ Hz}$) and high frequencies (blue: $2 \leq f \leq 30 \text{ Hz}$).

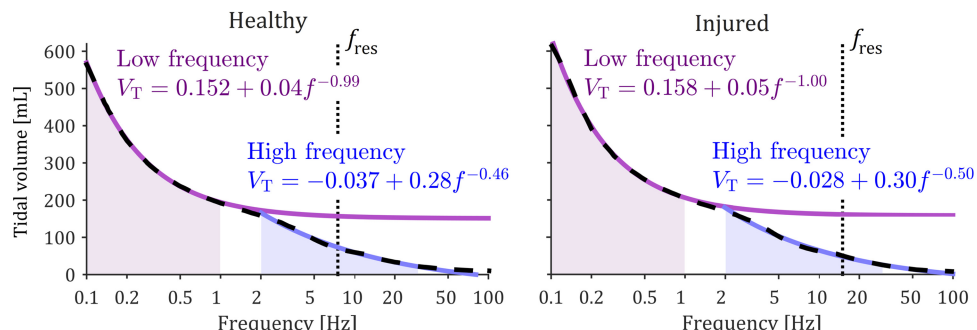


Table 1. Power-law regression parameters for Eq. 15 during low frequency oscillatory ventilation

Parameter	Expected Value	Regression Estimate	Deviation from Expected Value, %
β_0	$V_D = 0.169$	0.151	10.7
β_1	$863 \frac{fV_T}{\dot{V}_A} \dot{V}_{tot}^{euc} CO_2 = 0.042$	0.043	2.2
β_2	-1	-0.99	1.1

ventilation and spontaneous breathing (APPENDIX A-3). Expected values for high frequency gas exchange (i.e., 2 Hz < $f < 30$ Hz) are obtained from previous experimental studies.

Figure 6 shows a comparison between these interpolated eucapnic simulation results and experimental data from Venegas et al. (47), converted to dimensionless equations of gas exchange:

$$Q = \frac{fV_T^{euc}(f)}{\dot{V}_A} \quad (16)$$

$$\mathcal{F} = \frac{fV_D}{\dot{V}_A} \quad (17)$$

where Q and \mathcal{F} are the normalized flow cost and normalized frequency, respectively, and \dot{V}_A is the total acinar ventilation required for eucapnia:

$$\dot{V}_A = \left(863 \frac{\dot{V}_{tot}^{euc} CO_2}{P_a CO_2} \right) \quad (18)$$

where $P_a CO_2$ is the eucapnic partial pressure of CO_2 in mixed arterial blood. The low-frequency relationship $Q = 1 + \mathcal{F}$ corresponds to theoretical gas exchange primarily via direct acinar ventilation, whereas the high-frequency relationship $Q = 0.40\mathcal{F}^{0.54}$ is a regression to experimentally acquired data (47). The model accurately predicts the transition from low-frequency to high-frequency gas exchange behavior, and simulation results demonstrate close qualitative and quantitative agreement with the experimental data of Venegas et al. (47), deviating at the highest frequencies ($\mathcal{F} > 60$, or $f > 12.8$ Hz).

Impact of heterogeneity. Figure 7 shows five transverse model cross sections that are color-coded to depict the distribution of normalized acinar flows, along with acinar CO_2 elimination rates, for frequencies between 0.2 and 30 Hz.

Table 2. Ratio of power-law exponents for CO_2 elimination as a function of f^a and V_T^b during high frequency oscillatory ventilation, as reported in various studies

Study	Species	b/a
Slutsky et al. 1981 (36)*	dog	1.7
Berdine et al. 1984 (7) [†]	dog	1.9
Jaeger 1991 (19)	dog	1.9
Jaeger et al. 1984 (20)	dog	2.0
Venegas et al. 1985 (45)	dog	2.1
Present study	dog	2.1
Venegas et al. 1986 (47)	various	2.2
Watson, Jackson 1985 (52)	monkey	1.9
Watson, Jackson 1984 (51)	rabbit	2.7

Only the ratio of b to a is presented because the power-law regression in Eq. 15 determines only the relative relationship between frequency and volume amplitude. *Values for a and b reported by Venegas et al. (47). [†]Values for a and b reported by Chang (9).

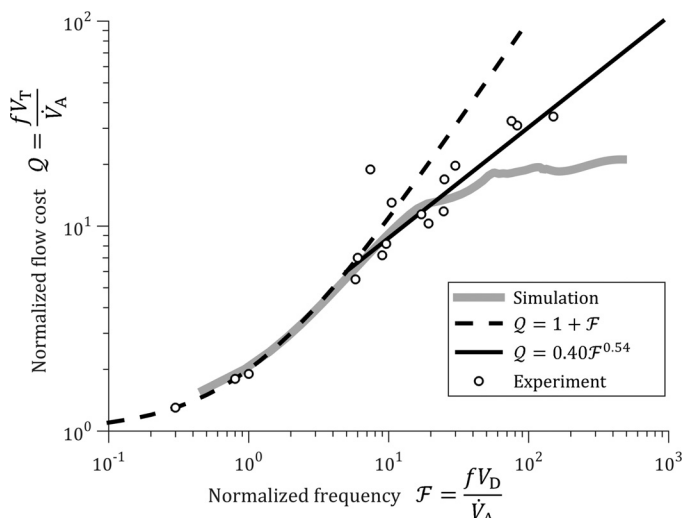


Fig. 6. Comparison between simulation results and experimental data of Venegas et al. (47). The axes are dimensionless variables of frequency (F) and flow (Q). The black lines correspond to theoretical predictions of low-frequency gas exchange (dashed) and regression to experimental HFOV data (solid). The gray line represents the simulations results interpolated at eucapnic conditions.

bution of normalized acinar flows, along with acinar CO_2 elimination rates, for frequencies between 0.2 and 30 Hz. Acinar flow magnitudes were normalized relative to their corresponding values for a perfectly symmetric, homogeneous lung with rigid airway walls and no gas compression. The distribution of acinar CO_2 elimination was normalized to the total CO_2 elimination divided by the number of acini. The coefficients of determination between acinar flow magnitude and CO_2 elimination (r^2) at each frequency and condition are also shown. Acinar CO_2 elimination was positively correlated with acinar flow magnitude for either condition, although the correlation tended to decrease with increasing frequency. Gravitational gradients were apparent at low frequencies for the healthy condition, yet diminish with increasing frequency. For the injured condition, the distributions of both flow and CO_2 elimination were spatially concordant with the distribution of acinar tissue stiffness (Fig. 2) for the frequencies shown.

Figure 8 shows two-dimensional histograms of normalized acinar flow magnitude and phase distributions for healthy and injured conditions, along with the acinar CO_2 elimination distribution from 0.1 to 100 Hz. Acinar flow phase was normalized relative to the corresponding tracheal flow phase, constrained to be within $\pm 180^\circ$. The histograms are color-coded based on the percentage of acini in the model. For frequencies less than resonance, ventilation distribution is largely frequency independent. However, when the oscillatory frequency exceeds resonance, ventilation distribution becomes both frequency dependent and heterogeneous, even for the mechanically homogeneous healthy case. The low-frequency ventilation distribution is much more homogeneous for the healthy case compared with the injured case, as expected. However the effect of high frequency on ventilation heterogeneity is comparable between the two conditions, in both cases increasing heterogeneity with increasing $f > f_{res}$. Above f_{res} the mean normalized acinar flow magnitude exceeded unity, indicating

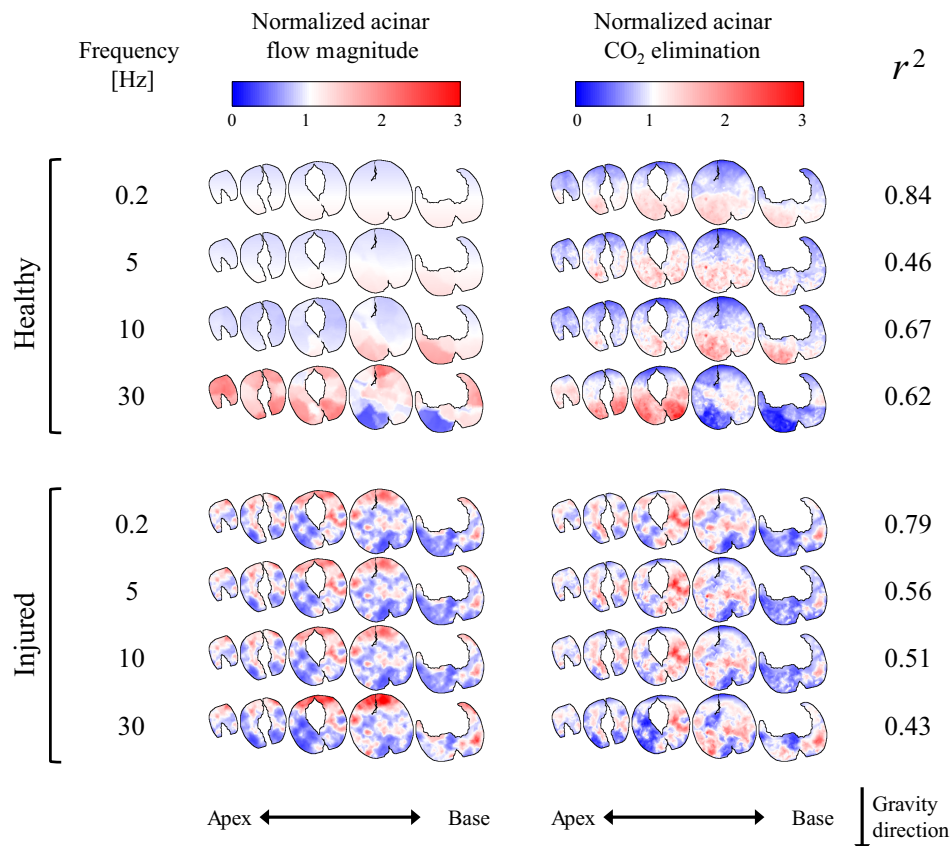


Fig. 7. Transverse cross sections of simulated regional acinar flow magnitude (left) and CO₂ elimination (right) at selected oscillatory frequencies, for healthy (top) and injured (bottom) conditions, spatially interpolated between acinar elements for visualization. Coefficients of determination (r^2) between acinar flow magnitude and CO₂ elimination are shown at the far right.

cating that the sum of acinar flow magnitudes was greater than the tracheal flow magnitude. The increase in mean acinar flow magnitudes above f_{res} is coincident with increased acinar phase variance. Multimodal patterns were also visible in histograms, reflecting large groups of acini with similar frequency-dependent behavior.

To determine whether such multimodality in ventilation distribution was consistent with anatomic grouping, we color-coded individual acini according to the frequency at which they experienced either a local minimum (f_{min}) or maximum (f_{max}) normalized flow magnitude. Figure 9 shows the spatial anatomic distributions of f_{min} and f_{max} for the three-dimensional model. Spatially organized clusters of acini with the same f_{min} or f_{max} values are immediately apparent, implying that overventilation and underventilation may manifest simultaneously in clusters of the lung, in a frequency-dependent manner. The particular pattern of clustering was similar between the healthy and injured conditions, despite substantial differences in the distribution of tissue elastance (Fig. 2).

DISCUSSION

In this study, we developed an anatomic computational model of gas exchange during oscillatory ventilation by incorporating mechanical impedance and pertinent gas transport mechanisms over a wide range of frequencies. The dominant mechanism of gas transport exhibits strong scaling dependence on V_T , with transitions from molecular diffusion near zero-flow conditions to laminar oscillatory dispersion, then turbulent dispersion, then advective mixing at bifurcations, and finally direct acinar ventilation at the largest V_T . The transition from

laminar dispersion to turbulent dispersion is determined by a critical Reynolds number, which was set at $Re_{crit} = 30$ (35). Values of Re are proportional to the root-mean-square axial flow velocity, which implies dependence on both volume amplitude and oscillatory frequency. Therefore, the transition from laminar to turbulent dispersion will occur at different volume amplitudes for each frequency. Laminar oscillatory dispersion alone is not sufficient to provide eucapnic ventilation at a reasonably small V_T for any f in the simulated range between 0.1 and 30 Hz. By contrast, the transition to turbulence yields about an order-of-magnitude increase in $\dot{V}_{tot}CO_2$, such that for high frequencies ($f > 10$ Hz), adequate $\dot{V}_{tot}CO_2$ is achieved primarily via dispersion.

For intermediate frequencies (between 1 and 10 Hz), mixing at bifurcations contributes the most to eucapnic ventilation, nearly doubling $\dot{V}_{tot}CO_2$ compared with dispersion alone. The transition from dispersion-dominated to bifurcation-mixing-dominated gas transport occurs at a constant V_T between 50 and 60 ml across all frequencies. The trachea of our canine model has a luminal volume of 56.3 ml, which is by far the largest volume of any airway in the tree: the next largest is 6.5 ml, followed by 2.2 ml. Thus we may safely assume that advective mixing at airway bifurcations in the model has the greatest effect on total gas transport for V_T larger than tracheal volume.

The final transition in dominant gas transport mechanisms is attributable to the increasing prevalence of direct acinar ventilation. Occurring only at the largest V_T , this mechanism requires a front of fresh gas to move directly between the airway opening and the acinar compartments, producing sub-

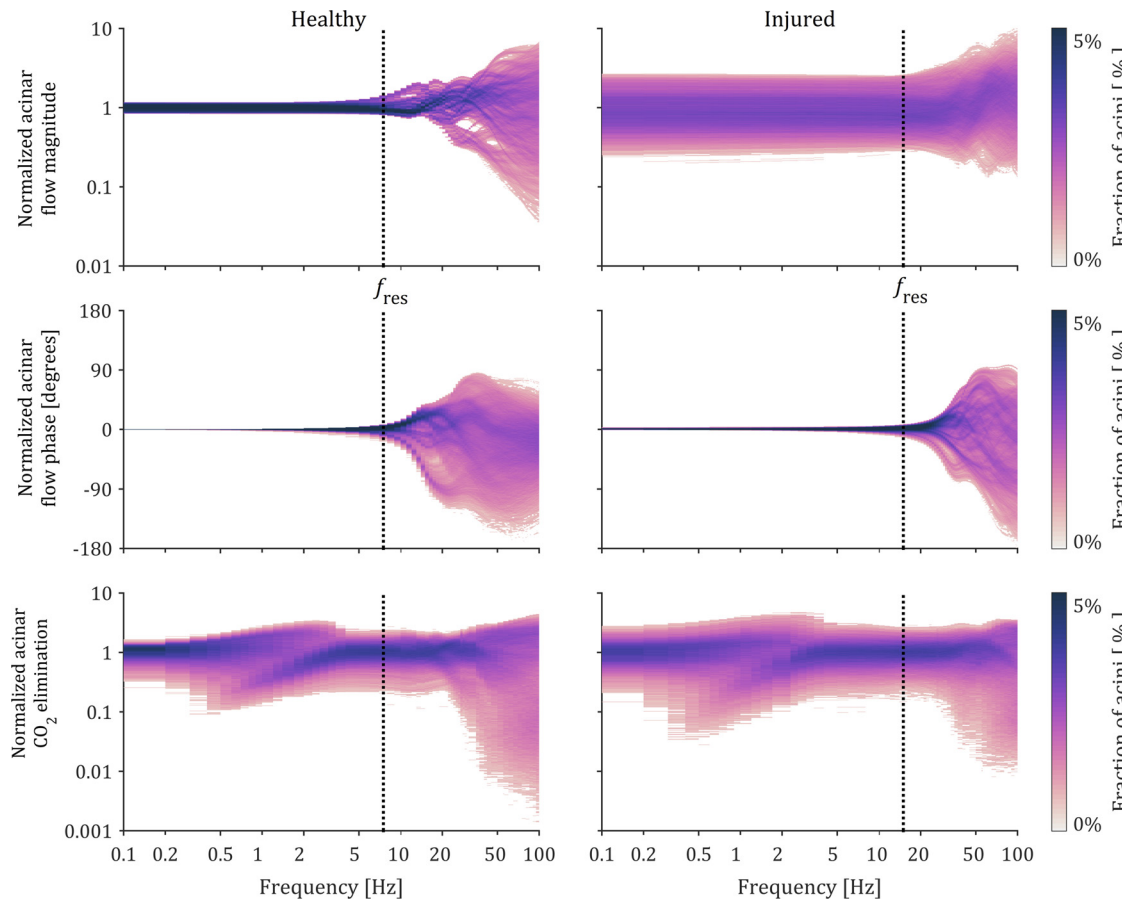


Fig. 8. Simulation representing model predictions for eucapnic ventilation vs. oscillatory frequency. Horizontal axes are aligned, dashed black lines represent the resonant frequency (f_{res} : elastic and inertial components of impedance equal and opposite). Acinar flow magnitude, flow phase, and CO₂ elimination are normalized as described in the text.

stantial gas transport via advection. The transition to direct acinar ventilation occurs over a wider range of V_T compared with the other mechanisms, due to differences in the ventilation distribution as well as the distribution of path lengths. The impact of direct acinar ventilation on gas transport is also much larger than that of any other mechanism for CO₂ elimination by almost an order of magnitude.

The last two transitions seem to have constant V_T thresholds, whereas the diffusion and dispersion transitions are f dependent as well as V_T dependent. This can be explained by the physical dependence of direct acinar ventilation and bifurcation mixing on the size and arrangement of dead space in the conducting airways, whereas dispersion depends more strongly on the magnitude, frequency, and cross-sectional profile of the flow waveform.

Pendelluft occurs when lung regions with differing mechanical time constants oscillate out of phase with respect to each other, resulting in increased intrapulmonary gas mixing and homogenization (16, 29). In this model of time-averaged gas transport, pendelluft manifests as increased acinar phase variance and flow magnitude, as shown in Fig. 8. Gas mixing is increased between lung regions oscillating out of phase, due to increased flow magnitude in each region. The simulations performed in this study indicate that pendelluft occurs primarily above the resonant frequency, consistent with experimental findings of phase variance using stroboscopic measurements of the lung surface (27) and alveolar pressure capsules (15).

Validation. Simulations from this canine lung model, under healthy conditions with near homogeneous mechanical properties, exhibit agreement with experimental results regarding the behavior of $\dot{V}_{tot}CO_2$ with respect to f , V_T , and V_D (47). Low- f gas exchange is dominated by direct acinar ventilation.

The personal dead space and alveolar mixing models demonstrate concordance with expected behavior of CO₂ elimination during conventional mechanical ventilation and spontaneous breathing. Theoretical predictions and empirical findings for power-law behavior of high- f CO₂ elimination are relatively more inconsistent by comparison. In general it is accepted that $\dot{V}_{tot}CO_2$ depends more strongly on V_T than on f according to:

$$\dot{V}_{tot}CO_2 \propto f^a V_T^b \quad (19)$$

with $a < b$ (31). The exponent values obtained from these simulations are within the range of values provided in the literature, represented in Table 2 (9, 47).

Considering the normalized representation of flow cost vs. frequency used by Venegas et al. (47), the simulation results are in close qualitative and quantitative agreement with experimental results. However, our simulations underestimated the normalized flow cost Q at the highest frequencies (i.e., $F > 60$, or $f > 12.8$ Hz) in animals. This discrepancy may be attributed

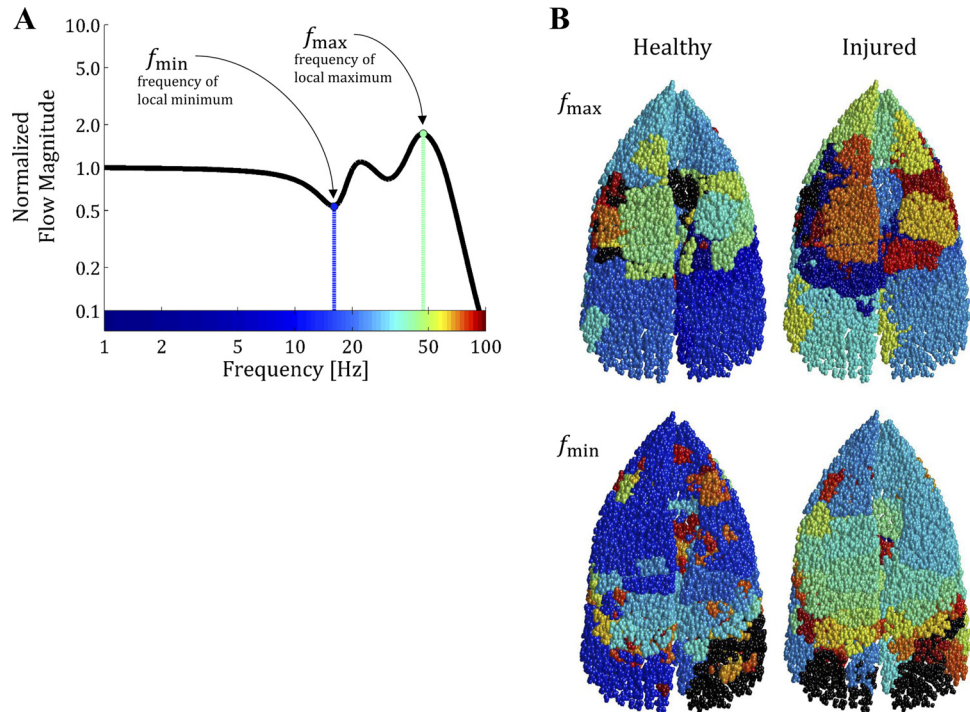


Fig. 9. *A:* frequencies of maximum and minimum normalized flow magnitude, shown for clarity in the context of a single acinus. *B:* frequencies of maximum (*top*) and minimum (*bottom*) normalized flow magnitude, represented spatially for every acinus, using consistent coloring according to the scale provided in *A*. Acinar flow magnitude is normalized to the uniform distribution (unity corresponds to tracheal magnitude divided by total number of acini). Acini that do not exhibit a local minimum or maximum within the range of frequencies simulated are shown in black. The gravitational vector points out of the page, toward the reader.

to an overemphasized effect of turbulent dispersion in the model and may be improved by the fine-tuning of a scaling parameter used to calculate $D_{\text{dis}}^{\text{turb}}$. In previous studies, Fredberg (14) used an order-of-magnitude approximation to set the scaling parameter equal to unity, while Slutsky et al. (35) used an average value obtained from inspiratory and expiratory flows in a mechanical model (34) used an average value obtained from inspiratory and expiratory flows in a mechanical model. It is possible that more accurate values of the scaling parameter during the turbulent flows of HFOV may be obtained either through experiment or through computational fluid dynamics (CFD) simulation.

Impact of heterogeneity and frequency selection during HFOV. We can make several predictions about the impact of frequency selection on ventilation heterogeneity during HFOV, by jointly observing the frequency dependence of the acinar flow distribution, acinar $\dot{V}_n\text{CO}_2$ distribution, and total eucapnic volume amplitude. The resonant frequency f_{res} marks the transition from elastically dominated to inertially dominated flow. For frequencies less than f_{res} , flow distribution heterogeneity is frequency independent and determined primarily by the distribution of resistive and elastic properties. For frequencies greater than f_{res} , the transition to frequency-dependent flow heterogeneity suggests that local transitions from elastically dominated to inertially dominated flow occur at different frequencies throughout the lung, depending on local mechanical, geometrical, and topological properties. The multimodal behavior of the flow heterogeneity (Fig. 8) and the spatial distributions of f_{min} and f_{max} (Fig. 9) suggest that frequency-dependent behavior of the flow distribution is regionally clustered. Note that two acini sharing the same value of f_{max} does not imply also sharing the same value of f_{min} , suggesting that subtle differences between mechanical properties of neighboring acini produce noticeable differences in frequency dependence of ventilation distribution. Furthermore, the healthy and

injured conditions exhibited similar clustering, suggesting that the frequency-dependent behavior of ventilation distribution is largely determined by airway properties affecting inertance (i.e., airway size, path-length between airway opening and acinus, airway network topology) rather than tissue properties in this particular model of injury.

The transition from low- f to high- f gas exchange, which occurs between 0.5 and 5 Hz in our canine model, is associated with increased acinar $\dot{V}_n\text{CO}_2$ heterogeneity despite no change in flow distribution heterogeneity. This can be explained by the nonuniform distribution of personal dead space across the acini. Even if flow is distributed uniformly, differences in path-length, airway network symmetry, and airway sizes cause some acini to receive less fresh gas per oscillatory period than others. As the rate of ventilation increases, the tidal volume required for eucapnia decreases, and the acini with large personal dead space do not participate in direct acinar ventilation. A bimodal distribution of acinar CO_2 elimination exists over the transition range $0.5 \text{ Hz} < f < 5 \text{ Hz}$, with one mode corresponding to acini receiving direct acinar ventilation and the other mode correspond to acini eliminating CO_2 only via mixing and dispersion. For example, the fraction of acini receiving direct acinar ventilation in the healthy simulations reduced to 50% at 1.6 Hz and 0% at 5 Hz. In this range of frequencies, increased acinar $\dot{V}_n\text{CO}_2$ heterogeneity gives the appearance of increased ventilation-to-perfusion mismatching. The effects of frequency-dependent transitioning from direct acinar ventilation to mixing and dispersion observed in these simulations are consistent with the results of washout imaging reported by Venegas et al. (49), whose findings were supported by a simplified model with heterogeneous dead space. Achieving increased direct acinar ventilation at higher frequencies, and thereby reducing the tidal volume required for eucapnia, may be possible through the use of specialized ventilation

apparatus designed to minimize dead space of the ventilator tubing and upper respiratory tract (44).

The selection of an optimal frequency for delivering HFOV may be described as a multiobjective optimization problem, wherein one objective is to minimize the volume amplitude and another objective is to minimize ventilation heterogeneity. Lower frequencies ($f < f_{res}$) require greater volume amplitudes, thus increasing the risk of overdistension in the presence of lung injury. High frequencies ($f > f_{res}$) minimize the volume amplitude required for eucapnia yet increase acinar flow heterogeneity and consequently acinar $\dot{V}_n\text{CO}_2$ heterogeneity. Based on these simulations, we predict that optimal HFOV for this canine model is delivered using frequencies slightly less than f_{res} . This range provides the best compromise between minimizing both volume amplitude and ventilation heterogeneity in the simulated canine lungs.

The spatial distributions shown in Fig. 7 demonstrate spatial concordance between regional acinar flow and CO_2 elimination, consistent with experimental studies combining positron emission and X-ray computed tomographies (21, 43, 55). The positive correlation between flow and CO_2 elimination decreased at higher frequencies, likely due to the diminishing influence of direct acinar ventilation and bulk transport on CO_2 elimination. Simulations from the healthy condition demonstrate a transition from elastically dominated flow and CO_2 elimination at low frequencies (as indicated by the influence of gravity on these distributions) to variable regional ventilation at higher frequencies. That is, the same lung region can experience a larger share of total ventilation at one particular frequency, yet smaller shares at others. This phenomenon yields the clustering of regionally preferred frequencies f_{max} as shown in Fig. 9. This finding suggests that a combination of multiple frequencies delivered simultaneously may produce more uniform overall ventilation (23).

Limitations

Despite the complexity of our model in terms of structural geometry, topology, fluid flow, and gas transport, there are numerous assumptions and simplifications that limit the physiological interpretation of these results. The pathophysiological features of ARDS are not realistically described by a simple altered distribution of tissue elastances. The model also does not account for derecruitment, perfusion shunting, or any changes in airway mechanics. Furthermore, the model ignores intratidal variations in mechanics, which are especially relevant to overdistension and cyclic derecruitment (2, 5).

Another assumption, that mixed-venous blood has a constant partial pressure of CO_2 in all simulations, restricts the applicability of these simulations to eucapnic conditions and short time scales; that is, all simulations are executed to calculate an instantaneous $\dot{V}_{tot}\text{CO}_2$ under the premise that mixed-venous CO_2 partial pressure is uniformly 46 mmHg throughout the lung. If the value of instantaneous $\dot{V}_{tot}\text{CO}_2$ calculated in this manner for any waveform is equal to the rate of CO_2 production by metabolism, then that waveform will maintain equilibrium of arterial CO_2 partial pressures. Also the assumed boundary condition used at the airway opening (i.e., $P_{ao}\text{CO}_2 = 0$ mmHg) neglects the additional dead space of the upper airways or an endotracheal tube. Thus we expect our results to slightly underestimate the volume amplitudes required for

eucapnic ventilation. The close agreement between simulation results and the experimental data of Venegas et al. (47) may be due in part to the latter's use of specialized oscillatory apparatus that delivered fresh gas directly to the trachea, bypassing the dead space upper airways (44). Boundary conditions at the acinar level do not include the effects of acinar interdependence (28), collateral ventilation (4), or pleural surface interactions at the chest wall, diaphragm, or between lobes (48).

The model of airway segment impedance used in this study (10) was intended to characterize flow phenomena up to the lower end of the acoustic range (i.e., up to 100 Hz), assuming Womersley-type oscillatory flow (42, 54) and isothermal gas compression. Admittedly, the lumped longitudinal and shunt airway segment impedances are simplifications of actual fluid mechanical descriptions of oscillatory flow. The isothermal gas compression compliance used in our model is also a limiting case of the full thermodynamic expression (6). The model is also limited in that it does not include other potentially influential gas transport mechanisms, such as asymmetric velocity profiles at bifurcations, differences between inspiratory and expiratory velocity profiles, or cardiogenic mixing (9). Furthermore, the included transport mechanisms are assumed to superimpose linearly, except for direct acinar ventilation (which is inherently nonlinear due to complete CO_2 removal at the airway opening). Despite limiting the scope of these modeled mechanisms for the sake of parsimony, this work does provide comparable results with previous experimental work using HFOV in dogs (15, 27, 45).

Aside from these limitations, there are several important considerations regarding the applicability of these canine simulations to mechanical ventilation in humans. Differences in anatomic structure of the canine airway tree compared with that of humans, such as increased branching asymmetry and dead space relative to body weight, will also yield differences in airway resistance, resonant frequency, and the transition frequency from conventional ventilation to HFOV (47). Moreover, the influence of frequency on the pressure cost of ventilation, as well as on the distribution of gas transport, may be altered in humans compared with dogs particularly at high frequencies (46). Clinically relevant predictions for optimal frequency selection during HFOV may be obtained using this gas transport model in airway structures based on human anatomy.

Conclusion

Oscillatory frequency has a substantial impact on ventilation distribution. The total tidal volume required to maintain eucapnia decreases with frequency. Thus increasing oscillatory frequency may minimize the risks associated with excessive volume distension. However increasing frequency may not be a universally appropriate ventilator management strategy, since frequency-dependent transitions from elastically dominated to inertially dominated ventilation distribution results in overventilation and underventilation simultaneously in different lung regions. Transitions in gas transport mechanisms also induce frequency-dependent heterogeneity in ventilation distribution, which may result in ventilation-to-perfusion mismatching and impairments in gas exchange. Thus it is essential to consider these multiple interdependent factors when selecting frequency during oscillation of the injured lung.

APPENDIX A-1

Derivation of mixing transport resistance

Consider an example bifurcation given by three cylindrical airway segments meeting at a central node. The CO₂ concentration at the central node is given by $C_0\text{CO}_2$, with concentrations at the distal end of each of the three adjoining airway segments ($i = 1, 2, 3$) given by $C_1\text{CO}_2$, $C_2\text{CO}_2$, and $C_3\text{CO}_2$. In the absence of diffusion and dispersion, the time-averaged value of $C_0\text{CO}_2$ is given by a weighted average of the neighboring concentrations $C_i\text{CO}_2$, for $i = 1, 2, 3$. Also assume that the weighting of each neighboring CO₂ concentration is proportional to the rate at which the mixing volume ($V_{\text{mix},i}$) passes completely through its respective airway segment. The $V_{\text{mix},i}$ is given by the (strictly) positive difference between the magnitude of total oscillating volume in the segment $|V_{\text{osc},i}|$ and the segment luminal volume itself ($V_{\text{seg},i}$):

$$V_{\text{mix},i} = \max(|V_{\text{osc},i}| - V_{\text{seg},i}, 0) \quad (\text{A1})$$

where max () indicates the maximum value of the enclosed arguments. The weighted averaged concentration at the central node is then:

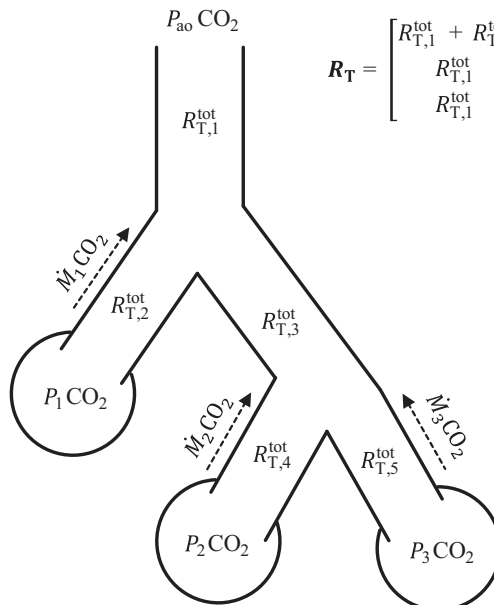
$$C_0\text{CO}_2 = \frac{\sum_{i=1}^3 fV_{\text{mix},i} C_i\text{CO}_2}{\sum_{i=1}^3 fV_{\text{mix},i}} \quad (\text{A2})$$

where f is the oscillation frequency. This weighting scheme ensures that 1) airway segments receiving greater proportions of incoming oscillatory gas flow provide greater contributions to mixing at the bifurcation, and 2) airway segments receiving oscillatory gas volumes less than their respective luminal volumes do not contribute to mixing at the bifurcation. Converting CO₂ concentrations to partial pressures based on the ideal gas law, we obtain:

$$P_0\text{CO}_2 = \frac{\sum_{i=1}^3 \frac{fV_{\text{mix},i}}{\mathcal{R}T} P_i\text{CO}_2}{\sum_{i=1}^3 \frac{fV_{\text{mix},i}}{\mathcal{R}T}} \quad (\text{A3})$$

where \mathcal{R} is the universal gas constant and T is the gas temperature. We assume that this mixing transport mechanism can be characterized by a transport resistance, such that the CO₂ molar flux in any airway

Fig. 10. Example airway network and corresponding system of equations for solving molar flux of CO₂ out of each acinus, according to Eq. A8. This network comprises 5 airways, terminating in 3 acini.



segment ($\dot{M}_i^{\text{mix}}\text{CO}_2$) is proportional to the mixing transport resistance for that airway ($R_{\text{T},i}^{\text{mix}}$). The axial CO₂ partial pressure difference from the distal end of each airway segment to the central node is given by $P_i\text{CO}_2 - P_0\text{CO}_2$. Since each CO₂ partial pressure differential is defined relative to the central node, conservation of mass of the CO₂ molar flux at the central node yields:

$$\sum_{i=1}^3 \dot{M}_i^{\text{mix}}\text{CO}_2 = \sum_{i=1}^3 \frac{P_i\text{CO}_2 - P_0\text{CO}_2}{R_{\text{T},i}^{\text{mix}}} = 0 \quad (\text{A4})$$

Rearranging Eq. A4 to solve for the CO₂ partial pressure at the central node yields:

$$P_0\text{CO}_2 = \frac{\sum_{i=1}^3 \left[\left(\frac{1}{R_{\text{T},i}^{\text{mix}}} \right) P_i\text{CO}_2 \right]}{\sum_{i=1}^3 \left(\frac{1}{R_{\text{T},i}^{\text{mix}}} \right)} \quad (\text{A5})$$

Combining Eqs. A3 and A5, it can be demonstrated that $R_{\text{T},i}^{\text{mix}}$ is inversely proportional to the weighting factor:

$$R_{\text{T},i}^{\text{mix}} = \varepsilon \frac{\mathcal{R}T}{fV_{\text{mix},i}} \quad (\text{A6})$$

where ε is a constant of proportionality characterizing the completeness with which $V_{\text{mix},i}$ is homogenized between neighboring nodes. Very large ε yields $R_{\text{T},i}^{\text{mix}}$ approaching infinity, resulting in no mixing and no transport. In the current study we have assumed complete homogenization of $V_{\text{mix},i}$ such that ε is unity, and Eq. A6 becomes:

$$R_{\text{T},i}^{\text{mix}} = \frac{\mathcal{R}T}{fV_{\text{mix},i}} \quad (\text{A7})$$

APPENDIX A-2

Mesh analysis of transport resistance network

The transport resistance $R_{\text{T}}^{\text{tot}}$ of an airway segment relates the molar flux \dot{M} and CO₂ partial pressure differential ΔPCO_2 in the axial direction. For a network of branching airways, a system of linear ordinary differential equations can be easily solved. A mesh analysis of the system ensures conservation of mass, such that the sum of molar fluxes through the airway opening and every terminal airway

$$\begin{aligned} \mathbf{R}_{\text{T}} &= \begin{bmatrix} R_{\text{T},1}^{\text{tot}} + R_{\text{T},2}^{\text{tot}} & R_{\text{T},1}^{\text{tot}} & R_{\text{T},1}^{\text{tot}} \\ R_{\text{T},1}^{\text{tot}} & R_{\text{T},1}^{\text{tot}} + R_{\text{T},3}^{\text{tot}} + R_{\text{T},4}^{\text{tot}} & R_{\text{T},1}^{\text{tot}} + R_{\text{T},3}^{\text{tot}} \\ R_{\text{T},1}^{\text{tot}} & R_{\text{T},1}^{\text{tot}} + R_{\text{T},3}^{\text{tot}} & R_{\text{T},1}^{\text{tot}} + R_{\text{T},3}^{\text{tot}} + R_{\text{T},5}^{\text{tot}} \end{bmatrix} \\ \mathbf{MCO}_2 &= \begin{bmatrix} M_1\text{CO}_2 \\ M_2\text{CO}_2 \\ M_3\text{CO}_2 \end{bmatrix} \\ \Delta\text{PCO}_2 &= \begin{bmatrix} P_1\text{CO}_2 - P_{\text{ao}}\text{CO}_2 \\ P_2\text{CO}_2 - P_{\text{ao}}\text{CO}_2 \\ P_3\text{CO}_2 - P_{\text{ao}}\text{CO}_2 \end{bmatrix} \end{aligned}$$

segment is zero. The molar fluxes at the proximal node of every acinus are chosen as state variables, and the system of equations is expressed in matrix notation as:

$$\mathbf{R}_T \dot{M}_{CO_2} = \Delta PCO_2 \quad (A8)$$

where each row of the system corresponds to the mesh formed by the airways connecting a single acinus to the airway opening. Accordingly, each term in ΔPCO_2 corresponds to total CO_2 partial pressure loss between an n th acinus and the airway opening $P_n CO_2 - P_{ao} CO_2$, and the corresponding n th row of the matrix product $\mathbf{R}_T \dot{M}_{CO_2}$ corresponds to the sum of partial pressure losses due to transport resistance in each airway between that n th acinus and the airway opening.

The matrix \mathbf{R}_T is completely dense, because the transport resistance of the trachea $R_{T,trachea}^{\text{tot}}$ is included in every mesh. In other words, every path from an acinus to the airway opening includes the same partial pressure loss over the trachea, which is equal to

$R_{T,trachea}^{\text{tot}} \sum_{n=1}^N \dot{M}_n CO_2$ where n indexes all individual acini. A simple example of an airway network and corresponding system of equations is provided in Fig. 10. Because matrix \mathbf{R}_T is completely dense, memory cost may be substantial for large numbers of airways. However \mathbf{R}_T is symmetric and can be stored and solved efficiently using dedicated algorithms for symmetric matrices.

An alternative to mesh analysis is nodal analysis, which involves choosing the state variables as the partial pressures at the proximal node of every airway segment. Nodal analysis forms a system of equations using conservation of mass applied to each individual node, which produces a sparse coefficient matrix. However, small numerical inaccuracies at each node can result in substantial discrepancies between the flux at the airway opening and the total flux across the acini. Thus, mesh analysis is preferred.

APPENDIX A-3

Expected low-frequency gas exchange behavior

Expected values for low-frequency gas exchange (i.e., 0.1 Hz < f < 1 Hz) are derived from standard equations of gas exchange physiology during conventional mechanical ventilation and spontaneous breathing. Given the assumption that CO_2 elimination is dominated by direct alveolar ventilation and is therefore proportional to alveolar ventilation, we have:

$$\dot{V}_{\text{tot}}^{\text{euc}} CO_2 \propto f(V_T^{\text{euc}} - V_D) \quad (A9)$$

Alveolar partial pressure CO_2 is related to the eucapnic alveolar ventilation (\dot{V}_A) and CO_2 elimination rate ($\dot{V}_{\text{tot}}^{\text{euc}} CO_2$) and is assumed to be equal to mixed arterial CO_2 partial pressure ($P_a CO_2$):

$$\frac{\dot{V}_{\text{tot}}^{\text{euc}} CO_2}{\dot{V}_A} = \frac{\dot{V}_{\text{tot}}^{\text{euc}} CO_2}{f(V_T^{\text{euc}} - V_D)} = \frac{P_a CO_2}{863} \quad (A10)$$

where 863 is a conversion factor between partial pressure in mmHg and gas volume fraction, accounting for the difference between $\dot{V}_{\text{tot}}^{\text{euc}} CO_2$ in l/s at standard temperature and pressure dry air, and \dot{V}_A in l/s at body temperature and pressure air saturated with water vapor. Equation A10 can be rearranged in the form of the power-law regression in Eq. 15, such that:

$$V_T^{\text{euc}} = V_D + \left(\frac{863}{P_a CO_2} \dot{V}_{\text{tot}}^{\text{euc}} CO_2 \right) f^{-1} \quad (A11)$$

Thus, the expected values for the power-law regression parameters for Eq. 15 are $\beta_0 = V_D$, $\beta_1 = \left(\frac{863}{P_a CO_2} \dot{V}_{\text{tot}}^{\text{euc}} CO_2 \right)$, and $\beta_2 = -1$.

ACKNOWLEDGMENTS

Portions of this work were excerpted from Master of Science thesis “Simulation of Ventilation Distribution and Gas Transport During Oscillatory Ventilation” by Jacob Herrmann, Boston University, 2015. The authors thank Drs. Bela Suki, Brett Simon, J. Jane Pillow, and Joseph Tien for helpful suggestions during the course of this work.

GRANTS

This work was supported in part by the Medical Technologies Centre of Research Excellence at the University of Auckland (M. H. Tawhai), National Institutes of Health Grant UM1 HL-108724 (D. W. Kaczka), US Department of Defense Grant PR151761 (D. W. Kaczka), and the University of Iowa Department of Anesthesia (D. W. Kaczka, J. Herrmann).

DISCLOSURES

D. W. Kaczka and J. Herrmann are coinventors on a pending patent involving multifrequency oscillatory ventilation (MFOV). In addition, they are cofounders and shareholders of Oscillavent, Inc.

AUTHOR CONTRIBUTIONS

J.H., M.H.T., and D.W.K. conception and design of research; J.H. and M.H.T. performed experiments; J.H., M.H.T., and D.W.K. analyzed data; J.H., M.H.T., and D.W.K. interpreted results of experiments; J.H. and D.W.K. prepared figures; J.H. and D.W.K. drafted manuscript; J.H., M.H.T., and D.W.K. edited and revised manuscript; J.H., M.H.T., and D.W.K. approved final version of manuscript.

REFERENCES

1. **The Acute Respiratory Distress Syndrome Network.** Ventilation with lower tidal volumes as compared with traditional tidal volumes for acute lung injury and the acute respiratory distress syndrome. *N Engl J Med* 342: 1301–1308, 2000. doi:10.1056/NEJM200005043421801.
2. **Amini R, Herrmann J, Kaczka DW.** Intratidal overdistension and derecruitment in the injured lung: A simulation study [epub ahead of print]. *IEEE Trans Biomed Eng* in press, 2016. doi:10.1109/TBME.2016.2572678.
3. **Amini R, Kaczka DW.** Impact of ventilation frequency and parenchymal stiffness on flow and pressure distribution in a canine lung model. *Ann Biomed Eng* 41: 2699–2711, 2013. doi:10.1007/s10439-013-0866-7.
4. **Armengol J, Jones RL, King EG.** Collateral ventilation during high-frequency oscillation in dogs *J Appl Physiol* (1985) 58: 173–179, 1985.
5. **Bates JHT, Irvin CG.** Time dependence of recruitment and derecruitment in the lung: a theoretical model. *J Appl Physiol* (1985) 93: 705–713, 2002. doi:10.1152/japplphysiol.01274.2001.
6. **Benade AH.** On the propagation of sound waves in a cylindrical conduit. *J Acoust Soc Am* 44: 616–623, 1968. doi:10.1121/1.1911130.
7. **Berdine GG, Lehr JL, McKinley DS, Drazen JM.** Nonuniformity of canine lung washout by high-frequency ventilation. *J Appl Physiol* (1985) 61: 1388–1394, 1986.
8. **Carvalho AR, Spieth PM, Pelosi P, Vidal Melo MF, Koch T, Jandre FC, Giannella-Neto A, de Abreu MG.** Ability of dynamic airway pressure curve profile and elastance for positive end-expiratory pressure titration. *Intensive Care Med* 34: 2291–2299, 2008. doi:10.1007/s00134-008-1301-7.
9. **Chang HK.** Mechanisms of gas transport during ventilation by high-frequency oscillation. *J Appl Physiol Respir Environ Exerc Physiol* 56: 553–563, 1984.
10. **Colletti AA, Amini R, Kaczka DW.** Simulating ventilation distribution in heterogeneous lung injury using a binary tree data structure. *Comput Biol Med* 41: 936–945, 2011. doi:10.1016/j.combiom.2011.08.004.
11. **Ebert DS, Musgrave FK, Peachey D, Perlin K, Worley S, Mark WR, Hart JC.** *Texture and Modeling: A Procedural Approach* (3rd ed.). San Francisco, CA: Morgan Kaufmann Publishers, 2002.
12. **Ferguson ND, Cook DJ, Guyatt GH, Mehta S, Hand L, Austin P, Zhou Q, Matte A, Walter SD, Lamontagne F, Granton JT, Arabi YM, Arroliga AC, Stewart TE, Slutsky AS, Meade MO; OSCILLATE Trial Investigators; Canadian Critical Care Trials Group.** High-frequency oscillation in early acute respiratory distress syndrome. *N Engl J Med* 368: 795–805, 2013. doi:10.1056/NEJMoa1215554.
13. **Fortune JB, Wagner PD.** Effects of common dead space on inert gas exchange in mathematical models of the lung. *J Appl Physiol Respir Environ Exerc Physiol* 47: 896–906, 1979.

14. Fredberg JJ. Augmented diffusion in the airways can support pulmonary gas exchange. *J Appl Physiol Respir Environ Exerc Physiol* 49: 232–238, 1980.
15. Fredberg JJ, Keefe DH, Glass GM, Castile RG, Frantz ID III. Alveolar pressure nonhomogeneity during small-amplitude high-frequency oscillation. *J Appl Physiol Respir Environ Exerc Physiol* 57: 788–800, 1984.
16. Greenblatt EE, Butler JP, Venegas JG, Winkler T. Pendelluft in the bronchial tree. *J Appl Physiol* (1985) 117: 979–988, 2014. doi:[10.1152/japplphysiol.00466.2014](https://doi.org/10.1152/japplphysiol.00466.2014).
17. Hantos Z, Daróczy B, Suki B, Nagy S, Fredberg JJ. Input impedance and peripheral inhomogeneity of dog lungs. *J Appl Physiol* (1985) 72: 168–178, 1992.
18. Haskins S, Pascoe PJ, Ilkiw JE, Fudge J, Hopper K, Aldrich J. Reference cardiopulmonary values in normal dogs. *Comp Med* 55: 156–161, 2005.
19. Jaeger MJ. High-frequency ventilation in dogs with three gases of different densities. *J Appl Physiol* (1985) 70: 2188–2192, 1991.
20. Jaeger MJ, Kurzweg UH, Banner MJ. Transport of gases in high-frequency ventilation. *Crit Care Med* 12: 708–710, 1984. doi:[10.1097/00003246-198409000-00003](https://doi.org/10.1097/00003246-198409000-00003).
21. Johansen T, Winkler T, Kelly VJ, Osorio-Valencia JS, Greenblatt EE, Harris RS, Venegas JG. A method for mapping regional oxygen and CO₂ transfer in the lung. *Respir Physiol Neurobiol* 222: 29–47, 2016. doi:[10.1016/j.resp.2015.10.017](https://doi.org/10.1016/j.resp.2015.10.017).
22. Kaczka DW, Brown RH, Mitzner W. Assessment of heterogeneous airway constriction in dogs: a structure-function analysis. *J Appl Physiol* (1985) 106: 520–530, 2009. doi:[10.1152/japplphysiol.90576.2008](https://doi.org/10.1152/japplphysiol.90576.2008).
23. Kaczka DW, Herrmann J, Zonneveld CE, Tingay DG, Lavizzari A, Noble PB, Pillow JJ. Multifrequency oscillatory ventilation in the premature lung: effects on gas exchange, mechanics, and ventilation distribution. *Anesthesiology* 123: 1394–1403, 2015. doi:[10.1097/ALN.0000000000000898](https://doi.org/10.1097/ALN.0000000000000898).
24. Kaczka DW, Massa CB, Simon BA. Reliability of estimating stochastic lung tissue heterogeneity from pulmonary impedance spectra: a forward-inverse modeling study. *Ann Biomed Eng* 35: 1722–1738, 2007. doi:[10.1007/s10439-007-9339-1](https://doi.org/10.1007/s10439-007-9339-1).
25. Khoo MC, Slutsky AS, Drazen JM, Solway J, Gavriely N, Kamm RD. Gas mixing during high-frequency ventilation: an improved model. *J Appl Physiol Respir Environ Exerc Physiol* 57: 493–506, 1984.
26. Lai-Fook SJ, Rodarte JR. Pleural pressure distribution and its relationship to lung volume and interstitial pressure. *J Appl Physiol* (1985) 70: 967–978, 1991.
27. Lehr JL, Butler JP, Westerman PA, Zatz SL, Drazen JM. Photographic measurement of pleural surface motion during lung oscillation. *J Appl Physiol* (1985) 59: 623–633, 1985.
28. Mead J, Takishima T, Leith D. Stress distribution in lungs: a model of pulmonary elasticity. *J Appl Physiol* 28: 596–608, 1970.
29. Otis AB, McKerrow CB, Bartlett RA, Mead J, McIlroy MB, Selver-Stone NJ, Radford EP Jr. Mechanical factors in distribution of pulmonary ventilation [Online]. [8 Sep. 2014]. *J Appl Physiol* 8: 427–443, 1956. <http://www.ncbi.nlm.nih.gov/pubmed/13286206>
30. Piiper J, Scheid P. Diffusion and convection in intrapulmonary gas mixing, in *Comprehensive Physiology*. Bethesda, MD: John Wiley & Sons, p. 51–69. doi:[10.1002/cphy.cp030404](https://doi.org/10.1002/cphy.cp030404).
31. Pillow JJ. High-frequency oscillatory ventilation: mechanisms of gas exchange and lung mechanics. *Crit Care Med* 33, Suppl: S135–S141, 2005. doi:[10.1097/01.CCM.0000155789.52984.B7](https://doi.org/10.1097/01.CCM.0000155789.52984.B7).
32. Poulsen P, Karbing DS, Rees SE, Andreassen S. Tidal breathing model describing end-tidal, alveolar, arterial and mixed venous CO₂ and O₂. *Comput Methods Programs Biomed* 101: 166–172, 2011. doi:[10.1016/j.cmpb.2010.03.020](https://doi.org/10.1016/j.cmpb.2010.03.020).
33. Scherer PW, Haselton FR, Seybert JR. Gas transport in branched airways during high-frequency ventilation. *Ann Biomed Eng* 12: 385–405, 1984. doi:[10.1007/BF02407782](https://doi.org/10.1007/BF02407782).
34. Scherer PW, Shendelman LH, Greene NM, Bouhuys A. Measurement of axial diffusivities in a model of the bronchial airways. *J Appl Physiol* 38: 719–723, 1975.
35. Slutsky AS, Drazen FM, Ingram RH Jr, Kamm RD, Shapiro AH, Fredberg JJ, Loring SH, Lehr J. Effective pulmonary ventilation with small-volume oscillations at high frequency. *Science* 209: 609–671, 1980. doi:[10.1126/science.6771872](https://doi.org/10.1126/science.6771872).
36. Slutsky AS, Kamm RD, Rossing TH, Loring SH, Lehr J, Shapiro AH, Ingram RH Jr, Drazen JM. Effects of frequency, tidal volume, and lung volume on CO₂ elimination in dogs by high frequency (2–30 Hz), low tidal volume ventilation. *J Clin Invest* 68: 1475–1484, 1981. doi:[10.1172/JCI110400](https://doi.org/10.1172/JCI110400).
37. Slutsky AS, Ranieri VM. Ventilator-induced lung injury. *N Engl J Med* 369: 2126–2136, 2013. doi:[10.1056/NEJMra1208707](https://doi.org/10.1056/NEJMra1208707).
38. Tawhai MH, Hunter P, Tschirren J, Reinhardt J, McLennan G, Hoffman EA. CT-based geometry analysis and finite element models of the human and ovine bronchial tree. *J Appl Physiol* (1985) 97: 2310–2321, 2004. doi:[10.1152/japplphysiol.00520.2004](https://doi.org/10.1152/japplphysiol.00520.2004).
39. Howatson Tawhai M, Pullam AJ, Hunter PJ. Generation of an anatomically based three-dimensional model of the conducting airways. *Ann Biomed Eng* 28: 793–802, 2000. doi:[10.1141/1.1289457](https://doi.org/10.1141/1.1289457).
40. Taylor G. The dispersion of matter in turbulent flow through a pipe. *Proc R Soc A Math Phys Eng Sci* 223: 446–468, 1954.
41. Thorpe CW, Bates JHT. Effect of stochastic heterogeneity on lung impedance during acute bronchoconstriction: a model analysis. *J Appl Physiol* (1985) 82: 1616–1625, 1997.
42. Thurston GB. Periodic fluid flow through circular tubes. *J Acoust Soc Am* 24: 653–656, 1952. doi:[10.1121/1.1906949](https://doi.org/10.1121/1.1906949).
43. Tsuzaki K, Hales CA, Strieder DJ, Venegas JG. Regional lung mechanics and gas transport in lungs with inhomogeneous compliance. *J Appl Physiol* (1985) 75: 206–216, 1993.
44. Venegas JG. Equivalent circuit analysis of high-frequency ventilators including a new high-impedance flow-interrupting ventilator. *IEEE Trans Biomed Eng* 33: 420–427, 1986. doi:[10.1109/TBME.1986.325798](https://doi.org/10.1109/TBME.1986.325798).
45. Venegas JG, Custer J, Kamm RD, Hales CA. Relationship for gas transport during high-frequency ventilation in dogs. *J Appl Physiol* (1985) 59: 1539–1547, 1985.
46. Venegas JG, Fredberg JJ. Understanding the pressure cost of ventilation: why does high-frequency ventilation work? *Crit Care Med* 22, Suppl: S49–S57, 1994. doi:[10.1097/00003246-199422091-00004](https://doi.org/10.1097/00003246-199422091-00004).
47. Venegas JG, Hales CA, Strieder DJ. A general dimensionless equation of gas transport by high-frequency ventilation. *J Appl Physiol* (1985) 60: 1025–1030, 1986.
48. Venegas JG, Tsuzaki K, Fox BJ, Simon BA, Hales CA. Regional coupling between chest wall and lung expansion during HFV: a positron imaging study. *J Appl Physiol* (1985) 74: 2242–2252, 1993.
49. Venegas JG, Yamada Y, Custer J, Hales CA. Effects of respiratory variables on regional gas transport during high-frequency ventilation. *J Appl Physiol* (1985) 64: 2108–2118, 1988.
50. Watson EJ. Diffusion in oscillatory pipe flow. *J Fluid Mech* 133: 233–244, 1983. doi:[10.1017/S0022112083001883](https://doi.org/10.1017/S0022112083001883).
51. Watson JW, Jackson AC. CO₂ elimination as a function of frequency and tidal volume in rabbits during HFO. *J Appl Physiol Respir Environ Exerc Physiol* 57: 354–359, 1984.
52. Watson JW, Jackson AC. Frequency dependence of CO₂ elimination and respiratory resistance in monkeys. *J Appl Physiol* (1985) 58: 653–657, 1985.
53. West JB. Ventilation-perfusion inequality and overall gas exchange in computer models of the lung. *Respir Physiol* 7: 88–110, 1969. doi:[10.1016/0034-5687\(69\)90071-1](https://doi.org/10.1016/0034-5687(69)90071-1).
54. Womersley JR. Method for the calculation of velocity, rate of flow and viscous drag in arteries when the pressure gradient is known. *J Physiol* 127: 553–563, 1955. doi:[10.1113/jphysiol.1955.sp005276](https://doi.org/10.1113/jphysiol.1955.sp005276).
55. Yamada Y, Burnham C, Hales CA, Venegas JG. Regional mapping of gas transport during high-frequency and conventional ventilation. *J Appl Physiol* (1985) 66: 1209–1218, 1989.
56. Young D, Lamb SE, Shah S, MacKenzie I, Tunnicliffe W, Lall R, Rowan K, Cuthbertson BH; OSCAR Study Group. High-frequency oscillation for acute respiratory distress syndrome. *N Engl J Med* 368: 806–813, 2013. doi:[10.1056/NEJMoa1215716](https://doi.org/10.1056/NEJMoa1215716).

2017 Meeting of the American Society of Anesthesiologists

[Print this Page for Your Records](#)[Close Window](#)**Control/Tracking Number :** 17-SA-4940-ASAHQ**Activity :** Scientific Abstract**Current Date/Time :** 4/3/2017 8:09:43 PM**TITLE:****Parenchymal Strain vs. Strain Rate During Multi-Frequency Oscillatory Ventilation****AUTHOR(S):****David W. Kaczka, M.D.,Ph.D.**¹, Jacob Herrmann, M.S.², Merryn H. Tawhai, Ph.D.³.

¹Anesthesia, Biomedical Engineering, and Radiology, University of Iowa, Iowa City, IA, USA, ²Anesthesia and Biomedical Engineering, University of Iowa, Iowa City, IA, USA, ³Auckland Bioengineering Institute, University of Auckland, Auckland, New Zealand.

AFFIRMATIONS:**Affirmations Cont. (Complete):****I Agree:** True

*: I agree to the above statements

*: No human subjects were involved in the research

*: No animal subjects were involved in the research

*: No human or animal subjects were involved in the research

SESSION CATEGORY:

017.2 RESPIRATION - Pulmonary Mechanics and Ventilation (Including Artificial)

QUESTIONNAIRE:**Questionnaire (Complete):****Please select:** No, do not consider my abstract for the ANESTHESIOLOGY Journal Symposium**Is this abstract submitted by a resident?**: No**Funding Information:** Other Federal Funding**If you chose "Other" above, please explain (250 characters):** U.S. Department of Defense**Yes or No?**: No**Please select:** Yes, I would like to be considered to present an Oral/Poster Discussion Session.**Please Select:** If my abstract is selected for a poster presentation at ANESTHESIOLOGY® 2017, I would have no **preference** between an electronic or a printed poster presentation**ABSTRACT:**

Introduction: Ventilator-induced lung injury (VILI) in mechanically ventilated patients may result from extreme stresses, strains, and strain rates associated with parenchymal overdistension, as well as repetitive alveolar collapse and reopening. High frequency oscillatory ventilation (HFOV) is an alternative lung-protective ventilation strategy, which attempts to minimize VILI using small volume amplitudes delivered at high frequencies (2 to 20 Hz). However oscillatory ventilation at a single discrete frequency is distributed non-uniformly and in a frequency-dependent manner, especially in the mechanically heterogeneous lung. In a previous study, we demonstrated that lung function and gas exchange can be significantly improved if volume oscillations are applied at multiple simultaneous frequencies, rather than at a single discrete frequency (Kaczka et al. Anesthesiology 123:1394-1403, 2015). We refer to this unique ventilatory modality as 'Multi-Frequency Oscillatory Ventilation' (MFOV), and propose that improved physiologic outcomes arise from the more even distribution of ventilation, in accordance with local lung mechanical properties. In the present study, we hypothesized that the spectral content of MFOV waveforms can be further tuned according to the relative contributions of acinar strain vs. strain rate to VILI. We developed a computational model of the porcine lung to investigate the potential for minimizing distributed acinar strains and strain rates during MFOV. **Methods:** The computational model was constructed using a central airway tree segmented from a computed tomographic image of a supine pig, with algorithmically generated peripheral airways. The model consisted of 60,494 airway segments in total, with 30,243 viscoelastic acini. Eucapnic ventilation was simulated using a Monte Carlo technique to select from over one thousand MFOV waveforms consisting of four frequencies (5, 10, 15, and 20 Hz), with randomized volume amplitudes and phases. Corresponding distributions of acinar strains and strain rates throughout the model were determined for each MFOV waveform, and used to compute a cost function defined by weighting terms to emphasize the percent contributions of parenchymal strain vs. strain rate to VILI. **Results:** Our simulations demonstrated that MFOV waveforms were superior to traditional single-frequency HFOV for minimizing strain and strain rate in both healthy and injured lungs. Optimized volume amplitudes at each frequency in the

MFOV waveform were modulated according to the relative cost function weighting of strain and strain rate, as well as the degree of lung mechanical heterogeneity (Figure 1). Increasing contribution of strain rate to VILI (as opposed to strain) resulted in decreasing volume amplitudes at higher frequencies for the optimized MFOV waveforms. **Conclusion:** These simulations indicate that frequency content in MFOV waveforms may be tuned to minimize the relative contributions of parenchymal strain and strain rate. Our unique approach may allow for the selection of patient-specific optimized MFOV waveforms, especially when combined with experimental evidence to justify physiologically-

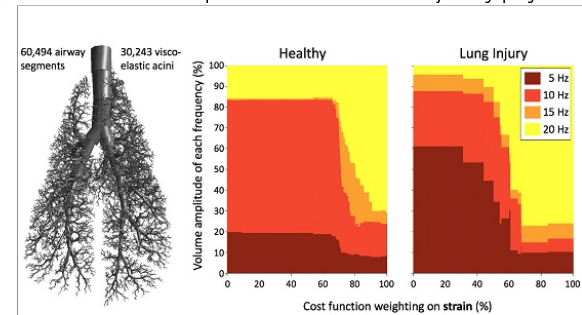


Figure 1: Computational model of porcine lung (left panel). Optimal volume amplitudes at each frequency are shown for varying cost function emphasis on strain vs. strain rate, in simulated healthy conditions (center panel) and heterogeneous lung injury (right panel).

relevant emphasis on strain vs. strain rate to minimize risk for VILI.

SUMMARY:

Multi-Frequency Oscillatory Ventilation (MFOV) has been demonstrated to improve physiologic outcomes in heterogeneous lungs, due to more even distribution of ventilation. In this computational modeling study of the porcine lung, we demonstrate that the spectral content of MFOV waveforms can be further optimized, according to the relative contributions of parenchymal strain vs. strain rate to ventilator-induced lung injury.

Status: Complete

[Leave OASIS Feedback](#)